

# Towards Universal Solvers: Using PGD Attack in Active Learning to Increase Generalizability of Neural Operators as Knowledge Distillation from Numerical PDE Solvers

Yifei Sun\*<sup>1</sup>

<sup>1</sup>University of Michigan-Ann Arbor, School of Information

## Abstract

Nonlinear partial differential equations (PDEs) typically require very fine spatial and temporal discretizations and local linear/Taylor-type approximations of nonlinear terms; this leads to large memory footprints and long step-by-step solver runtimes. [39] Neural operators extend neural networks’ universal function approximation perspective to mappings between function spaces and learn direct function-to-function surrogates that can be queried at arbitrary spatio-temporal points, exemplified by Fourier Neural Operators (FNOs) and DeepONets. [39, 46] Compared with iterative time-marching, Fourier-based operator architectures can truncate high-frequency components and perform fast single-shot inference while maintaining high accuracy on in-distribution data, indicating possible redundancy in traditional solvers’ spatio-temporal discretization. [39, 41] A major limitation of data-driven neural operators is poor out-of-distribution (OOD) generalization: when input functions have ranges or structural features that depart from the training distribution, neural-operator predictions can differ substantially from solver ground truth, preventing their use as universal solvers. To address this, we propose a teacher–student distillation framework in which a differentiable numerical solver (teacher) supervises a compact neural-operator student. Because solver-generated labels are expensive, we embed an active/adversarial sample selection loop in a minimax (PGD-style) formulation: with the student fixed we search (via projected gradient maximization) for input perturbations that maximize the student–teacher discrepancy (subject to physically motivated smoothness/energy constraints), add those worst-case examples to the training pool, and update the student. [47] Leveraging a differentiable spectral solver such as Exponax permits back-propagation of solver gradients into the adversarial search, stabilizing and strengthening sample mining under periodic/spectral settings. [32] We validate our method using FNO students and a differentiable spectral solver on canonical benchmarks (1D Burgers and 2D Navier–Stokes). Experiments show that adversarially guided distillation substantially improves OOD robustness while retaining the low parameter count and fast single-shot inference of neural operators, expanding their practical utility as surrogate PDE solvers.

## Introduction

Nonlinear partial differential equations (PDEs) arise across the physical and engineering sciences and often govern complex, multi-scale dynamics such as shock formation, turbulence, pattern formation and other strongly nonlinear phenomena. Classical numerical approaches for such problems—finite differences, finite volumes/elements, spectral methods and their time-integrators—rely on discretizing the spatial and temporal domains into fine meshes and advancing the solution through many small time steps. This strategy approximates nonlinear terms locally via linearization or low-order Taylor expansions and enforces stability through small time steps (e.g., CFL-like constraints) and refined spatial resolution. While well-understood and broadly successful, this approach can lead to very large numbers of spatio-temporal degrees of freedom, heavy memory (and GPU) requirements, and long wall-clock forward-solve times for long-time or high-resolution simulations. Moreover, classical discretizations remain susceptible to numerical instabilities

---

\*Corresponding author: yifeisun@umich.edu

when resolution or timestep choices are suboptimal, exhibiting blow-up, spurious oscillations, and Gibbs-like artifacts near discontinuities or sharp gradients (for example, shock waves in Burgers-type problems).

An alternative paradigm that has gained rapid traction is to learn *operators*—maps between infinite-dimensional function spaces—directly from data. Neural operators extend the idea of neural networks as universal *function* approximators to universal *operator* approximators, i.e., models that take an input function (e.g., an initial condition or forcing field) and output a target function (e.g., the solution field at a later time) without performing explicit step-by-step time marching. Representative architectures include DeepONet, which combines branch and trunk networks motivated by operator approximation theory [46], and Fourier Neural Operators (FNOs), which parametrize integral kernels in Fourier space and have demonstrated fast, accurate, single-shot predictions for canonical PDE benchmarks such as Burgers and Navier–Stokes [39]. These neural-operator methods can be queried at arbitrary spatio-temporal coordinates, and when trained and evaluated in-distribution they often produce highly accurate outputs while dramatically reducing runtime compared to conventional solvers. In particular, Fourier-based methods exploit frequency truncation—retaining only the dominant low-frequency modes—so a compact set of parameters can capture the essential large-scale dynamics and produce rapid, single-pass inference [39].

The success of neural operators in many settings highlights two complementary insights. First, for many practical prediction tasks there can be redundancy in the very fine spatio-temporal discretizations used by classical solvers: the information required to obtain an accurate map from inputs to outputs can be compressed into a smaller set of spectral coefficients or learned features. Second, neural operators’ interpolation and regression characteristics often make them numerically robust: unlike an explicit time integrator whose stability can catastrophically fail when timesteps are too large or the spatial grid too coarse, learned surrogates trained on representative solutions tend to produce outputs that remain near the training-output manifold and therefore avoid the uncontrolled numeric blow-up typical in poorly resolved solvers. Taken together, this explains why, in many empirical tests, FNO-like surrogates can provide accurate predictions with coarser temporal granularity and much lower computational cost [39].

Despite these advantages, a fundamental limitation of current neural-operator approaches is their data-driven nature: they typically generalize well only when test inputs are drawn from the same distribution as the training data. When confronted with out-of-distribution (OOD) inputs—especially those whose local cell-wise ranges, spectral content, or global statistics differ substantially from the training set—neural-operator predictions can deviate severely from the ground-truth solutions produced by trusted numerical solvers. In practice this manifests as large predictive error or qualitatively wrong dynamics when the model is asked to extrapolate beyond the training manifold. This lack of robust OOD generalization means that neural operators are not yet reliable *universal solvers* that one can confidently apply to arbitrary inputs without careful validation or retraining. From a theoretical perspective, this shortcoming is unsurprising: compact neural-operator parametrizations (few layers, truncated spectra, relatively small parameter counts) trade expressive generality for speed and parsimony, and the complex, distribution-sensitive evolution laws of nonlinear PDEs mean that dynamics can change qualitatively as input distributions shift.

A second, related body of PDE-learning work is formed by physics-informed neural networks (PINNs) and their variants. PINNs treat a neural network as a surrogate for the solution *function* and enforce PDE residuals, boundary and initial conditions via automatic differentiation during training. Because PINNs operate at the level of pointwise collocation (space–time coordinates), active and adaptive sampling of residual points has been extensively studied to locate failure regions (e.g., near shocks or steep gradients) and to improve training efficiency and accuracy [78]. Recently, adversarial/adaptive schemes for PINNs—e.g., PGD-style adversarial sampling that moves collocation points toward local maxima of the PDE residual—have been proposed to automatically find and correct failure regions without strong distributional assumptions [38]. While these sampling strategies mitigate some PINN failure modes, PINNs and neural operators fundamentally differ in input–output granularity: PINNs approximate a single solution function across the domain (pointwise), whereas neural operators learn mappings between whole functions (high-dimensional tensor inputs). Consequently, many PINN-centric active-sampling techniques do not translate directly to operator learning, because operator inputs live in very high-dimensional, often unbounded function spaces and residual-landscape assumptions (e.g., low-dimensional parametric forms) are harder to justify.

Motivated by these observations, in this work we explore a hybrid *solver–student* framework that leverages the strengths of both differentiable numerical solvers and compact neural operators. Concretely, we treat a high-fidelity, differentiable PDE solver (teacher)—such as a Fourier-spectral, JAX-based integrator that

supports gradient propagation (e.g., Exponax)—as the canonical source of truth and distill its input→output operator into a compact neural-operator student (e.g., an FNO). The student is trained to mimic the solver’s mapping from initial/forcing functions to solution fields at target times; once trained, the neural operator functions as a fast surrogate that can be queried with coarse temporal granularity or in a single shot, providing orders-of-magnitude speedups over the solver for in-distribution cases [32, 39].

Because generating solver-labeled training data is computationally expensive, naive distillation like random sampling in a neighborhood in the functional space over a nominal training distribution risks producing a model that performs poorly on neighboring regions of function space. To overcome this, we embed an active learning/adversarial training sample-mining loop into the distillation process using a minimax formulation inspired by adversarial robustness literature [47] and adaptive PINN sampling approaches [38, 78]. With the student’s parameters frozen, we seek small perturbations (in an appropriate norm and subject to physically motivated smoothness or periodicity constraints) to input functions that maximally increase a solver–student discrepancy loss; these adversarial inputs reveal the regions in function space where the student is weakest. The solver—being differentiable—provides meaningful gradient information with respect to the input function (interpretable as a Fréchet-type derivative in function space), which stabilizes and strengthens the adversarial search. We then add the discovered worst-case input→solver-output pairs into the student’s training pool and update the student, iterating this search-and-retrain loop. This approach generalizes the PGD-style adversarial training paradigm to operator distillation and active sampling in very high-dimensional function spaces.

We implement and evaluate this framework using FNO students and a differentiable spectral teacher (Exponax) on canonical testbeds including 1D viscous Burgers and 2D incompressible Navier–Stokes problems—the same classes of examples used in many seminal neural-operator studies [39]. Our experiments characterize how adversarially guided distillation improves OOD robustness, quantify the trade-offs between perturbation strength and sample-efficiency, and analyze the role of solver-provided gradients in accelerating adversarial sample discovery and improving student generalization. The results demonstrate that adversarially informed distillation can substantially enlarge the effective domain of reliability for compact neural operators while preserving their computational advantages, pointing toward more practical and trustworthy operator surrogates for complex nonlinear PDEs.

## Related Work

**Classical and Differentiable Numerical Solvers for Nonlinear PDEs.** Traditional solvers for strongly nonlinear PDEs typically discretize the spatial and temporal domains finely and approximate nonlinear operators locally via linearization or low-order Taylor expansions. The central method families include finite difference (FDM), finite volume (FVM), finite element (FEM), and spectral / pseudospectral methods. FDM replaces derivatives with finite differences on structured grids, offering ease of implementation and efficiency for simple geometries, but is constrained by stability conditions (e.g. CFL) and struggles with complex boundaries. FVM enforces conservation over control volumes via flux balances at interfaces (e.g., Godunov, MUSCL, WENO schemes), making it a staple in computational fluid dynamics and shock-dominated flows thanks to its robustness and local conservation property. FEM casts PDEs in variational form and uses piecewise polynomial bases on unstructured meshes, which enables flexible handling of complex geometries and boundary conditions with  $h$ -,  $p$ -, or  $hp$ -refinements, but at the cost of constructing and solving large sparse systems, mesh generation burden, and solver overhead. Spectral and pseudospectral methods expand the solution in global basis functions (e.g. Fourier, Chebyshev); they offer exponential (or very high) convergence for smooth solutions and high accuracy per degree of freedom, but are vulnerable to Gibbs oscillations near discontinuities and less adaptable to irregular domains. Hybrid or spectral-element variants combine high-order accuracy with local meshing flexibility [22, 6]. In practice, especially for long-time integration or multi-scale, strongly nonlinear problems, all of these methods demand extremely fine meshes and small timesteps to maintain stability and accuracy, leading to very large memory and computational cost, difficulties in solver scaling, stiffness, preconditioning needs, and nontrivial meshing workflows. In industrial settings—from aerospace CFD to structural analysis—FVM and FEM remain predominant, yet their limitations in scalability, adaptivity, solver tuning, and the cost of repeated solves (e.g. in optimization, design, uncertainty quantification) persist as major pain points.

Beyond classical solvers and purely neural approaches, a hybrid paradigm has emerged in which numerical PDE solvers are made *differentiable* (i.e. permit gradient propagation via automatic differentiation or adjoint methods), enabling them to be embedded within learning pipelines or coupled end-to-end with neural networks. The essential idea is that each step (or block) of the solver—time stepping, spatial discretization, linear/nonlinear solves, flux evaluations, implicit updates, etc.—is implemented such that it not only computes forward results but also supports computation of derivatives w.r.t. inputs, boundary/initial conditions, or parameters. In effect, the solver becomes a differentiable operator in the computation graph, allowing backpropagation or adjoint-based gradient flow through the numerical method [71, 71, 68].

In practice, differentiable solvers are implemented by wrapping classical discretization routines (e.g. finite difference, finite volume, finite element, spectral) in AD-capable frameworks (e.g. JAX, PyTorch) or by implementing custom backward/adjoint routines. For instance, the “Solver-in-the-Loop” approach integrates an iterative PDE solver into the training loop, enabling neural network correction modules to influence and receive gradients through solver iterations [71]. Similarly, differentiable physics toolkits like  $\Phi$ Flow provide simulation primitives (e.g. diffusion, advection, projection) that interface with ML toolkits so gradients can flow through fluid solvers, particle systems, or grid updates [15]. More generically, the differentiable physics abstraction allows users to build composite models by coupling neural networks and PDE modules, while the framework handles the derivative bookkeeping and code generation [5].

One notable application is in physics-informed reduced order modeling ( $\Phi$ -ROM), where a differentiable PDE solver is embedded during training so that the learned latent dynamics respect the discretized physics; this improves generalization and long-time forecasting compared to purely data-driven ROMs [11]. In the hybrid modeling domain, frameworks such as Im-PiNDiff adopt implicit fixed-point neural layers combined with adjoint-based derivatives to provide stable, long-horizon differentiable solvers for spatiotemporal PDEs [4].

**Neural Operators: Learning Operators in Function Space.** Neural operators generalize classical neural networks (universal function approximators) into universal *operator* approximators: they learn mappings between function spaces. In the context of PDEs, a neural operator takes as input a function (e.g. the initial condition or forcing field) and returns the solution function at some later time or under different parameters, thereby avoiding explicit step-by-step integration in time. Among leading architectures are the Fourier Neural Operator (FNO) [39] and DeepONet [44, 46].

In FNO, one parameterizes the integral kernel in Fourier space: each layer transforms the input via a truncated Fourier transform, linear operations on selected low-frequency modes, and an inverse transform, interleaved with nonlinear activations. This is equivalent to performing a global convolution in physical space, but operating efficiently in spectral domain [39, 41]. Because only lower modes are retained, FNO uses relatively few spectral coefficients, enabling compact models and fast inference. In effect, FNO “compresses” what traditional solvers would do through many fine time steps into learned spectral coefficient transformations—its layers do *not* correspond to physical time steps, but learn to map from initial to final states (or coarse-interval states) in a learned composite fashion.

DeepONet is built upon the universal operator approximation theorem, which states that neural networks can approximate continuous operators. It consists of two sub-networks: a *branch net* that encodes the input function (via its values at sensor points) and a *trunk net* that encodes the output locations (query points). The output is formed via a (dot-product-like) combination of branch and trunk outputs, allowing the network to predict the value of the solution function at arbitrary spatial points [44, 46]. DeepONet is flexible and mesh-agnostic in its output querying.

These neural-operator methods have notable advantages over classical solvers. (1) They can bypass extremely fine temporal recursion: instead of marching forward with tiny time steps (as in 1D Burgers, e.g.), the operator may directly map from the input to a later time. (2) Their model parameter counts and inference cost are often much smaller than the total size of the spatio-temporal discretization used by classical solvers, thanks to spectral truncation and few layers. (3) Their interpolation / smoothness bias helps avoid numerical blow-up or Gibbs-type oscillations when temporal or spatial resolution is coarse, because predictions stay near the training-output manifold. However, these methods also have limitations: they are typically trained on in-distribution inputs and may generalize poorly to out-of-distribution (OOD) cases; their spectral truncation may lose fine-scale features; and their learned layers lack explicit physical interpretability or guaranteed stability.

In summary, FNO and DeepONet exemplify two successful neural operator designs: FNO leverages spectral domain operations and compact Fourier-mode parameterization; DeepONet embraces a dual-network strategy to make queryable operator approximations over continuous domains. Each offers a distinct balance between expressivity, efficiency, and generalization.

**Active learning and adversarial sampling for PINNs.** Physics-informed neural networks (PINNs) treat the neural network as a surrogate solution function  $u_\theta(x, t)$  and minimize a composite loss that combines data/BC/IC terms with PDE residuals evaluated at collocation points in space–time [58, 57]. A central challenge in PINN training is selecting these collocation points: a small subset of “hard” points (e.g., shocks, boundary layers, or steep gradients) frequently dominates the global generalization error, so naive uniform sampling can waste budget on easy regions while failing to resolve failure regions [77, 81]. To address this, the literature has developed three broad families of sampling strategies: (1) *uncertainty-driven* methods that estimate epistemic uncertainty (e.g., MC-Dropout, Bayesian surrogates) and sample where uncertainty is high; (2) *residual-driven* methods that add or reweight collocation points in regions of large PDE residual (e.g., RAR/RAD/RAR-D and importance sampling); and (3) *representativeness/diversity* heuristics (e.g., Latin Hypercube Sampling, mesh-refinement or reduced-order surrogate guided selection) that preserve global coverage while avoiding oversampling concentrated clusters [53, 77, 70, 56].

A particularly effective and practically attractive variant borrows adversarial machinery from classification/regression: PGD-style attacks are used to *move* collocation points along the gradient of the physics loss with respect to the input coordinates (i.e., use the PINN’s built-in autodiff to compute  $\nabla_{(x,t)}\mathcal{R}(x, t)$  and take constrained ascent steps), producing “hard” locations where the PDE residual is amplified; these adversarial locations are then used for fine-tuning (adversarial training, AT-PINN / PIAT and related methods). Critically, practitioners commonly initialize points with space-filling designs such as Latin Hypercube Sampling (LHS) and restrict the PGD/step budget so the moved points (i) migrate toward residual maxima while (ii) avoiding pathological concentration and thus retaining diversity and domain representativeness [37, 33]. This procedure has two pragmatic advantages: it (a) does not require a parametric prior over the residual distribution (no Gaussian / GMM assumptions), and (b) directly probes the true residual landscape induced by the current network, thereby locating realistic failure regions for targeted refinement [37, 42].

Although PINN adversarial sampling is defined in a low-dimensional Euclidean input domain (space–time coordinates), the underlying PGD principle readily generalizes conceptually to neural operators (NOs): instead of perturbing coordinates we can search the high-dimensional function space in a local neighborhood of each training function (an  $\varepsilon$ -ball in coefficient or spectral space) for small, spectrum/energy-constrained perturbations that maximally increase the operator loss. Concretely, for NOs one may (i) start from a baseline distribution of functions (e.g., GRF samples), (ii) define a physically meaningful perturbation norm (e.g., an  $L^2$  or weighted spectral norm, or constraints on power in certain frequency bands), and (iii) perform constrained ascent in that function space to find worst-case neighbors to include in adversarial augmentation. This function-space PGD both preserves the desirable property of not assuming a residual prior and effectively explores the model’s local robustness within the concentrated manifold induced by the training distribution — a crucial capability for NOs where the discrete inputs are extremely high dimensional and classical PINN coordinate-moving tactics are not directly applicable [40, 45, 37].

**PGD attack on FNO.** Adesoji et al. provide an early, practical study of PGD adversarial attacks on Fourier Neural Operators (FNOs) and demonstrate that FNO errors can grow rapidly under  $\ell_\infty$  perturbations [3]. However, their implementation makes two pragmatic approximations that are important to highlight. First, because re-running a high-fidelity PDE solver for every perturbed input at every PGD step would impose prohibitive wall-time and memory costs, they do not solve the PDE on the fly for each perturbation. Instead, they precompute a large dictionary of input fields and corresponding solver outputs (thousands of GRF samples) drawn from the same distribution used to train the FNO, and during an attack they locate a nearest-neighbor entry in this dictionary to serve as an approximate “ground truth” for the current perturbed input [3, Sec. 3.1]. This nearest-neighbor surrogate makes the attack tractable in practice but implicitly assumes that the solver response for a perturbed input is well approximated by the solver output of a nearby precomputed sample — an approximation that can be poor where solver outputs vary nonlinearly with input (e.g., near shocks, bifurcations, or other sensitive regimes).

Second, and crucially, their procedure backpropagates gradients only through the FNO; the solver is

treated as a fixed reference and no gradient information from the solver (or a differentiable solver implementation) is propagated back into the attack or defense loop. Operationally, this is equivalent to assuming that while the FNO’s prediction changes with the input perturbation, the solver’s true output does not (or has zero gradient)—an assumption that is generally false: both the learned operator and the numerical solver produce outputs that change with input, and therefore the solver itself has nontrivial sensitivity to perturbations. The combination of (i) using a dictionary lookup as an approximate ground truth and (ii) omitting solver gradients biases the attack optimization and can mischaracterize both vulnerability and robustness; these choices were almost certainly made to avoid the very large runtime and memory burden of differentiating through a full high-fidelity solver (or because a differentiable solver implementation was unavailable), but they introduce a mismatch between the attack objective and the actual solver-level worst-case behavior.

By contrast, differentiable-solver or “solver-in-the-loop” approaches explicitly integrate the numerical solver into the computational graph so gradients can flow through the solver’s forward iterations; this removes the surrogate/dictionary approximation and captures how the solver output itself shifts under perturbations, at the price of substantial additional computation and memory usage (cf. [71]). For rigorous evaluation of operator robustness, one should therefore weigh the trade-offs: dictionary surrogates and solver-free gradient shortcuts make large-scale experiments feasible, but they can under- or mis-estimate worst-case behaviors that would be exposed when the solver is actually re-executed (or differentiated) for each perturbed input. Finally, good adversarial evaluation practice requires care to avoid such approximation pitfalls and to report their potential impacts on conclusions.

**Knowledge Distillation and Representation Alignment.** Knowledge distillation (KD) enables transferring “knowledge” from a pre-trained *teacher* to a more efficient *student*. The classic form—*vanilla KD* or response-based distillation—teaches the student to mimic the teacher’s softened output logits via a KL divergence loss [24, 20]. However, it ignores the teacher’s intermediate representations.

To capture more structure, *feature-based distillation* (also called hint-based or intermediate-layer distillation) enforces the student to mimic internal activations (or feature maps) of the teacher, typically projecting between different feature spaces and applying alignment losses (e.g. L2, attention-weighted) [61, 26]. A third class, *relation-based distillation*, transfers knowledge about relationships (e.g. similarity patterns, pairwise distances) among features [34].

In the neural operator / PDE surrogate setting, one may ask whether internal representations correspond to meaningful “time-stepping” quantities. One can use XAI techniques (attribution, clustering, relevance maps) to test alignment. But since teacher and student may have different architectures or bases, naive feature alignment often suffers from *feature misalignment* or *representation mismatch*.

In practice, KD works indirectly: the teacher emits responses or features as supervision, and the student learns to imitate them under its own parameterization. You cannot directly “copy the teacher’s brain.” In this work, a solver acts as teacher, and a leaner operator is student. Feature-based / ILD is promising—if you design suitable projection or adapters to align representations despite architectural differences.

**Adversarial Training for Better Generalizability and Robustness** Adversarial training (AT) improves generalization and robustness by converting learning into a min–max optimization: for each input, an inner PGD-style search finds worst-case perturbations within a norm ball, and the outer loop updates model parameters to minimize error on those adversarial examples, pushing the model to learn more stable, perturbation-resistant features and avoid overfitting to spurious cues [48, 17]. Beyond robustness to attacks, recent works show that AT can help with out-of-distribution generalization or improved test performance under shifted or noisy conditions [82, 83]. On the theoretical side, analyses such as “On the Generalization Properties of Adversarial Training” explore conditions under which AT leads to consistent robust estimators and characterize trade-offs between robustness and generalization in linear and neural regimes [79]. In this operator learning context, adversarial training can broaden the effective support of training data in function space, forcing the neural operator to generalize not just on nominal data but also locally perturbed variants, which may improve stability under small input shifts or modeling noise.

## Methods

**Neural Operator Model  $G$**  Let the input function space be  $\mathcal{A} = A(D; \mathbb{R}^{d_a})$ , the hidden function space  $\mathcal{V} = V(D; \mathbb{R}^{d_v})$ , and the output function space  $\mathcal{U} = U(D; \mathbb{R}^{d_v})$ . Optionally introduce pointwise mappings

$$\mathcal{P}_{\text{in}} : \mathcal{A} \rightarrow \mathcal{V}, \quad \mathcal{P}_{\text{out}} : \mathcal{V} \rightarrow \mathcal{U}.$$

Initialize

$$v_0(x) = \mathcal{P}_{\text{in}}(a)(x).$$

Then iterate for  $t = 0, 1, \dots, T - 1$ :

$$v_{t+1}(x) = \sigma(W v_t(x) + \mathcal{K}(a; \theta)[v_t](x)),$$

where  $W : \mathbb{R}^{d_v} \rightarrow \mathbb{R}^{d_v}$  is a linear map and  $\mathcal{K}(a; \theta)$  is a kernel integral operator (e.g. in FNO, implemented via multiplication in Fourier domain). Finally the output is

$$G(a) = \mathcal{P}_{\text{out}}(v_T(\cdot)).$$

**Classical Numerical Solver  $g$**  Consider a time-dependent PDE with initial condition  $u(x, 0) = a(x)$ , and let the goal be to compute  $u(x, T)$ . Define

$$g : \mathcal{A} \rightarrow \mathcal{U}, \quad g(a) = u^N,$$

where  $u^n$  is advanced in time by

$$u^{n+1} = \Phi_{\Delta t}(u^n), \quad n = 0, 1, \dots, N - 1, \quad u^0 = a.$$

Hence

$$g(a) = (\Phi_{\Delta t})^{\circ N}(a).$$

In spectral or pseudo-spectral methods, each time step typically involves: Fourier transform of  $u^n$ , multiplication by frequency-domain linear operator, handling nonlinear terms (in real space or transform back), and inverse transform to produce  $u^{n+1}$ .

Both  $G$  and  $g$  effect a mapping  $\mathcal{A} \rightarrow \mathcal{U}$ .  $G$  uses a small number of ‘‘layers’’  $T$ , each acting globally over the domain;  $g$  uses a large number of time steps  $N$ . In implementation, both require discretization (grid sampling, tensor representation), so that integral, convolution, or Fourier operators become linear algebra or FFT operations. We simply refer to

$$G : \mathcal{A} \rightarrow \mathcal{U}, \quad g : \mathcal{A} \rightarrow \mathcal{U}$$

to denote the neural operator and the classical solver, respectively.

**Back Propagation and Derivative** Both operators  $G, g$  map a common input  $a$  to output functions  $G(a), g(a) \in \mathcal{U}$ . We define a loss functional  $\mathcal{L}(G(a), g(a))$  and obtain the scalar loss  $\ell(a) = \mathcal{L}(G(a), g(a))$ .

In the infinite-dimensional setting, we consider the Fréchet derivative

$$D\ell(a) : \mathcal{A} \rightarrow \mathbb{R}$$

which captures how small perturbations  $\delta a$  map to first-order changes in  $\ell(a)$ . Concretely, via the chain rule in Banach spaces,

$$D\ell(a) = D\mathcal{L}(G(a), g(a)) \circ (DG(a), Dg(a)).$$

When implemented in practice, we discretize the functions and operators on a mesh / grid, and the Fréchet derivative in the discrete representation becomes the ordinary gradient (or Jacobian) used in backpropagation.

We intentionally used MSE as loss instead of the L-p relative loss as in original FNO paper, because the relative loss inherently allows larger absolute error when the average ground truth absolute value is larger. This assumes that FNO can have larger deviation when ground truth’s norm is larger and thus assumes worse generalization in such cases.

Assume we use squared loss and difference as error

$$\ell(a) = \|G(a) - g(a)\|_2^2, \quad e(a) := G(a) - g(a)$$

. Jacobians:  $J_G(a)$ ,  $J_g(a)$  are the Jacobians of  $G$  and  $g$  w.r.t.  $a$ .

(1) Full / with-solver version

Chain rule through both  $G$  and  $g$ :

$$\nabla_a \tilde{\ell}(a) = 2 (J_G(a) - J_g(a))^\top (G(a) - g(a))$$

(2) Detached version (use the true  $g(a)$  in the forward pass, but stop gradient through  $g$ )

The operator `sg` returns its input in value but has zero derivative (stop-gradient, only function forward but no gradient backward).

$$\hat{\ell}(a) := \|G(a) - \text{sg}(g(a))\|_2^2, \quad \nabla_a \hat{\ell}(a) = 2 J_G(a)^\top (G(a) - g(a))$$

(3) Approximated version (dictionary proxy for  $g$  and no grad through  $g$ )

Use a nearest neighbor  $\tilde{a}(a)$  from a fixed dictionary "dict" to define a proxy  $\tilde{g}(a) = g(\tilde{a}(a))$ .

Then ignore the dependence of  $\tilde{g}$  on  $a$  (no function forward and gradient backward path through  $g$ ).

$$\tilde{a}(a) := \arg \min_{b \in \text{dict}} \|a - b\|, \quad \tilde{g}(a) := g(\tilde{a}(a)), \quad \tilde{\ell}(a) := \|G(a) - \tilde{g}(a)\|_2^2,$$

$$\nabla_a \tilde{\ell}(a) \approx 2 J_G(a)^\top (G(a) - \tilde{g}(a))$$

Under some circumstances (simpler tasks, or L inf PGD attack), the difference between some of them could be minimal, especially in L inf PGD attack, between full and detached, because L inf PGD attack only takes the sign of input elementwise, and these two gradients have very similar signs. Approximated PDE solver ground truth has larger negative effect in find the true gradient to the real loss.

**Choice of Loss Function** In selecting an appropriate loss, we found that a naive *cell-wise* / *pixel-wise* difference metric is ill-suited for our experimental setting. In our problem, we impose periodic boundary conditions: conceptually, there is no fixed boundary, the edges are connected and flow can move freely across them, and the domain is topologically equivalent to a torus. Since our Navier–Stokes (NS) equations are defined over a two-dimensional spatial domain, we in effect work on a 2D torus. Suppose the final state of the NS solution exhibits exactly the same pattern, but merely shifted spatially. A pixel-wise loss would register a large error, while perceptually the shifted pattern appears identical. To distinguish *true pattern differences* from mere spatial translations or local stretch/compression, we consider two advanced loss strategies: DTW (Dynamic Time Warping) and perceptual loss.

For one-dimensional discrete signals  $x, y$ , DTW aligns them via dynamic programming:

$$\text{DTW}(x, y) = \min_{\pi \in \mathcal{A}} \sum_{(i,j) \in \pi} d(x_i, y_j),$$

where  $\mathcal{A}$  is the set of monotonic alignment paths. The time complexity is  $O(mn)$ . To preserve local monotonic stretching / compression, the alignment steps are restricted (e.g. right, down, diagonal), disallowing reverse moves. In the unconstrained case (no band restrictions), one must evaluate all  $m \times n$  cells to compute the DTW loss, which is expensive. Moreover, the min operator can induce *path switching* — tiny perturbations in the inputs may cause the optimal alignment  $\pi$  to change abruptly, making the loss non-differentiable at those points.

To ameliorate this, we adopt soft-DTW [10], which replaces the hard minimum over paths by a “soft-min” (a log-sum-exp smoothing) over all alignment costs:

$$\text{soft-DTW}^\gamma(x, y) = -\gamma \log \left( \sum_{\pi \in \mathcal{A}} \exp(-C(\pi)/\gamma) \right),$$

where  $C(\pi) = \sum_{(i,j) \in \pi} d(x_i, y_j)$ . This smoothing yields a differentiable loss (for  $\gamma > 0$ ), while retaining a close relationship to the DTW geometry. The authors show both the value and gradient can be computed in  $O(mn)$  time and space [10].

However, soft-DTW does not perfectly preserve the *translation invariance* that DTW ideally possesses: a pure spatial shift may still incur nonzero cost under soft alignment. Another fundamental challenge lies in extending DTW to two-dimensional pattern alignment (i.e. image warping). For 2D signals, even with restrictive assumptions, Lei and Govindaraju’s method “2D Dynamic Warping” (2DDW) exhibits worst-case complexity  $O(N^6)$  [36], and in general elastic image matching problems have been proven to be NP-complete [31]. These results make practical deployment of full 2D DTW-style alignment infeasible for moderate image sizes.

Given these computational and differentiability constraints, we draw inspiration from Youzuo Lin et al.’s work in full waveform inversion (FWI), wherein they employ a perceptual loss: the images are passed through a pre-trained deep network (specifically VGG-16) and losses are computed on intermediate feature representations rather than raw pixels [28, 29]. Their approach requires only a single forward pass and is orders of magnitude faster for 2D image domains. In effect, the perceptual loss abstracts away pixel-by-pixel differences into feature-space consistency, making it more suitable for our toroidal NS setting.

**Batch Derivative** Let  $X = \mathcal{A}$  and  $Y = \mathcal{U}$  be Banach spaces. For a batch  $\mathbf{a} = (a_1, \dots, a_k) \in X^k$ , define

$$\ell_{\text{batch}}(\mathbf{a}) := \sum_{i=1}^k \mathcal{L}(G(a_i), g(a_i)) = \left( \sum_{i=1}^k \text{id}_{\mathbb{R}} \right) \circ \underbrace{(\mathcal{L} \circ (G, g))^{\times k}}_{X^k \rightarrow \mathbb{R}^k}(\mathbf{a}).$$

Assume  $\mathcal{L} : Y \times Y \rightarrow \mathbb{R}$ ,  $G, g : X \rightarrow Y$  are Fréchet differentiable at each  $a_i$ . By the chain rule in Banach spaces and linearity of the Fréchet derivative (sum rule),

$$D\ell_{\text{batch}}(\mathbf{a}) = \sum_{i=1}^k D(\mathcal{L} \circ (G, g))(a_i) = \sum_{i=1}^k D\mathcal{L}(G(a_i), g(a_i)) \circ (DG(a_i), Dg(a_i)).$$

Equivalently, viewing  $D\ell_{\text{batch}}(\mathbf{a}) \in (X^k)^* \cong X^* \times \dots \times X^*$ ,

$$D\ell_{\text{batch}}(\mathbf{a}) = (D\ell(a_1), \dots, D\ell(a_k)), \quad \text{where } \ell(a) = \mathcal{L}(G(a), g(a)).$$

Thus the batch Fréchet derivative is exactly the tuple (i.e., concatenation) of the per-sample Fréchet derivatives. If the batch loss is the average,  $\ell_{\text{avg}} = \frac{1}{k} \sum_i \ell(a_i)$ , then  $D\ell_{\text{avg}}(\mathbf{a}) = \frac{1}{k} D\ell_{\text{batch}}(\mathbf{a})$ .

This tells we can use batch method to accelerate the computation of gradient of loss against input function  $a$ . This method will take larger memory and longer total time but less time per input as later experiments suggest.

**PGD adversarial attack** We discretize functions and operators on a mesh so that the Fréchet derivative  $D\ell(a)$  becomes the ordinary gradient  $\nabla_a \ell$  used in backpropagation; the adversary therefore performs first-order optimization in the discrete input space. (See Madry et al. for the PGD formulation.)<sup>1</sup> [47]

Below  $\ell(x)$  denotes the scalar loss for discrete input  $x$  (corresponding to  $\ell(a)$  in the continuous notation); we consider untargeted attacks that maximize  $\ell$ .

### PGD in the $L_\infty$ ball

given: original input  $x_0 = a$ ,  $\epsilon > 0$ ,  $\alpha > 0$ ,  $T \in \mathbb{N}$ ,  
 init  $x^{(0)} \leftarrow x_0 + \xi$ ,  $\xi \sim \text{Uniform}([- \epsilon, \epsilon])$  (optional random start)  
 for  $t = 0, \dots, T - 1$  :  
 $g^{(t)} = \nabla_x \ell(x^{(t)})$   
 $x^{(t+1)} = \Pi_{\| \cdot - x_0 \|_\infty \leq \epsilon}(x^{(t)} + \alpha \cdot \text{sign}(g^{(t)}))$   
 $x^{(t+1)} = \text{clip}(x^{(t+1)}, x_{\min}, x_{\max})$  (optional domain clip)  
 return  $x^{(T)}$ .

Here  $\Pi_{\| \cdot - x_0 \|_\infty \leq \epsilon}$  denotes projection onto the  $L_\infty$  ball around  $x_0$  (i.e. elementwise clamp to  $[x_0 - \epsilon, x_0 + \epsilon]$ ). This is the standard PGD (Madry) variant. [47]

<sup>1</sup>Madry et al., “Towards Deep Learning Models Resistant to Adversarial Examples”, 2017.

## PGD in the $L_2$ ball

given:  $x_0 = a$ ,  $\epsilon > 0$ ,  $\alpha > 0$ ,  $T \in \mathbb{N}$ ,  
 $x^{(0)} \leftarrow x_0 + \xi$ ,  $\xi \sim \text{Uniform on } \{\|\xi\|_2 \leq \epsilon\}$  (optional)  
for  $t = 0, \dots, T - 1$  :  
 $g^{(t)} = \nabla_x \ell(x^{(t)})$   
 $\tilde{g}^{(t)} = \frac{g^{(t)}}{\|g^{(t)}\|_2 + \delta}$  ( $\delta$  small for stability)  
 $x^{(t+1)} = x^{(t)} + \alpha \tilde{g}^{(t)}$   
if  $\|x^{(t+1)} - x_0\|_2 > \epsilon$ ,  $x^{(t+1)} \leftarrow x_0 + \epsilon \cdot \frac{x^{(t+1)} - x_0}{\|x^{(t+1)} - x_0\|_2}$   
 $x^{(t+1)} = \text{clip}(x^{(t+1)}, x_{\min}, x_{\max})$   
return  $x^{(T)}$ .

The  $L_2$  variant uses the (normalized) gradient direction and projects back to the  $L_2$  ball when necessary; see practical recipes for  $L_p$  PGD implementations.

In implementation, we choose to use Adam in the PGD attack for the update based on gradients to achieve smoother loss progression and obtain steady loss increase.

---

### Algorithm 1 PGD with Adam-style adaptive direction ( $L_2$ -constrained)

---

**Require:**  $x_0$ ,  $\epsilon > 0$ ,  $\alpha > 0$ , steps  $T$ ,  $\beta_1, \beta_2 \in [0, 1)$ ,  $\text{adam\_eps} > 0$ ,  $\delta_{\text{stab}} > 0$ , optional  $x_{\min}, x_{\max}$

**Ensure:**  $x^{(T)}$  with  $\|x^{(T)} - x_0\|_2 \leq \epsilon$

```

1: (Optional random start) set  $x^{(0)} \leftarrow x_0 + \text{Uniform}_{L_2.\text{ball}}(\epsilon)$  or  $x^{(0)} \leftarrow x_0$ 
2:  $m \leftarrow 0$ ;  $v \leftarrow 0$ ;  $t_{\text{adam}} \leftarrow 0$ 
3: for  $t = 0$  to  $T - 1$  do
4:    $t_{\text{adam}} \leftarrow t_{\text{adam}} + 1$ 
5:    $g \leftarrow \nabla_x \ell(x^{(t)})$  # maximize the loss
6:    $m \leftarrow \beta_1 m + (1 - \beta_1)g$ 
7:    $v \leftarrow \beta_2 v + (1 - \beta_2)(g \odot g)$ 
8:    $\hat{m} \leftarrow m / (1 - \beta_1^{t_{\text{adam}}})$ ;  $\hat{v} \leftarrow v / (1 - \beta_2^{t_{\text{adam}}})$ 
9:    $d \leftarrow \hat{m} / (\sqrt{\hat{v}} + \text{adam\_eps})$ 
10:   $d_{\text{norm}} \leftarrow \|d\|_2$ 
11:  if  $d_{\text{norm}} < 10^{-12}$  then
12:     $u \leftarrow d$ 
13:  else
14:     $u \leftarrow d / (d_{\text{norm}} + \delta_{\text{stab}})$ 
15:  end if
16:   $x' \leftarrow x^{(t)} + \alpha u$ 
17:   $\Delta \leftarrow x' - x_0$ ;  $\Delta_{\text{norm}} \leftarrow \|\Delta\|_2$ 
18:  if  $\Delta_{\text{norm}} > \epsilon$  then
19:     $\Delta \leftarrow \Delta \cdot \frac{\epsilon}{\Delta_{\text{norm}} + 10^{-12}}$ ;  $x^{(t+1)} \leftarrow x_0 + \Delta$ 
20:  else
21:     $x^{(t+1)} \leftarrow x'$ 
22:  end if
23:   $x^{(t+1)} \leftarrow \text{clip}(x^{(t+1)}, x_{\min}, x_{\max})$ 
24: end for
25: return  $x^{(T)}$ 

```

---

**Notes:**  $\odot$  denotes elementwise product. The routine maximizes  $\ell$  by following an Adam-adapted direction  $d$ , then projects back to the  $L_2$  ball  $\{x : \|x - x_0\|_2 \leq \epsilon\}$  to enforce the perturbation constraint. Normalizing  $d$  (step 4) makes  $\alpha$  act as a controlled  $L_2$  step-size; omitting normalization uses the raw Adam step instead.

$\epsilon$  and  $\alpha$  are important parameters here as they define how large the final perturbation is and how fast the perturbation grows.

We chose L2-norm PGD attack because it gives smoother perturbed inputs which are more realistic as initial conditions in this physics context.

In reality, because the solver can give blow-up final condition when input is perturbed to a certain state during the PGD attack. We employed a combined method of adaptive time stepping step size and attack total steps' limit to solve this. We keep a list of gradually smaller step size steps. If the forwarded loss or back propagated gradient returns infinity or NaN, it will try to use smaller steps. If after it tries all smaller steps, there is still blow-up, it will keep the perturbed input as the last non-blow-up input. We also used a small total number of steps during the attack, which is 10.

**Min–Max Optimization Framework** We consider a robust training / adversarial objective of the form

$$\min_{\theta} \max_{\|\delta\| \leq \epsilon} \ell(a + \delta; \theta),$$

where:  $\theta$  denotes the learnable parameters of the neural operator  $G$ ,  $\ell(x; \theta)$  is the loss (e.g. comparing  $G(x)$  and  $g(x)$ ),  $\delta$  is an adversarial perturbation on the input  $a$ ,  $\|\delta\| \leq \epsilon$  constrains the attack under some norm (e.g.  $L_\infty$  or  $L_2$ ).

Equivalently, for  $L_p$ -bounded perturbations:

$$\min_{\theta} \mathbb{E}_{a \sim \mathcal{D}} \left[ \max_{\|\delta\|_p \leq \epsilon} \ell(a + \delta; \theta) \right].$$

In our discretized implementation, the inner maximization is approximated via PGD, and the outer minimization is done by descending the resulting gradient with respect to  $\theta$ .

The attacking process freezes the model parameters and update inputs such that the losses are maximized, the training processes freezes the updated inputs and their respective outputs and update the model parameters such that the losses are minimized. In this continual alternating training, knowledge is transferred from the solver to the model.

We tried 2 training methods here. The first one is more like an active learning method (round by round). We train the model for N epochs, and attack the current model with the training inputs, and then replace some of the training inputs with attacked results, and train the model for the next round using the updated training dataset. The second one is more like an adversarial training method (batch by batch). Every batch of training inputs are first attacked using the current model, and we input the attacked inputs to the model for training. The model only sees attacked inputs in this process.

## Experiments

First we show the drawback of neural operators in OOD testing, and then the effectiveness of this attacking method in finding perturbed samples with larger neural operator prediction loss. Then we show the effectiveness of incorporating this attacking method into active learning to increase generalizability and robustness.

### Neural Operators in OOD testing

#### FNO1d on 1D Burgers

I generated a pool of OOD datasets, basically used different initial condition distributions, drew samples from them and used PDE solver to compute the final conditions. The distribution tested here are, gaussian kernel Gaussian Random Field, matern kernel Gaussian Random Field, and zigzag function (piecewise linear function). I altered the correlation length of kernel of gaussian GRF, the nu and correlation length of matern GRF, and the number of piecewise lines of zigzag function. I trained the FNO models on gaussian kernel GRF of correlation length 0.1 of value range (0,1). Usually GRFs are generated with value range centered around 0, here I normalizes their range to (0,1). Figure 1 shows the testing RMSE and MAE of vanilla FNO (unnormalized) and normalized FNO. I intentionally tried both unnormalized FNO and normalized FNO to

show that the bad performance of FNO to out-of-range data is not because it is not normalized. Here I used darker color to denote normalized version and lighter color to denote unnormalized version. It is obvious that for most cases, unnormalized FNO has lower errors than normalized FNO. Test and train errors are shown on the rightmost of the plot. *All\_neg* and *All\_pos* in this plot denote range (-1,0) and (0,1) respectively. The range here is the value range of the 1D tensor after normalizing it from centering around 0. We can see that FNO performs relatively well on (0,1) and (0,0.5) OOD datasets, because they have relatively similar range as the training dataset. Generally speaking, I find that FNO particularly performs badly when the input value range is much different than its training range. This is true even when the curve shape are exactly the same but just moved upwards and downwards. GRF kernel types, kernel parameters, and even not GRFs, have relatively less effect on its bad performance. This shows the interpolation and data-driven nature of neural network methods. They are not first-principle methods based on math formula like CFD method. We can see clearly that FNO has best performance on (0,0.5) and (0,1) datasets.

By analyzing the output of FNO on particular OOD samples, I find that this is largely due to the diversity of behaviors of PDE system under different initializations. The behavior of PDE system is not simply determined by hyperparameters like viscosity here in the Burgers case. Burgers equation depicts a velocity wave that travels in a direction and speed roughly related to the average magnitude and direction of the initial velocity itself. Negative and positive velocity gives totally different velocity wave propagation directions. Larger magnitude of velocity gives quicker wave propagation speed. Training FNO on velocity range (0,1) and inferring it on velocity range (0,3) gives slower wave propagation than ground truth. And FNO gives completely wrong prediction when range contains negative part when trained on only positive range. These are evident from Figure 8 to 11. In order to solve this without very sophisticated math construction, I think the best way is to let neural operators to see more diverse data automatically and actively. Any human crafted , constructed, and selected inputs will incur a lot of tedious human labor.

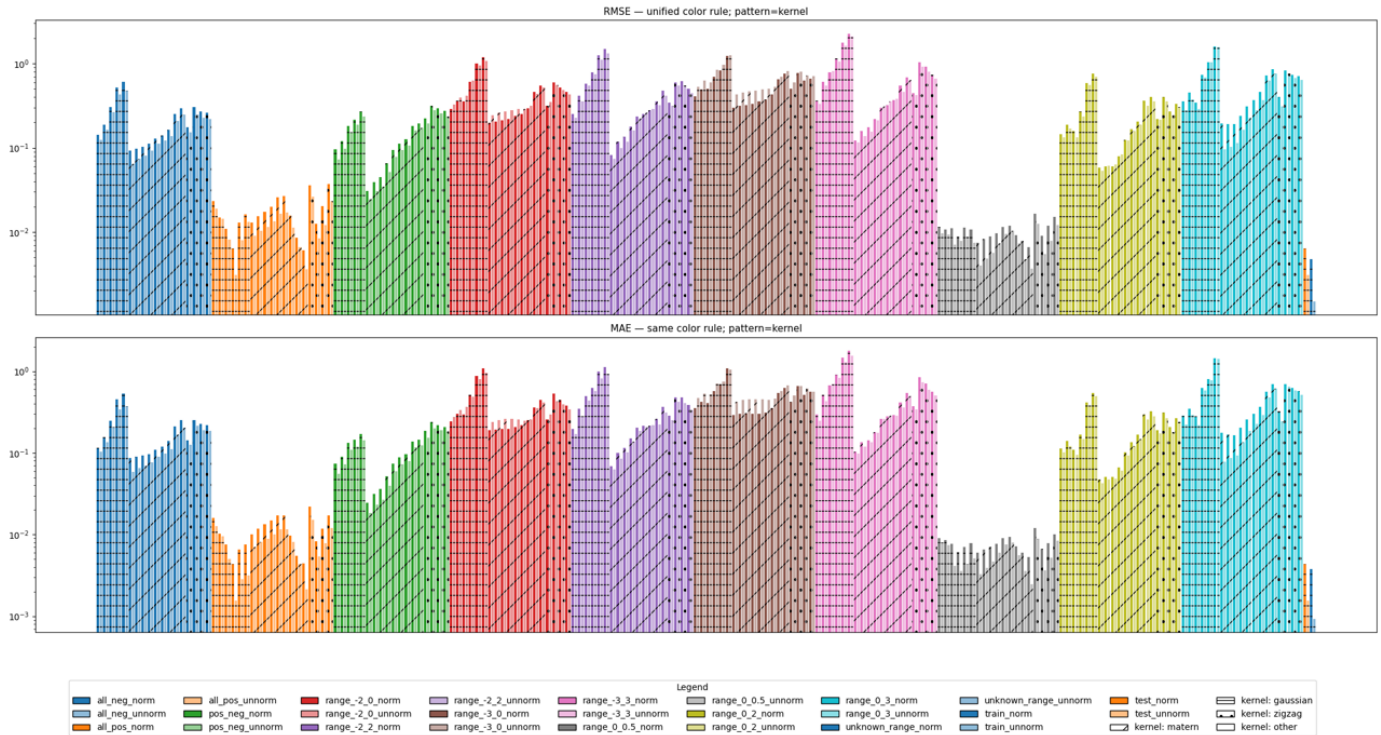


Figure 1: Unnormalized and Normalized FNO 1D Burgers OOD testing RMSE and MAE

### FNO2d on 2D Navier-Stokes equation of Vorticity-Streamfunction Formulation

I did a similar OOD test to the Navier-Stokes equation using FNO2d. The recurrent FNO model in [40] used frames 1-10 to predict frames 11-20, but here we only care about the input (frame 1) and output (frame

20). Frames 2-10 (generated by solver and inputted to FNO as part of the input) and frames 11-19 (predicted output of FNO but dropped in computing the final loss) can be seen as intermediate results needed in FNO model to do this prediction. This redundant input and output is necessary in FNO2d, as directly using frame 1 and frame 20 as input and output in training gives bad prediction performance in testing of the same input-output pairs, in my experiment. Without the information in intermediate frames, it is very hard for recurrent FNO2d to do the prediction. However the innovation of FNO lies in that the time granularity of input of FNO is much larger than numerical PDE solvers, which is 1 sec vs. 0.001 sec. I used GRFs of kernel "gaussian", "matern", "periodic" and "rq (rational quadratic)", with varying kernel parameters, as OOD initial condition, and normalized the generated GRFs to different ranges. Similar findings are obtained here, which is FNO generalizes particularly bad when the testing range is significantly different from training range. The predicted cell values of final frame are significantly skewed to the larger portion or smaller portion in these cases. The output errors of all OOD distribution are shown in Figure 2. One difference is that under the particular external forcing term in [40] (similar to Kolmogorov flow, but forcing is exerted as the curl of force of  $45^\circ$ ), some initial condition distribution gives smaller final errors than training and testing dataset. This is due to the fact that these distributions have very small pattern spatial scales. The small ups and downs in the values of neighboring cells of initial conditions are quickly smoothed out by diffusion in NS equation, and the behavior of the system becomes very simple under this circumstance, with no curvy or chaotic streamlines. The testing samples' performance are shown in Figure 12 to 16.

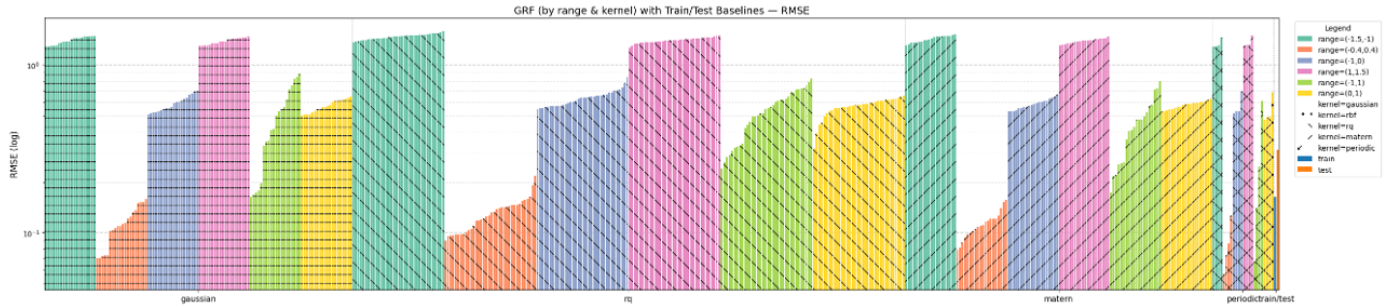


Figure 2: Unnormalized FNO 2D NS OOD testing RMSE

## PGD attack

### FNO1d on 1D Burgers

FNO1d on 1D Burgers is a relatively simple case, with one initial condition and a final condition, all of them being 1D tensors.

Figure 3 illustrates the function forward and gradient backward mechanism in PGD attack. The two pathways of forward and backward being the PDE solver and FNO. This method is called "with solver". Since the forward and backward methods take significantly longer time, we also compared our method with the detached version (PDE solver output  $x_1$  is detached, thus there is only function forward in PDE no gradient backward, solver ground truth value  $x_1$  is obtained, but PDE solver gradient is not used in back propagation to get the real gradient of loss against  $x_0$ ), and approximated version as in [3] (PDE solver is not used in this attacking process, the ground truth solver value  $x_1$  is got from an approximated value from the pre-calculated dictionary of initial-final condition pairs. No function forward and gradient backward.).

Here we tried the PGD attack of FNO on 1D Burgers of  $\nu=0.0005$  and  $\nu=0.01$ . Sample results (loss progression) are presented from Figure 17 to 18. This shows that sometimes approximated method does not always attack the model successfully, e.g. the loss may not increase steadily and keep that maximized value. With solver gradient method also has the loss growing fastest. Because for approximated method, we used the approximated final condition, we calculated 2 losses for these approximated cases, true losses are presented on the left (calculated using PDE solver ground truth final condition), surrogate losses are presented on the right, calculated using approximated final condition using input-output pairs in the pre-calculated dictionary). I notice that approximated method tend to give smaller surrogate loss in the beginning, with

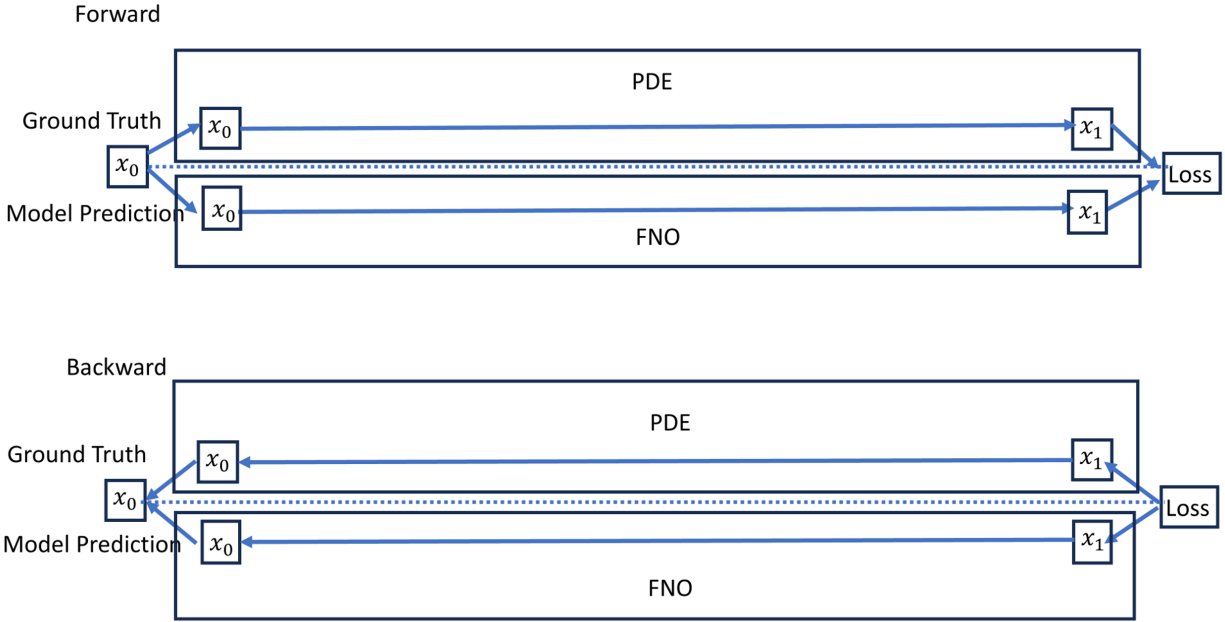


Figure 3: 1D Burgers PGD attack illustration (with solver)

the loss smaller as dictionary size increases. This surrogate loss is misleading as it uses surrogate ground truth not real ground truth. Last step perturbed inputs are shown in Figure 23. With solver gives slightly larger loss than detached and significantly larger loss than approximated.

### Using Soft-DTW as Loss

In the above, I used the pixel-wise difference mse as loss function. However, it is not good at identifying shapes or patterns in the two inputs. As here we used a periodic boundary condition, the output state can move freely across boundary with no constraint. Even if two output functions have exactly the same shape and value, but one is just a translation of another, this pixel-wise loss will identify them as different and give a large loss, while soft-DTW, a differentiable variant of DTW, will give a very small loss. Soft-DTW will give large loss when the 2 inputs are truly different in shape. Result from Figure 26 shows that using soft-DTW as loss can give more complex perturbation function with some weird curves and inflections. We see that with solver gradient back prop tend to give slower loss increase in the beginning but larger final loss in the end. I found that soft-DTW indeed will move the shock waves of ground truth farther away from the FNO output's shock wave. There is no currently implemented differentiable DTW loss method for 2D signals like images due to computation complexity, so I did not try this in 2D NS case.

### DeepONet1d on 1D Burgers

While the perturbed inputs are quite smooth and realistic in FNO1d case, the perturbations are very noisy in DeepONet1d case. This could be due to 2 reasons: 1. The test case of DeepONet here has  $\nu = 0.01$  which means stronger diffusion. Very noise initial conditions will become smooth quickly after a small time step. 2. The DeepONet model is not as robust as FNO. I did notice that DeepONet does not perform well on small  $\nu$  Burgers test cases, a lot worse than FNO, so I chose  $\nu=0.01$ . It is possible that FNO is more robust to noise as it captures global signal using Fourier transform and filters out high frequency components. Further study can be done to probe into this. Figure 24 shows the loss progression and the final perturbed inputs of 3 methods. With solver method can give the largest final loss and also fastest loss growth. Approximated method can cause loss decrease at certain step during the attack.

## FNO2d on 2D Navier-Stokes

To investigate a more complicated PDE test case, I chose the 2D Navier-Stokes case as in [39]. [39] used a FNO2d in a recurrent way. The FNO2d predicts the next frame from the input 10 frames with 1 sec time interval between them. The FNO adds the newly predicted next frame to the input frames of next prediction in a sliding window and predicts all 11 to 20 frames as output using 1 to 10 frames as input. I have tested other architecture of FNOs like FNO3d with time as a new dimension besides 2 spatial dimensions, and also directly predicting the final frame (20 sec) using initial frame (1 sec). These methods do not give as good performance as recurrent FNO2d, as shown in Figures 27 to 28. (Solely using the initial frame to predict the final frame gives totally wrong output.) I infer this is because for very complex problems like NS, time-evolving information is crucial for the final state. This poses a challenge for our attacking here, as the expected input and output of PDE solver and FNO are different. The PDE solver expects only the initial frame (1 sec) as input and only the final frame (20 sec) as output, but FNO requires frames 1-10 sec as input and frames 11-20 as output to give a satisfying prediction of the final frame. Here we still use the initial frame and final frame as the sole input and output of the whole system, but the PDE solver has to compute 2-10 sec frames as intermediate results for the input of FNO in addition to the 20 sec frame, and the last frame is sliced out of output of FNO to give the final output of the system, as shown in 4.

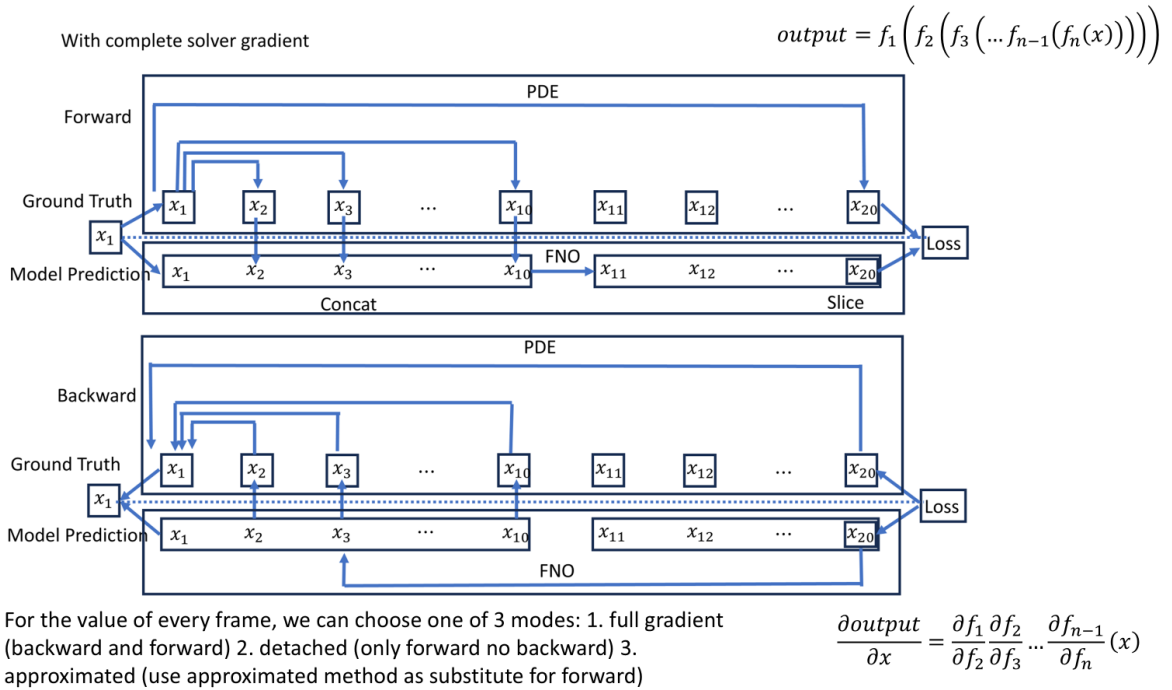


Figure 4: 2D NS PGD attack illustration (with solver)

In this attack process, every frame (2-10 and 20 frames) used here can be in 3 modes: with (used in both forward and backward propagation), detached (only used in forward propagation but detached in backward propagation), and approximated (not used in both forward and backward propagation), the same as the Burgers case’s output frame. These variants are shown in Figures 29 to 31. The ablation study shows that in this more complex NS case, PDE solver gradient backward is more crucial for the fast increase and large final loss in the attack process. While in Burgers case, with and detached mode give very similar loss progression and final loss in a lot of times, in NS case, detached mode usually gives slower loss progression and smaller final loss every time. And I found that later frames in the process is more important. Without the back prop of solver gradient of frame 20 sec, the attack fails completely, and including frames of 5-10 secs in gradient back prop is more effective than include frames of 1-4 secs. I infer this is because later frames are more different from the initial frame and are more informative of the system.

One particular interesting finding is that the perturbations generated using this PGD attack by combining

FNO and PDE solver are reflective of the external forcing exerted on the NS system. I found that when averaging the generated perturbations of all records in the dataset, the averaged result is highly similar to the external forcing pattern. This is intuitive as the external forcing determines how the system evolves and the final condition. The perturbation can only be exerted in a way according to the external forcing to maximize the final difference. When there is no external forcing, the perturbation average is a random field. Results are shown in Appendix D.10.

## Challenges in the Above PGD Attack

PGD attacks on Burgers are done using L4 GPU, and attacks on NS are done using B200 GPU. Memory and time consumption in doing these attacks is a real concern. Attacks on Burgers (batch size = 1) can be done using 20 GB of memory, while attacks (batch size = 1) on NS need memory around 30-50 GB, and the memory increases linearly with respect to batch size. When using B200, which is the GPU with largest possible memory nowadays, I can only run PGD attack on 2D NS with max batch size of 7. Batch size of more than 7 will incur OOM issue. The training of FNO in [39] has a default batch size of 20. For some attacks on Burgers of 100 steps, the time could vary between 1000-4000 seconds. For attacks on NS, the time of one update of initial condition based on gradient could be minimized to around 5.7 seconds (batch size = 1), and around 9.3 seconds (batch size = 7). Empirical results show that the backward propagation roughly takes twice the time of forward propagation. Nearly all the time and memory consumption is caused by the PDE solver. I suspect this because of the very fine spatial and temporal discretization of the data in the solver. The stored tensor is roughly  $256 \times 256 \times 4000$  (20 seconds divided by 0.005 time step). The gradient has to be back propagated through all 4000 layers, which is a huge cost. Detailed information is listed below.

Setting	Forward Time	Backward Time	FNO Time (G Time)	PDE/find Time (g Time)
with solver	0.1593	0.2870	0.0030	0.1557
detached	0.1592	0.0032	0.0028	0.1559
approximated	0.0024	0.0023	0.0022	0.0001

Table 1: PGD Attack Time Breakdown on Every Steps of 1D Burgers

with solver — forward and backward propagation both go through the PDE solver (i.e., the full solver-path is differentiable; during training gradients are back-propagated through the solver).

detached — the solver is used in the forward pass to produce outputs as ground truth, but gradients are *not* propagated back through the solver (i.e., the solver-path is detached in the backward pass).

approximated — no solver-path is used (neither forward nor backward through the solver); instead, precomputed

ground-truth/lookup values are used directly for forward passes to get surrogate ground truth, i.e., effectively no solver-path exists.

Step	Time (s)
PDE Solver Forward	1.840655
FNO Forward	0.019233
Forward Total	1.859888
Backward Propagation	3.829500
PGD Update	0.001600
<b>Full Step Total</b>	<b>5.693166</b>

Table 2: PGD Attack Time Breakdown on Every Steps of 2D NS (batch size = 1, with all solver gradient back propagated)

Step	Time (s)
PDE Solver Forward	2.684421
FNO Forward	0.059844
Forward Total	2.744265
Backward Propagation	6.563473
PGD Update	0.006794
<b>Full Step Total</b>	<b>9.316607</b>

Table 3: PGD Attack Time Breakdown on Every Step of 2D NS (batch size = 7, with all solver gradients back-propagated)

## Adversarial Training Using Above PGD Attack

I tried 2 variants of adversarial training. The first is the traditional adversarial training method: every batch of training pairs of input and output are first attacked and then input to the FNO model for training. One epoch of training in this manner takes around 3800 seconds. The second is more like an active learning method: the training and attacking alternating round by round, and training dataset is partially replaced or expanded using the attacked result of last round. One baseline method is just randomly adding a constant out of a uniform distribution to all pixel values of the initial conditions of input dataset in the training, and the training is done similarly to the first method. One epoch of training in this manner takes around 900 seconds. Results suggest that the baseline method can decrease the prediction loss of FNO across all out-of-range datasets compared to the original trained model, but it can not achieve lower loss for datasets in the same range but of different kernels and kernels' parameters. Best result comes from round-by-round method of training. At 6th round, it could achieve lower loss for nearly all datasets except datasets of range  $(-1.5, -1)$ . Results show that they could increase the loss of many datasets while decrease the loss of others. Both the batch-by-batch training and adding random constant training will cause greater loss in the original train and test datasets. Because of the memory constraint, only a batch size of 2 is allowed in batch-by-batch training. Delta losses (losses of adversarially trained models minus losses of original models) across all datasets are shown in the plots below (negative value means smaller loss than original).

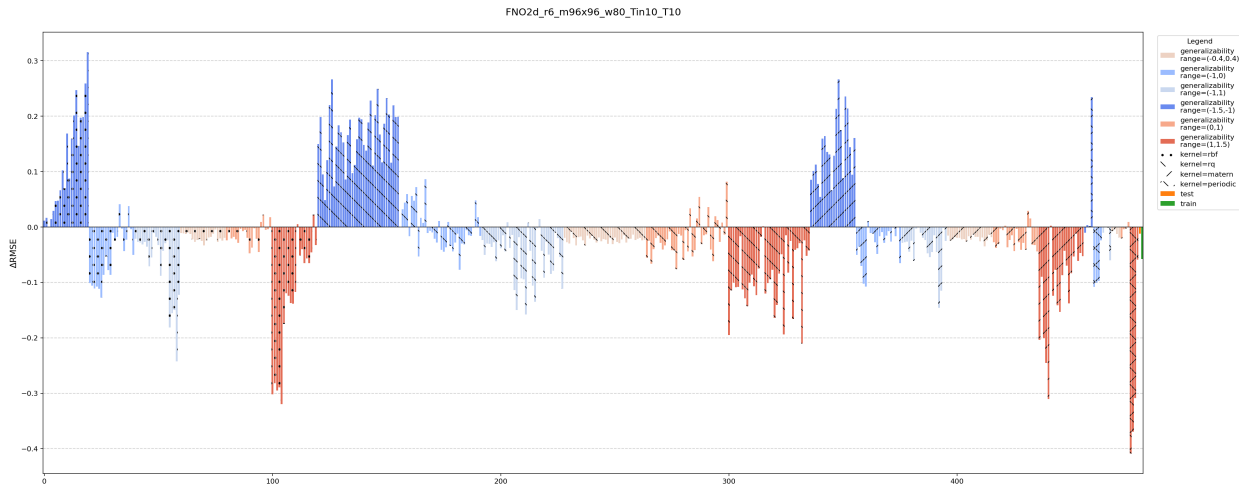


Figure 5: Loss change of round-by-round method

Generally I feel this is a difficult task due to the fact that we are trying to sample inputs in the very high dimensional function space. Because of the data-driven nature of the deep-learning model, without ingenious mathematical construction, it is hard for deep learning method to generalize well on OOD and unseen datasets. This is aggravated by the fact that using solver to generate data and use solver gradient to guide the deep learning model is extremely cost in time and memory. Also another likely hypothesis is that FNO could reach limit on its generalizability because of its relatively few parameters.

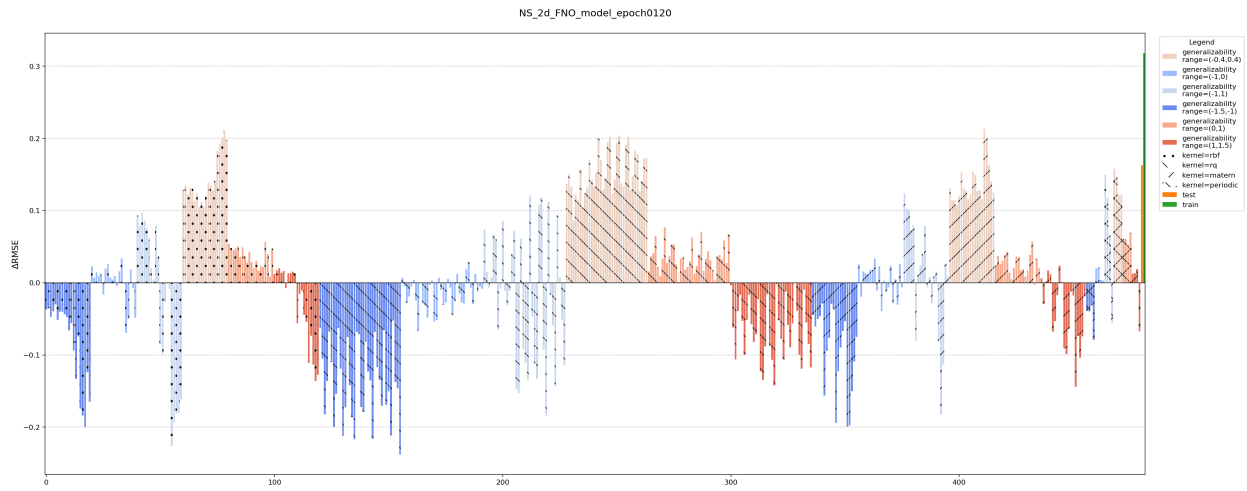


Figure 6: Loss change of batch-by-batch method

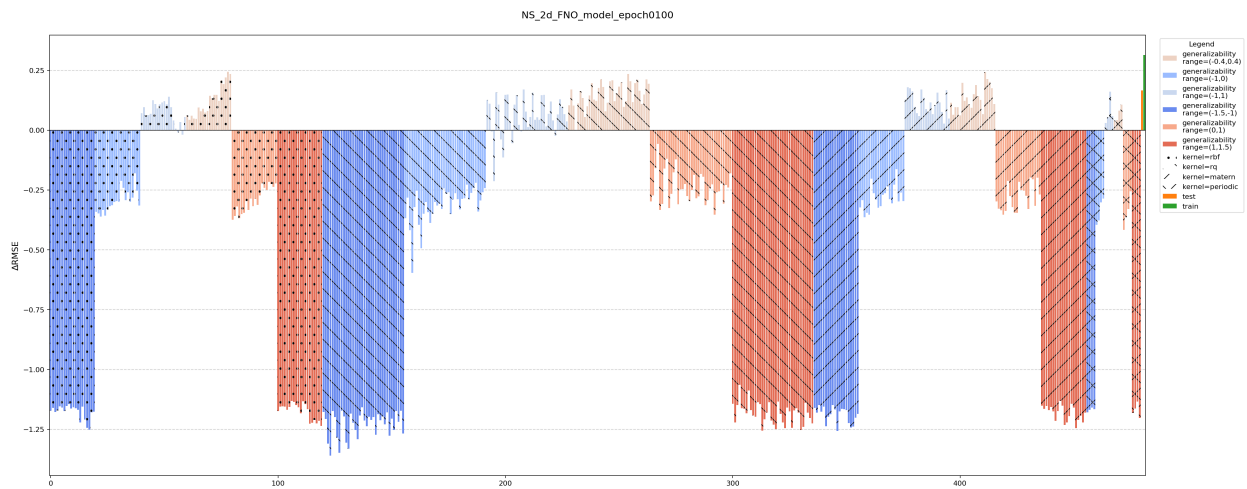


Figure 7: Loss change of random constant method

## Conclusion

I successfully implemented PGD attack by combining both neural operators and numerical solvers, address the inaccuracy of previous attack method which assumes the ground truth does not change during the attack. This gives larger final attack loss and quicker and steadier increase of attack loss, in both 1D Burgers and 2D Navier-Stokes cases. Adversarial training using this attack method can increase the generalizability of the model across most of the datasets, especially for datasets in the same range but of different kernels and kernels' parameters. However, the time and memory consumption when integrating the PDE solver is huge. Also extensive research can be done to investigate the limit of generalizability of deep learning PDE solver, and how it is related to the number of parameters of the model. I leave this challenge for the future to solve.

## Acknowledgment

I want to thank Prof Huan Zhang, Prof Gege Wen, Prof Yuanyuan Shi, Prof Shibo Li and Prof Youzuo Lin's help and support in doing this research.

## References

- [1] Dirac comb. Wikipedia, 2025. URL [https://en.wikipedia.org/wiki/Dirac\\_comb](https://en.wikipedia.org/wiki/Dirac_comb).
- [2] Matérn covariance function. Wikipedia, 2025. URL [https://en.wikipedia.org/wiki/Mat%C3%A9rn\\_covariance\\_function](https://en.wikipedia.org/wiki/Mat%C3%A9rn_covariance_function).
- [3] Adedotun Adesoji et al. Evaluating the adversarial robustness for fourier neural operator. SRML Workshop at ICLR 2022, 2022. URL <https://arxiv.org/abs/2204.04259>.
- [4] Deepak Akhare, Pan Du, Tengfei Luo, and Jian-Xun Wang. Implicit neural differential model for spatiotemporal dynamics (im-pindiff). *arXiv preprint arXiv:2504.02260*, 2025.
- [5] Nacime Bouziani, David A. Ham, and Ado Farsi. Differentiable programming across the pde and machine learning barrier. *arXiv preprint arXiv:2409.06085*, 2024.
- [6] Keaton J. Burns, Geoffrey M. Vasil, Jeffrey S. Oishi, Daniel Lecoanet, and Benjamin P. Brown. Dedalus: A flexible framework for numerical simulations with spectral methods. *Physical Review Research*, 2020. doi: 10.1103/PhysRevResearch.2.023068. URL <https://arxiv.org/abs/1905.10388>.
- [7] C. Canuto, M.Y. Hussaini, A. Quarteroni, and T.A. Zang. *Spectral Methods in Fluid Dynamics*. Springer, 1988.
- [8] Herman J.H. Clercx et al. A spectral solver for the navier–stokes equations in cylindrical geometries. *Journal of Computational Physics*, 1997. AB2 for advection, Crank–Nicolson for diffusion.
- [9] Marco Cuturi and Mathieu Blondel. Soft-DTW: a differentiable loss function for time-series. In *Proceedings of the 34th International Conference on Machine Learning (ICML)*, pages 894–903, Sydney, Australia, 2017. PMLR.
- [10] Marco Cuturi and Mathieu Blondel. Soft-dtw: a differentiable loss function for time-series. In *Proceedings of the 34th International Conference on Machine Learning (ICML)*, 2017.
- [11] Nima Hosseini Dashtbayaz, Hesam Salehipour, Adrian Butscher, and Nigel Morris. Physics-informed reduced order modeling of time-dependent pdes via differentiable solvers. *arXiv preprint arXiv:2505.14595*, 2025.
- [12] C. R. Dietrich and G. N. Newsam. Fast and exact simulation of stationary gaussian processes through circulant embedding. *SIAM Journal on Scientific Computing*, 1997.
- [13] David Duvenaud. The kernel cookbook: Advice on covariance functions, 2014. URL <https://www.cs.toronto.edu/~duvenaud/cookbook/>.
- [14] Michael Dzhibladze. Fourier series representation of periodic signals. Purdue University lecture notes, 2011. URL [https://engineering.purdue.edu/~mikedz/ee301/OW\\_CT\\_FourierSeries.pdf](https://engineering.purdue.edu/~mikedz/ee301/OW_CT_FourierSeries.pdf).
- [15] Tum-PBS / Philipp Holl et al.  $\phi$ flow: A differentiable pde solving framework. GitHub / open source. Integration with PyTorch, TensorFlow, JAX.
- [16] Konstantin Genin and Yutong Zheng. Advanced gaussian processes (scribed notes, lecture 21). CMU 10-708 Spring 2015, 2015. URL [https://www.cs.cmu.edu/~epxing/Class/10708-15/notes/10708\\_scribe\\_lecture21.pdf](https://www.cs.cmu.edu/~epxing/Class/10708-15/notes/10708_scribe_lecture21.pdf).
- [17] Ian J. Goodfellow, Jonathon Shlens, and Christian Szegedy. Explaining and harnessing adversarial examples. *arXiv preprint arXiv:1412.6572*, 2015. URL <https://arxiv.org/abs/1412.6572>.
- [18] Roe Goodman. Discrete fourier transform and wavelet transforms (math 357 notes). Technical report, Rutgers University, 2008. URL [https://sites.math.rutgers.edu/~goodman/pub/math\\_357\\_lectures.pdf](https://sites.math.rutgers.edu/~goodman/pub/math_357_lectures.pdf). Supplementary class notes, revised May 3, 2008.

- [19] Roe Goodman. Finite fourier transform, circulant matrices, and the fast fourier transform. Technical report, Rutgers University, 2015. URL <https://sites.math.rutgers.edu/~yzhuang/rci/math/fftnotes.pdf>. Supplementary notes for Math 642/550.
- [20] J. Gou et al. Knowledge distillation: A survey. *arXiv preprint arXiv:2006.05525*, 2020.
- [21] Robert M. Gray. Toeplitz and circulant matrices: A review. *Foundations and Trends in Communications and Information Theory*, 2(3):155–239, 2006.
- [22] Muhammad Bilal Hafeez and Marek Krawczuk. A review: Applications of the spectral finite element method. *Archives of Computational Methods in Engineering*, 2023. doi: 10.1007/s11831-023-09911-2. URL <https://link.springer.com/article/10.1007/s11831-023-09911-2>.
- [23] Markus Heinonen. Spectral kernels (gpss 2021). Gaussian Process Summer School slides, 2021. URL <https://gpss.cc/gpss21/slides/Heinonen2021.pdf>.
- [24] Geoffrey Hinton, Oriol Vinyals, and Jeff Dean. Distilling the knowledge in a neural network. arXiv preprint arXiv:1503.02531, 2015.
- [25] Thomas Y. Hou and Ruo Li. Computing nearly singular solutions using pseudo-spectral methods. *Communications in Computational Physics*, 2007.
- [26] Mingi Ji, Byeongho Heo, and Sungrae Park. Show, attend and distill: Knowledge distillation via attention-based feature matching. *arXiv preprint arXiv:2102.02973*, 2021.
- [27] Peng Jin, Xitong Zhang, Yinpeng Chen, Sharon Huang, Zicheng Liu, and Youzuo Lin. Unsupervised learning of full-waveform inversion: Connecting cnn and partial differential equation in a loop. *Preprint / Conference (ICLR)*, 2022.
- [28] Peng Jin, Yanan Feng, . . . , and Youzuo Lin. An empirical study of large-scale data-driven full waveform inversion. *Scientific Reports*, 14, 2024.
- [29] Justin Johnson, Alexandre Alahi, and Li Fei-Fei. Perceptual losses for real-time style transfer and super-resolution. *European Conference on Computer Vision (ECCV) Workshops*, 2016.
- [30] Yitzhak Katznelson. *An Introduction to Harmonic Analysis*. Cambridge University Press, 3rd edition, 2004.
- [31] Daniel Keysers and Walter Unger. Elastic image matching is np-complete. *Pattern Recognition Letters*, 24(1-3):445–453, 2003.
- [32] Florian Köhler. Exponax: Fourier spectral etdrk time-steppers in jax. Online, 2024. <https://fkoehler.site/exponax/>.
- [33] et al. Kong. Physics informed adversarial training for solving partial differential equations (piat). arXiv:2207.XXXX, 2022. physics-informed adversarial training (representative early work).
- [34] Jeong-Hoe Ku, JiHun Oh, YoungYoon Lee, et al. A selective survey on versatile knowledge distillation paradigm for neural network models. *arXiv preprint arXiv:2011.14554*, 2020.
- [35] I. Laga and W. Kleiber. The modified matérn process. *Applied Mathematics and Computation*, 2017. URL <https://amath.colorado.edu/faculty/kleiberw/papers/Laga2017.pdf>.
- [36] Hansheng Lei and Venu Govindaraju. Direct image matching by dynamic warping. In *Proceedings of the International Conference on Pattern Recognition (ICPR)*, 2003.
- [37] Yao Li, Shengzhu Shi, Zhichang Guo, and Boying Wu. Adversarial training for physics-informed neural networks. arXiv:2310.11789, 2023. arXiv preprint.
- [38] Yao Li, Shengzhu Shi, Zhichang Guo, and Boying Wu. Adversarial training for physics-informed neural networks (at-pinns), 2023. URL <https://arxiv.org/abs/2310.11789>. Preprint arXiv:2310.11789, <https://arxiv.org/abs/2310.11789>.

- [39] Zongyi Li, Nikola Kovachki, Kamyar Azizzadenesheli, Burigede Liu, Karthik Bhattacharya, Andrew Stuart, and Anima Anandkumar. Fourier neural operator for parametric partial differential equations. *arXiv preprint arXiv:2010.08895*, 2020. Preprint.
- [40] Zongyi Li, Nikola B. Kovachki, Kamyar Azizzadenesheli, Burigede Liu, Andrew Stuart, Kaushik Bhattacharya, and Anima Anandkumar. Fourier neural operator for parametric partial differential equations. *arXiv:2010.08895*, 2020.
- [41] Zongyi Li, Daniel Zhengyu Huang, Burigede Liu, and Anima Anandkumar. Fourier neural operator with learned deformations for pdes on general geometries. *Journal of Machine Learning Research*, 2023. Preprint / JMLR version.
- [42] et al. Liu. Adaptive movement sampling physics-informed residual network. *arXiv:2504.03244*, 2025. movement-based residual sampling and domain-coverage constraints.
- [43] Lu Lu, Pengzhan Jin, and George E. Karniadakis. Deeponet: Learning nonlinear operators for identifying differential equations based on the universal approximation theorem of operators. *arXiv:1910.03193*, 2019.
- [44] Lu Lu, Pengzhan Jin, and George Em Karniadakis. Deeponet: Learning nonlinear operators for identifying differential equations based on the universal approximation theorem of operators. *arXiv preprint arXiv:1910.03193*, 2019. URL <https://arxiv.org/abs/1910.03193>. Accessed: 2025-09-27.
- [45] Lu Lu, Pengzhan Jin, and George E. Karniadakis. Learning nonlinear operators via deeponet based on the universal approximation theorem of operators, 2021.
- [46] Lu Lu, Pengzhan Jin, and George Em Karniadakis. Learning nonlinear operators via deeponet based on the universal approximation theorem of operators, 2021. Preprint / *arXiv:2104.09481*.
- [47] Aleksander Madry, Aleksandar Makelov, Ludwig Schmidt, Dimitris Tsipras, and Adrian Vladu. Towards deep learning models resistant to adversarial attacks. *arXiv preprint arXiv:1706.06083*, 2017. URL <https://arxiv.org/abs/1706.06083>. Accessed: 2025-09-27.
- [48] Aleksander Madry, Aleksandar Makelov, Ludwig Schmidt, Dimitris Tsipras, and Adrian Vladu. Towards deep learning models resistant to adversarial attacks. In *International Conference on Learning Representations (ICLR)*, 2018. URL <https://openreview.net/pdf?id=rJzIBfZAb>.
- [49] Andrew J. Majda and Andrea L. Bertozzi. *Vorticity and Incompressible Flow*. Cambridge University Press, 2002.
- [50] Fabien Margairaz, Marco G. Giometto, Marc B. Parlange, and Marc Calaf. Comparison of dealiasing schemes in large-eddy simulation of neutrally stratified atmospheric flows. *Geoscientific Model Development*, 11:4069–4084, 2018. doi: 10.5194/gmd-11-4069-2018. URL <https://gmd.copernicus.org/articles/11/4069/2018/>.
- [51] Department of Mathematics / Course 18.06 MIT. Circulant matrices. Technical report, Massachusetts Institute of Technology, 2017. URL <https://web.mit.edu/18.06/www/Spring17/Circulant-Matrices.pdf>. Lecture notes, available at MIT OCW (PDF).
- [52] D. Molenaar. Forced navier–stokes flows on a bounded 2d domain: Abcn scheme overview. Technical report, 2004.
- [53] Mohammad Amin Nabian, Ryan J. Gladstone, and Hadi Meidani. Efficient training of physics-informed neural networks via importance sampling. *Computer-Aided Civil and Infrastructure Engineering*, 36(8): 962–977, 2021. doi: 10.1111/mice.12685.
- [54] Vit Niennattrakul and Chotirat Ann Ratanamahatana. Learning dtw global constraint for time series classification. In *Proceedings of the 2009 International Conference on Data Mining*, 2009.

- [55] Steven A. Orszag. Numerical methods for the simulation of turbulence. In *Fluid Dynamics*, 1972. Introduces the 2/3 dealiasing rule.
- [56] K. V. Park et al. Al-pinn: Active learning-driven physics-informed neural networks for efficient sample selection. arXiv:2502.03963, 2025.
- [57] Maziar Raissi, Paris Perdikaris, and George E. Karniadakis. Physics informed deep learning (part i): Data-driven solutions of nonlinear partial differential equations. *arXiv preprint arXiv:1711.10561*, 2017.
- [58] Maziar Raissi, Paris Perdikaris, and George E. Karniadakis. Physics-informed neural networks: A deep learning framework for solving forward and inverse problems involving nonlinear partial differential equations. *Journal of Computational Physics*, 378:686–707, 2019. doi: 10.1016/j.jcp.2018.10.045.
- [59] Carl Edward Rasmussen and Christopher K. I. Williams. *Gaussian Processes for Machine Learning*. MIT Press, 2006. URL <https://gaussianprocess.org/gpml/chapters/RW4.pdf>.
- [60] Carl Edward Rasmussen and Christopher K.I. Williams. *Gaussian Processes for Machine Learning*. MIT Press, 2006.
- [61] Adrian Romero, Nicolas Ballas, Samira E Kahou, Cesar Chassang, Carlo Gatta, and Yoshua Bengio. Fitnets: Hints for thin deep nets. In *ICLR*, 2015.
- [62] Walter Rudin. *Fourier Analysis on Groups*. Wiley, 1990.
- [63] Hiroaki Sakoe and Seibi Chiba. Dynamic programming algorithm optimization for spoken word recognition. *IEEE Transactions on Acoustics, Speech, and Signal Processing*, 26(1):43–49, 1978.
- [64] Pavel Senin. Dynamic time warping algorithm review. Technical Report, University of Hawai‘i at Mānoa, 2008. Available online.
- [65] Smarker. Discovering the fourier transform: A tutorial on circulant matrices, circular convolution, and the dft. GitHub gist, 2019. URL <https://gist.github.com/Smarker/1e6fb0ebfd43778b535cc049868589f3>. Online tutorial note.
- [66] Peter Sollich. Understanding gaussian process regression using the fourier transform, 2000. URL <https://homepages.inf.ed.ac.uk/ckiw/postscript/sheff3.pdf>. Lecture notes.
- [67] Mashbat Suzuki. Fourier-spectral methods for navier–stokes equations in 2d. Course notes/technical report, McGill University (MATH 595), 2014. URL <https://www.math.mcgill.ca/gantumur/math595f14/NSMashbat.pdf>. December 17, 2014.
- [68] Nils Thuerey, Philipp Holl, Maximilian Mueller, Patrick Schnell, Felix Trost, and Kiwon Um. Physics-based deep learning. arXiv preprint, 2021. URL <https://arxiv.org/abs/2109.05237>.
- [69] Lloyd N. Trefethen. *Spectral Methods in MATLAB*. SIAM, 2000.
- [70] Jakub Trynda. Physics-informed neural network with adaptive mesh refinement sampling. SSRN preprint 5148446, 2024.
- [71] Kiwon Um, Robert Brand, Yun (Raymond) Fei, Philipp Holl, and Nils Thuerey. Solver-in-the-loop: Learning from differentiable physics to interact with iterative pde-solvers. In *NeurIPS*, 2020. <https://proceedings.neurips.cc/paper/2020/file/43e4e6a6f341e00671e123714de019a8-Paper.pdf>.
- [72] Norbert Wiener. Generalized harmonic analysis. *Acta Mathematica*, 1930. Wiener–Khinchin link  $ACF \leftrightarrow PSD$ .
- [73] Andrew Gordon Wilson and Ryan P. Adams. Gaussian process kernels for pattern discovery and extrapolation, 2013. URL <https://arxiv.org/abs/1302.4245>.
- [74] Andrew Gordon Wilson and Ryan P. Adams. Gaussian process kernels for pattern discovery and extrapolation. In *Proceedings of the 30th International Conference on Machine Learning (ICML)*. PMLR, 2013. URL <https://proceedings.mlr.press/v28/wilson13.html>.

- [75] Andrew Gordon Wilson and Eric P. Xing. Advanced gaussian processes (lecture slides). CMU 10-708 Spring 2015, 2015. URL <https://www.cs.cmu.edu/~epxing/Class/10708-15/slides/andrewgp2.pdf>.
- [76] Andrew T.A. Wood and Grace Chan. Simulation of stationary gaussian vector fields. *Statistics and Computing*, 1994.
- [77] Chenxi Wu, Min Zhu, Qinyang Tan, Yadhu Kartha, and Lu Lu. A comprehensive study of non-adaptive and residual-based adaptive sampling for physics-informed neural networks. *Computer Methods in Applied Mechanics and Engineering*, 403:115671, 2023. doi: 10.1016/j.cma.2022.115671.
- [78] Chenxi Wu, Min Zhu, Qinyang Tan, Yadhu Kartha, and Lu Lu. A comprehensive study of non-adaptive and residual-based adaptive sampling for physics-informed neural networks. *Computer Methods in Applied Mechanics and Engineering*, 403:115671, 2023. doi: 10.1016/j.cma.2022.115671. URL <https://arxiv.org/abs/2207.10289>. Accessed: 2025-09-27.
- [79] Yue Xing, Qifan Song, and Guang Cheng. On the generalization properties of adversarial training. In *Proceedings of the 24th International Conference on Artificial Intelligence and Statistics (AISTATS)*, pages 505–513, 2021. URL <https://proceedings.mlr.press/v130/xing21b.html>.
- [80] Jeremy Yu, Lu Lu, Xuhui Meng, and George E. Karniadakis. Gradient-enhanced physics-informed neural networks for forward and inverse pde problems. *Computer Methods in Applied Mechanics and Engineering*, 393:114823, 2022. doi: 10.1016/j.cma.2022.114823.
- [81] Dongkun Zhang, Li Guo, and George E. Karniadakis. Quantifying total uncertainty in physics-informed neural networks for solving forward and inverse stochastic problems. *Journal of Computational Physics*, 397:108850, 2019. doi: 10.1016/j.jcp.2019.07.048.
- [82] Mengnan Zhao, Lihe Zhang, Jingwen Ye, Huchuan Lu, Baocai Yin, and Xinchao Wang. Adversarial training: A survey. *arXiv preprint arXiv:2410.15042*, 2024. URL <https://arxiv.org/abs/2410.15042>.
- [83] Kai Zhu et al. Improving generalization of adversarial training via robust critical fine-tuning. In *ICCV 2023*, 2023. URL [https://openaccess.thecvf.com/content/ICCV2023/papers/Zhu\\_Improving\\_Generalization\\_of\\_Adversarial\\_Training\\_via\\_Robust\\_Critical\\_Fine-Tuning\\_ICCV\\_2023\\_paper.pdf](https://openaccess.thecvf.com/content/ICCV2023/papers/Zhu_Improving_Generalization_of_Adversarial_Training_via_Robust_Critical_Fine-Tuning_ICCV_2023_paper.pdf).

# Appendix: Pseudospectral Methods and Spectral GRF Generation

## A 1D Burgers Equation via Pseudospectral Method

We consider the viscous Burgers equation on the periodic domain  $x \in [0, L]$ :

$$u_t + u u_x = \nu u_{xx}, \quad u(x, 0) = u_0(x), \quad u(x + L, t) = u(x, t).$$

We discretize using  $N$  equispaced points and represent

$$u(x, t) = \sum_{k=-N/2}^{N/2-1} \hat{u}_k(t) e^{i 2\pi k x / L}.$$

In Fourier space, the evolution is:

$$\partial_t \hat{u}_k = -\widehat{(u u_x)}_k - \nu \left( \frac{2\pi k}{L} \right)^2 \hat{u}_k.$$

Because direct convolution for the nonlinear term is costly, we use the *pseudospectral* (collocation) approach: evaluate nonlinear product in physical space, then FFT back to spectral space; and apply a de-aliasing mask (commonly the 2/3 rule). This is standard in spectral fluid solvers (see e.g. Orszag’s de-aliasing rules)

A widely used time-discretization is AB2 for the nonlinear part and Crank–Nicolson for the viscous term (“AB2/CN”):

$$\frac{\hat{u}_k^{n+1} - \hat{u}_k^n}{\Delta t} = -\left( \frac{3}{2} \hat{N}_k^n - \frac{1}{2} \hat{N}_k^{n-1} \right) - \nu \left( \frac{2\pi k}{L} \right)^2 \frac{\hat{u}_k^{n+1} + \hat{u}_k^n}{2},$$

where  $\hat{N}_k^n = \widehat{(u u_x)}_k^n$ . Solving for  $\hat{u}_k^{n+1}$ ,

$$\hat{u}_k^{n+1} = \frac{\hat{u}_k^n - \Delta t \left( \frac{3}{2} \hat{N}_k^n - \frac{1}{2} \hat{N}_k^{n-1} \right) - \frac{1}{2} \Delta t \nu (2\pi k / L)^2 \hat{u}_k^n}{1 + \frac{1}{2} \Delta t \nu (2\pi k / L)^2}.$$

### Pseudocode:

---

#### Algorithm 2 1D Burgers via AB2/CN (Fourier pseudospectral)

---

- 1: Given initial  $u^0(x_j)$ , compute  $\hat{u}_k^0 = \text{FFT}(u^0)$ ; set  $\hat{N}^{-1} = 0$
  - 2: **for**  $n = 0, 1, 2, \dots$  **do**
  - 3:    $u^n = \text{iFFT}(\hat{u}^n)$
  - 4:   Compute derivative in spectral:  $\widehat{u_x}^n = i 2\pi k / L \hat{u}_k^n$ , then  $u_x^n = \text{iFFT}(\widehat{u_x}^n)$
  - 5:   Compute nonlinear term:  $N^n = u^n \cdot u_x^n$  (pointwise multiplication)
  - 6:    $\hat{N}^n = \text{FFT}(N^n)$
  - 7:   Dealias: multiply by mask (e.g. zero out modes  $|k| > N/3$ )
  - 8:   Update  $\hat{u}_k^{n+1}$  via AB2/CN formula above
  - 9:   Shift  $\hat{N}^{n-1} \leftarrow \hat{N}^n$
  - 10: **end for**
- 

### Remarks:

- Choose  $N$  as a power of 2 for efficient FFT.
- The 2/3 de-aliasing rule is standard to avoid aliasing from quadratic nonlinearities (Orszag).
- In very high resolution or near-singular regimes, more advanced smoothing or spectral filtering may be used (e.g. high-order Fourier smoothing).
- The method is spectrally accurate for smooth solutions; for Burgers, shock formation limits smoothness and thus accuracy regimes.

## B Derivation: 3D $\rightarrow$ 2D Navier–Stokes, and Vorticity–Streamfunction Formulation

We begin with the full incompressible Navier–Stokes in three dimensions:

$$\mathbf{u}_t + (\mathbf{u} \cdot \nabla)\mathbf{u} = -\nabla p + \nu \Delta \mathbf{u} + \mathbf{f}, \quad \nabla \cdot \mathbf{u} = 0.$$

Define the vorticity vector

$$\boldsymbol{\omega} = \nabla \times \mathbf{u}.$$

Taking curl of the momentum equation yields the vorticity evolution:

$$\boldsymbol{\omega}_t + (\mathbf{u} \cdot \nabla)\boldsymbol{\omega} = (\boldsymbol{\omega} \cdot \nabla)\mathbf{u} + \nu \Delta \boldsymbol{\omega} + \nabla \times \mathbf{f}.$$

The term  $(\boldsymbol{\omega} \cdot \nabla)\mathbf{u}$  is called the vortex-stretching (or tilting) term.

Now restrict to *two-dimensional* flows in the  $(x, y)$ -plane: assume all fields are independent of  $z$ , and  $\mathbf{u} = (u, v, 0)$ . Then the vorticity has only the  $z$ -component:

$$\boldsymbol{\omega} = (0, 0, \omega), \quad \omega = \partial_x v - \partial_y u.$$

In 2D the vortex-stretching term vanishes:  $(\boldsymbol{\omega} \cdot \nabla)\mathbf{u} = 0$ . Thus the vorticity equation reduces to

$$\omega_t + u \partial_x \omega + v \partial_y \omega = \nu \Delta \omega + (\nabla \times \mathbf{f})_z.$$

To close the system, introduce the streamfunction  $\psi$  by

$$u = \partial_y \psi, \quad v = -\partial_x \psi,$$

so incompressibility is automatically satisfied, and

$$\omega = -\Delta \psi.$$

Hence one obtains the 2D forced vorticity–streamfunction system:

$$\boxed{\omega_t + \mathbf{u} \cdot \nabla \omega = \nu \Delta \omega + g, \quad -\Delta \psi = \omega, \quad \mathbf{u} = (\partial_y \psi, -\partial_x \psi),}$$

where  $g(\mathbf{x}, t) = (\nabla \times \mathbf{f})_z$ . This is the standard formulation for 2D spectral solvers of Navier–Stokes in vorticity form (see e.g. Suzuki’s Fourier-spectral exposition).

## C 2D Vorticity Equation: Pseudospectral Solver (Fourier, Periodic)

We solve on the periodic square  $\Omega = [0, L]^2$  using an  $N \times N$  uniform grid  $x_j = jL/N$ ,  $y_\ell = \ell L/N$ . Let integer wavenumbers  $(k_x, k_y) \in \{-\frac{N}{2}, \dots, \frac{N}{2} - 1\}^2$  and

$$k^2 = \left(2\pi \frac{k_x}{L}\right)^2 + \left(2\pi \frac{k_y}{L}\right)^2.$$

We discretize the forced vorticity–streamfunction system

$$\omega_t + u \omega_x + v \omega_y = \nu \Delta \omega + g(\mathbf{x}, t), \quad -\Delta \psi = \omega, \quad \mathbf{u} = (\psi_y, -\psi_x),$$

where  $g = (\nabla \times \mathbf{f})_z$  is the curl of the body force  $\mathbf{f}$ .

**Precomputation (once).**

1. Build wavenumber arrays  $k_x, k_y$  and  $k^2$ . For FFT libraries using real-to-complex transforms (e.g. RFFT), store the half-spectrum indexing accordingly (truncate the redundant half along the last dimension). Set  $k^2(0,0) \leftarrow 1$  for safe division, and later force  $\widehat{\psi}(0,0) = 0$ .
2. Construct the de-aliasing mask  $\mathcal{M}$  (e.g. 2/3 rule):  $\mathcal{M}(k_x, k_y) = 1$  if  $|k_x| \leq \frac{N}{3}$  and  $|k_y| \leq \frac{N}{3}$ , else 0.<sup>2</sup>
3. FFT the initial vorticity  $\widehat{\omega}^0 = \text{FFT}(\omega^0)$ . If the forcing  $g$  is time-independent, precompute  $\widehat{g} = \text{FFT}(g)$  once; if  $g = g(\cdot, t)$ , define  $\widehat{g}^n = \text{FFT}(g(\cdot, t_n))$  each step.

**Spectral relations (per step).**

$$\widehat{\psi} = -\frac{\widehat{\omega}}{k^2}, \quad \widehat{u} = i2\pi\frac{k_y}{L}\widehat{\psi}, \quad \widehat{v} = -i2\pi\frac{k_x}{L}\widehat{\psi}, \quad \widehat{\omega}_x = i2\pi\frac{k_x}{L}\widehat{\omega}, \quad \widehat{\omega}_y = i2\pi\frac{k_y}{L}\widehat{\omega}.$$

Transform  $u, v, \omega_x, \omega_y$  to physical space, form the nonlinear term

$$N(\mathbf{x}) = u\omega_x + v\omega_y,$$

then FFT back to get  $\widehat{N}$  and apply de-aliasing:  $\widehat{N} \leftarrow \mathcal{M} \odot \widehat{N}$ .

**Time stepping with forcing.** We present two popular semi-implicit updates that both treat the viscous term implicitly (Crank–Nicolson) and the quadratic advection explicitly.

**(A) CN + explicit Euler for advection/forcing (matches the provided code):**

$$\boxed{\frac{\widehat{\omega}^{n+1} - \widehat{\omega}^n}{\Delta t} = -\widehat{N}^n - \nu k^2 \frac{\widehat{\omega}^{n+1} + \widehat{\omega}^n}{2} + \widehat{g}^n}$$

which gives the explicit update

$$\boxed{\widehat{\omega}^{n+1} = \frac{(1 - \frac{1}{2}\Delta t \nu k^2)\widehat{\omega}^n - \Delta t \widehat{N}^n + \Delta t \widehat{g}^n}{1 + \frac{1}{2}\Delta t \nu k^2}}.$$

*Mapping to code:*  $\widehat{\omega} \leftrightarrow w_h, \widehat{N} \leftrightarrow F_h, \widehat{g} \leftrightarrow f_h, k^2 \leftrightarrow \text{lap}$  (with  $L = 1$ ).

**(B) AB2/CN (2nd-order advection, CN diffusion) [67, 69]:**

$$\boxed{\frac{\widehat{\omega}^{n+1} - \widehat{\omega}^n}{\Delta t} = -\left(\frac{3}{2}\widehat{N}^n - \frac{1}{2}\widehat{N}^{n-1}\right) - \nu k^2 \frac{\widehat{\omega}^{n+1} + \widehat{\omega}^n}{2} + \widehat{g}^{n+\frac{1}{2}}}$$

so that

$$\boxed{\widehat{\omega}^{n+1} = \frac{\widehat{\omega}^n - \Delta t\left(\frac{3}{2}\widehat{N}^n - \frac{1}{2}\widehat{N}^{n-1}\right) - \frac{1}{2}\Delta t \nu k^2 \widehat{\omega}^n + \Delta t \widehat{g}^{n+\frac{1}{2}}}{1 + \frac{1}{2}\Delta t \nu k^2}}.$$

Here one may take  $\widehat{g}^{n+\frac{1}{2}} \approx \frac{1}{2}(\widehat{g}^n + \widehat{g}^{n+1})$  if  $g$  varies in time, or simply  $\widehat{g}$  if  $g$  is steady.

<sup>2</sup>Other options include 3/2 padding or high-order spectral smoothing; see [25, 50].

---

**Algorithm 3** 2D NS in vorticity form, Fourier pseudospectral (periodic, with forcing)

---

- 1: **Precompute**  $k_x, k_y, k^2$ , mask  $\mathcal{M}$ ; set  $k^2(0, 0) \leftarrow 1$ , and enforce  $\widehat{\psi}(0, 0) = 0$  when used.
  - 2: **Init**  $\widehat{\omega}^0 = \text{FFT}(\omega^0)$ ; if  $g$  steady, set  $\widehat{g} = \text{FFT}(g)$  once.
  - 3: **for**  $n = 0, 1, 2, \dots$  **do**
  - 4:   *Poisson solve in Fourier:*  $\widehat{\psi} = -\widehat{\omega}^n/k^2$ ; then  $\widehat{u} = i 2\pi(k_y/L)\widehat{\psi}$ ,  $\widehat{v} = -i 2\pi(k_x/L)\widehat{\psi}$ .
  - 5:   *Derivatives:*  $\widehat{\omega}_x = i 2\pi(k_x/L)\widehat{\omega}^n$ ,  $\widehat{\omega}_y = i 2\pi(k_y/L)\widehat{\omega}^n$ .
  - 6:   *Back to real:*  $u, v, \omega_x, \omega_y \leftarrow \text{iFFT}(\cdot)$ .
  - 7:   *Nonlinear term:*  $N = u\omega_x + v\omega_y$ ; then  $\widehat{N}^n = \text{FFT}(N)$ ; apply de-alias:  $\widehat{N}^n \leftarrow \mathcal{M} \odot \widehat{N}^n$ .
  - 8:   *Forcing:* if  $g$  depends on  $t$ , set  $\widehat{g}^n = \text{FFT}(g(\cdot, t_n))$  (or midpoint  $\widehat{g}^{n+\frac{1}{2}}$ ).
  - 9:   *Update*  $\widehat{\omega}^{n+1}$  using either scheme (A) or (B) above, with  $\nu k^2$  implicit.
  - 10:   *(Optional) Diagnostics/recording:*  $\omega^{n+1} = \text{iFFT}(\widehat{\omega}^{n+1})$ ; record enstrophy  $\|\omega\|_2^2$ , energy via  $\psi$ ; store snapshots every  $m$  steps.
  - 11: **end for**
- 

**Full algorithm (with forcing).**

**Implementation notes.**

- **Forcing in practice.** If the original body force is  $\mathbf{f} = (f_x, f_y)$ , then  $g = (\nabla \times \mathbf{f})_z = \partial_x f_y - \partial_y f_x$ . One may specify  $g$  directly in vorticity form and FFT once (as in the example), or specify  $\mathbf{f}$  and curl it in spectral space.
- **Zero mode.** Set  $\widehat{\psi}(0, 0) = 0$  (adding a constant to  $\psi$  does not change  $\mathbf{u}$ ). Keeping  $k^2(0, 0) = 1$  avoids division-by-zero; the corresponding  $\widehat{\omega}(0, 0)$  is preserved by incompressible advection and diffusion.
- **De-aliasing.** For quadratic nonlinearities, use the 2/3 truncation mask or the 3/2 zero-padding method; both are standard and control aliasing errors in pseudo-spectral products.<sup>3</sup>
- **Time step (CFL) guidance.** Choose  $\Delta t$  to satisfy an advective CFL (e.g.  $\Delta t \lesssim c \frac{L}{N \max |u|}$ ) and viscous stability constraint  $\Delta t \lesssim c_\nu / (\nu k_{\max}^2)$ , where  $k_{\max} \sim 2\pi \frac{N/2}{L}$ .<sup>4</sup>

## D Spectral Synthesis of Gaussian Random Fields (GRFs)

I and past literature extensively used GRF as initial condition of PDE system, both for 1D and 2D test cases. This section talks about the theory and implementation of generating GRF samples using spectral methods from 1 GRF distribution.

To generate a zero-mean stationary Gaussian random field (GRF) with specified autocovariance (or auto-correlation function, ACF) under periodic boundary conditions, the spectral method (via Wiener–Khinchin theorem and circulant embedding) is widely used.

**Theory.** By Wiener–Khinchin, the ACF  $k(\tau)$  and the power spectral density (PSD)  $S(\omega)$  are Fourier duals. Bochner’s theorem ensures that a positive-definite stationary kernel corresponds to nonnegative spectral measure  $S \geq 0$ . Under periodic boundary conditions on a discrete grid, the covariance matrix becomes circulant, which is diagonalized by the discrete Fourier transform:

$$C = F^{-1} \text{diag}(S) F.$$

Thus if we sample white Gaussian noise in frequency domain and weight by  $\sqrt{S}$ , we get the correct covariance structure after inverse FFT (this is the circulant embedding / spectral synthesis method).

---

<sup>3</sup>See Hou and Li [25] for a comparison with high-order spectral filters; see also Margairaz et al. [50] on 3/2-rule padding.

<sup>4</sup>Exact constants depend on the scheme; AB2/CN is more accurate for advection than explicit Euler.

---

**Algorithm 4** Spectral GRF Generation (periodic domain)

---

- 1: Build frequency grid  $\omega$  (1D/2D/3D) and compute  $S(\omega) \geq 0$  (e.g. from Matérn or Gaussian kernel)
  - 2: Sample complex white noise  $\xi(\omega)$  with Hermitian symmetry (so that resulting field is real)
  - 3: Set  $\hat{f}(\omega) = \sqrt{S(\omega)} \xi(\omega)$
  - 4: Compute  $f = \text{iFFT}(\hat{f})$ ; take real part
- 

**Algorithm.** In practice, we can enforce Hermitian symmetry, the field in real space is real and has the target covariance.

**Kernel choices and spectral form.** For example, a Matérn kernel in  $\mathbb{R}^d$  has the spectral decay

$$S(\omega) \propto (1 + \ell^2 \|\omega\|^2)^{-(\nu+d/2)},$$

so one can compute  $\sqrt{S(\omega)}$  in closed form (up to normalization) and sample accordingly.

Besides the Matérn family (whose spectrum decays like  $(1 + \ell^2 \|\omega\|^2)^{-(\nu+d/2)}$ ), several widely used stationary kernels admit simple spectral descriptions. Below we list common kernels, their key parameters, and their (continuous) power spectral densities  $S(\omega)$  in  $\mathbb{R}^d$  (up to normalization constants; conventions may differ by factors of  $2\pi$ ).

- **RBF / Gaussian / Squared-Exponential (SE).**

$$k_{\text{RBF}}(r) = \sigma^2 \exp\left(-\frac{r^2}{2\ell^2}\right), \quad S_{\text{RBF}}(\omega) \propto (2\pi\ell^2)^{d/2} \exp\left(-\frac{\ell^2 \|\omega\|^2}{2}\right).$$

*Parameters:* variance  $\sigma^2$ , length scale  $\ell$ . *Notes:* “RBF kernel” and “Gaussian kernel” are used interchangeably in the GP literature; both refer to the SE form above. Its spectrum is Gaussian in frequency, implying very smooth (infinitely mean-square differentiable) sample paths. [75, 66, 59]

- **Matérn.**

$$k_{\text{Matérn}}(r) = \sigma^2 \frac{2^{1-\nu}}{\Gamma(\nu)} \left(\sqrt{2\nu} \frac{r}{\ell}\right)^\nu K_\nu\left(\sqrt{2\nu} \frac{r}{\ell}\right), \quad S_{\text{Matérn}}(\omega) \propto (2\nu/\ell^2 + \|\omega\|^2)^{-(\nu+d/2)}.$$

*Parameters:* variance  $\sigma^2$ , length scale  $\ell$ , smoothness  $\nu > 0$ . *Notes:* Controls roughness via  $\nu$ ; as  $\nu \rightarrow \infty$ , RBF is recovered. [2, 35, 59]

- **Rational Quadratic (RQ).**

$$k_{\text{RQ}}(r) = \sigma^2 \left(1 + \frac{r^2}{2\alpha\ell^2}\right)^{-\alpha},$$

*Parameters:* variance  $\sigma^2$ , length scale  $\ell$ , shape  $\alpha > 0$ . *Spectrum:* can be viewed as a *scale mixture* of Gaussians in either domain; equivalently,  $k_{\text{RQ}}$  is an infinite mixture of RBF kernels with an inverse-Gamma prior on the length scale, which yields a Student- $t$ -like heavy-tailed  $S(\omega)$  (relative to RBF). [16, 13]

- **Periodic (strictly periodic) kernel.**

$$k_{\text{per}}(\tau) = \sigma^2 \exp\left(-\frac{2 \sin^2(\pi\tau/p)}{\ell^2}\right).$$

*Parameters:* variance  $\sigma^2$ , fundamental period  $p$ , length scale  $\ell$  (controls harmonic envelope). *Spectrum:* *discrete* lines at integer multiples of the base frequency  $2\pi/p$  (a Dirac comb), with amplitudes modulated by a Gaussian envelope determined by  $\ell$ ; i.e., strictly periodic covariance  $\Rightarrow$  discrete harmonic spectrum. [14, 1, 23]

- **Spectral Mixture (SM).** A flexible stationary kernel obtained by modelling the spectral density directly as a Gaussian mixture:

$$S_{\text{SM}}(\omega) = \sum_{q=1}^Q w_q \mathcal{N}(\omega; \mu_q, \Sigma_q), \quad k_{\text{SM}}(\tau) = \sum_{q=1}^Q w_q \exp\left(-\frac{1}{2}\tau^\top \Sigma_q \tau\right) \cos(\mu_q^\top \tau),$$

where  $w_q > 0$  are weights,  $\mu_q$  are mean frequencies (capturing periodicities), and  $\Sigma_q$  control length scales (decay). *Parameters:*  $\{w_q, \mu_q, \Sigma_q\}_{q=1}^Q$ . *Notes:* Can approximate many stationary kernels by matching their spectra; useful for pattern discovery and extrapolation. [74, 73, 23]

*Relations and guidance.* RBF(Gaussian)  $\equiv$  SE; Matérn  $\rightarrow$  RBF as  $\nu \rightarrow \infty$ ; RQ is a scale-mixture of RBFs (heavier spectral tails than RBF); strictly periodic kernels have *discrete* spectra (harmonics), unlike the continuous spectra of RBF/Matérn/RQ; SM parameterizes  $S(\omega)$  directly and thus subsumes many stationary covariances. Practical PSD normalizations depend on Fourier conventions; here we emphasize shapes/decay rather than constants. [59, 75, 13]

**Theoretical underpinning.** On a periodic domain (torus) or a discrete periodic grid, a stationary covariance kernel  $k(x - y)$  defines a linear, translation-invariant (convolution) operator

$$(Tf)(x) = \int_{\Omega} k(x - y) f(y) dy,$$

or its discrete analogue. Translation invariance implies that  $T$  commutes with all translations; the common eigenfunctions of translation are the Fourier exponentials  $e^{i\omega \cdot x}$ . Hence, *Fourier transforms diagonalize all convolution (translation-invariant) operators:* each Fourier mode is an eigenfunction with eigenvalue equal to the Fourier transform of the kernel. In finite-dimensional, discrete, periodic settings the covariance matrix  $C$  is *circulant* (block-circulant in multiple dimensions) and is diagonalized by the DFT matrix  $F$ :

$$C = F^{-1} \text{diag}(S(\omega)) F,$$

where  $S(\omega)$  is the (discrete) power spectrum. This is precisely the spectral-theorem analogue of an eigen-decomposition  $C = Q\Lambda Q^*$  with Fourier basis playing the role of  $Q$  and  $S(\omega)$  giving the eigenvalues [21, 69].

**Wiener–Khinchin.** For a (wide-sense) stationary process/field with autocovariance  $r(\tau) = \mathbb{E}[X(t)X(t+\tau)]$  (assuming zero mean), the *Wiener–Khinchin theorem* states that  $r$  and the power spectral density (PSD)  $S$  are Fourier transform pairs:

$$S(\omega) = \int_{\mathbb{R}^d} r(\tau) e^{-i\omega \cdot \tau} d\tau, \quad r(\tau) = \frac{1}{(2\pi)^d} \int_{\mathbb{R}^d} S(\omega) e^{i\omega \cdot \tau} d\omega.$$

On a discrete periodic grid, the same relation holds with DFTs. Thus specifying  $r$  (the covariance kernel) uniquely specifies  $S$ , and vice versa; in particular, sampling in the frequency domain with variance  $S(\omega)$  yields a field with covariance  $r$  [72, 60].

**Bochner.** *Bochner’s theorem* characterizes exactly which stationary kernels are valid covariances: a continuous function  $k : \mathbb{R}^d \rightarrow \mathbb{C}$  is positive-definite (so that all finite covariance matrices built from it are positive semidefinite) if and only if it is the Fourier transform of a finite nonnegative measure on frequency space. In the absolutely continuous case,

$$k(\tau) = \int_{\mathbb{R}^d} e^{i\omega \cdot \tau} S(\omega) d\omega, \quad \text{with } S(\omega) \geq 0 \text{ (the spectral density).}$$

Therefore, choosing any nonnegative  $S(\omega)$  automatically defines a valid stationary covariance kernel  $k$ , and conversely any stationary covariance admits a nonnegative spectrum [62, 30].

**Implication for spectral GRF sampling.** Combining the above: (i) by Wiener–Khinchin,  $S = \mathcal{F}\{k\}$ ; (ii) by Bochner,  $S(\omega) \geq 0$  iff  $k$  is a valid covariance; (iii) on periodic grids,  $C$  is circulant and diagonalized by  $F$ . Hence, drawing independent complex Gaussian modes  $\xi(\omega)$  with Hermitian symmetry and setting

$$\hat{f}(\omega) = \sqrt{S(\omega)} \xi(\omega), \quad f = \text{iFFT } \hat{f},$$

gives a real GRF with

$$\mathbb{E}[ff^*] = F^{-1}\text{diag}(S)F = C,$$

i.e. exactly the target covariance. This is the operator-theoretic analogue of finite-dimensional Gaussian sampling  $Q\Lambda^{1/2}z$  with  $z \sim \mathcal{N}(0, I)$ , where  $Q$  is the Fourier basis and  $\Lambda = \text{diag}(S)$  [21, 69, 60].

**Emphasis on operator diagonalization, circulant matrices, and Fourier diagonalization.** In the preceding discussion we asserted that translation-invariant (convolution) operators and circulant covariance matrices are diagonalized by the Fourier transform. We now elaborate more on the precise connections among these concepts:

- **Convolution operator and translation invariance.** A stationary covariance kernel  $k(x - y)$  on a periodic domain defines a convolution operator

$$(Tf)(x) = \int_{\Omega} k(x - y) f(y) dy,$$

or discretely  $(Tf)_j = \sum_m k_{j-m} f_m$ . Because  $k$  depends only on relative displacement,  $T$  commutes with translation (i.e. shifting the argument). In functional-analytic terms,  $T$  is a *circulant operator* in the periodic setting, and the group of translations is its symmetry group.

- **Eigenfunctions are Fourier modes.** Since the operator  $T$  commutes with every translation, it shares eigenfunctions with translation operators. The eigenfunctions of translation (on a periodic domain) are the Fourier exponentials  $e^{i\omega \cdot x}$ . Thus each Fourier mode is an eigenfunction of  $T$ , with eigenvalue given by the Fourier transform  $\hat{k}(\omega)$  (i.e. the spectral density). This is the continuous (or discretized) operator version of diagonalization.
- **From Toeplitz to circulant to DFT diagonalization.** In finite discrete settings (on a 1D or multidimensional periodic grid), the covariance matrix  $C$  built from a stationary kernel is *Toeplitz* when ignoring boundary wrapping, and becomes *circulant* under periodic embedding (i.e. every row is a cyclic shift of the previous row) [21]. A circulant matrix  $C$  has the property that it can be written as

$$C = F^{-1} \Lambda F,$$

where  $F$  is the discrete Fourier transform (DFT) matrix and  $\Lambda = \text{diag}(\lambda_k)$  is diagonal. Equivalently, conjugating by the Fourier basis diagonalizes  $C$  [21, 51].

Intuitively, the convolution interpretation of multiplication by  $C$  (i.e.  $Cf$  is a discrete convolution) becomes pointwise multiplication in Fourier space, which is precisely the effect of diagonalization by DFT. In other words,

$$Cf = (\text{convolution}) \implies FCF^{-1} = \text{diag}(S(\omega)).$$

Because *all* circulant matrices commute (they form a commutative algebra), they are simultaneously diagonalizable by the same eigenbasis (the DFT basis) [65, 19].

- **Convolution theorem  $\leftrightarrow$  DFT diagonalization.** For functions  $f, g$  on  $\mathbb{R}$ , define the convolution

$$(f * g)(x) = \int_{-\infty}^{+\infty} f(\tau) g(x - \tau) d\tau,$$

and the Fourier transform  $\hat{f}(\omega) := \mathcal{F}\{f\}(\omega)$  (likewise  $\hat{g}$ ). The *convolution theorem* states

$$\mathcal{F}\{f * g\}(\omega) = \mathcal{F}\{f\}(\omega) \cdot \mathcal{F}\{g\}(\omega) = \hat{f}(\omega) \hat{g}(\omega),$$

$$\{f * g\}(\omega) = \mathcal{F}^{-1}\{\mathcal{F}\{f\}(\omega) \cdot \mathcal{F}\{g\}(\omega)\}$$

$$f * g = \mathcal{F}^{-1}\{\mathcal{F}\{f\} \cdot \mathcal{F}\{g\}\}$$

i.e., the time-domain integral operator (convolution by  $g$ ) becomes pointwise multiplication in frequency.

On a periodic grid (length  $N$ ), let  $F$  be the DFT matrix and  $\hat{f} := Ff$ . For a circulant  $C$  with first column  $c$ , we have

$$Cf = c \star f, \quad C = F^{-1}\Lambda F, \quad \Lambda = \text{diag}(Fc),$$

hence

$$\begin{aligned} c \star f &= Cf = F^{-1}(\Lambda \hat{f}) = F^{-1}((Fc) \odot (Ff)), \\ c \star f &= F^{-1}((Fc) \odot (Ff)), \end{aligned}$$

which is exactly the discrete counterpart of the convolution theorem: circular convolution in time equals elementwise multiplication in frequency (circulant matrices are diagonal in the DFT basis).

*Remark (FNO).* Fourier Neural Operator (FNO) leverages this principle by learning/parametrizing the kernel in the frequency domain (the  $R$  tensor in FNO is equivalent to  $Fc$ ,  $\mathcal{F}\{f\}$  stated above) and applying elementwise multiplication on Fourier coefficients (in FNO it is the elementwise linear transformation on Fourier coefficients vectors of some channels), then inverse-transforming back—computationally efficient via FFT and equivalent to a global (periodic) convolution in the spatial domain.

- **Combining with Bochner and Wiener–Khinchin.** Putting these pieces together:

1. Wiener–Khinchin gives the equivalence between autocovariance  $k(\tau)$  and spectrum  $S(\omega) = \widehat{k}(\omega)$ .
2. Bochner guarantees that  $k(\tau)$  is a valid (positive-definite) covariance kernel exactly when  $S(\omega) \geq 0$ .
3. On a periodic discrete grid,  $C$  (as a circulant matrix) is diagonalizable by the Fourier transform with eigenvalues  $S(\omega)$ .
4. Therefore sampling independent Fourier modes with variance  $S(\omega)$  and transforming back gives a real field with exactly covariance matrix  $C$ .

- **Analogy with finite-dimensional Gaussian sampling.** In finite-dimensional statistics, sampling a Gaussian vector with covariance  $C = Q\Lambda Q^T$  is done via  $Q\Lambda^{1/2}z$ . Here,  $Q$  is the eigenvector matrix and  $\Lambda$  the eigenvalue diagonal. In our spectral GRF context, the Fourier basis plays the role of  $Q$ ,  $\Lambda = \text{diag}(S(\omega))$ , and  $z$  corresponds to independent complex Gaussian Fourier modes. Thus the spectral method is the functional-analytic extension of the standard multivariate Gaussian sampling procedure, adapted to translation-invariant operators.

In summary, the chain of ideas is:

$$\begin{aligned} \underbrace{k(x-y)}_{\text{stationary kernel}} &\longrightarrow \underbrace{\text{convolution operator } T}_{\text{commutes with translations}} \longrightarrow \underbrace{\text{Fourier eigenbasis}}_{\text{diagonalizes } T} \longrightarrow \underbrace{C}_{\text{circulant covariance matrix}} \\ &\longrightarrow C = F^{-1}\text{diag}(S)F \longrightarrow \text{spectral sampling via } \sqrt{S(\omega)}. \end{aligned}$$

## Appendix: Variational Functionals, Fréchet Derivatives, and Correspondences

Let  $X, Y$  be Banach spaces (e.g. spaces of functions). A functional is a map

$$J : X \rightarrow \mathbb{R},$$

and a nonlinear functional means  $J$  is not necessarily linear.

We say  $J$  is Fréchet differentiable at  $x \in X$  if there exists a bounded linear functional

$$DJ(x) : X \rightarrow \mathbb{R}$$

such that

$$J(x+h) = J(x) + DJ(x)[h] + o(\|h\|), \quad \|h\| \rightarrow 0.$$

Similarly, for a nonlinear operator

$$G : X \rightarrow Y,$$

if  $G$  is Fréchet differentiable at  $x$ , there exists a bounded linear operator

$$DG(x) : X \rightarrow Y$$

such that

$$G(x+h) = G(x) + DG(x)[h] + o(\|h\|).$$

—

Correspondences to finite-dimensional / discrete settings

- In finite dimensions  $f : \mathbb{R}^n \rightarrow \mathbb{R}^m$ , the Fréchet derivative is the Jacobian matrix  $Df(x)$  so that  $f(x+h) = f(x) + Df(x)h + o(\|h\|)$ .

- In the operator / functional setting:

- For  $J : X \rightarrow \mathbb{R}$ ,  $DJ(x)$  is a linear functional (analogue of the gradient).

- For  $G : X \rightarrow Y$ ,  $DG(x)$  is a linear operator (analogue of the Jacobian).

- Under discretization (mesh, grid, finite basis),  $X, Y$  become finite-dimensional vector spaces and  $DJ, DG$  become ordinary gradients or Jacobian matrices acting on vectors / tensors.

# Appendix: Dynamic Time Warping (DTW) and Soft-DTW

## Classical DTW

Dynamic Time Warping (DTW) is a method for measuring similarity between two temporal sequences  $\mathbf{x} = (x_1, x_2, \dots, x_n)$  and  $\mathbf{y} = (y_1, y_2, \dots, y_m)$ , allowing nonlinear time alignment. DTW computes an alignment path  $\pi = \{(i_k, j_k)\}_{k=1}^K$  that minimizes the cumulative distance:

$$\text{DTW}(\mathbf{x}, \mathbf{y}) = \min_{\pi} \sum_{(i,j) \in \pi} d(x_i, y_j), \quad (1)$$

where  $d(\cdot, \cdot)$  is typically the squared Euclidean distance.

The DTW cost is computed via dynamic programming:

$$D(i, j) = d(x_i, y_j) + \min\{D(i-1, j), D(i, j-1), D(i-1, j-1)\}, \quad (2)$$

with boundary conditions  $D(0, 0) = 0$  and  $D(i, 0) = D(0, j) = +\infty$ . The final DTW cost is  $D(n, m)$ .

**Complexity.** DTW requires filling an  $n \times m$  dynamic programming table, hence:

$$\text{Time complexity: } \mathcal{O}(nm), \quad \text{Memory complexity: } \mathcal{O}(nm).$$

**Differentiability.** DTW is **not differentiable** because of the hard min operator. Only one alignment path contributes to the final cost, creating piecewise-constant gradients and zero-gradient regions, which prevents backpropagation in neural networks.

## Soft-DTW

Soft-DTW [9] replaces the nondifferentiable minimum in DTW with a smooth soft-min operator:

$$\text{softmin}_{\gamma}(a_1, \dots, a_k) = -\gamma \log\left(\sum_{i=1}^k e^{-a_i/\gamma}\right), \quad (3)$$

where  $\gamma > 0$  is a smoothness parameter. The Soft-DTW cost is:

$$\text{SoftDTW}_{\gamma}(\mathbf{x}, \mathbf{y}) = \text{softmin}_{\pi} \sum_{(i,j) \in \pi} d(x_i, y_j). \quad (4)$$

The corresponding dynamic programming recursion becomes:

$$D_{\gamma}(i, j) = d(x_i, y_j) + \text{softmin}_{\gamma}(D_{\gamma}(i-1, j), D_{\gamma}(i, j-1), D_{\gamma}(i-1, j-1)). \quad (5)$$

**Complexity.** Soft-DTW retains the same asymptotic cost as DTW:

$$\text{Time complexity: } \mathcal{O}(nm), \quad \text{Memory complexity: } \mathcal{O}(nm).$$

**Differentiability.** Soft-DTW is **fully differentiable** because: 1. the soft-min is a smooth approximation of min, 2. gradients are spread across *all* alignment paths (not only one), 3. the backward pass is computed via a second DP recursion, enabling end-to-end training.

As  $\gamma \rightarrow 0^+$ , Soft-DTW converges to classical DTW, but as  $\gamma$  increases, the loss becomes smoother and gradients more stable for optimization.

# Appendix: FNO OOD Testing Performance

## D.1 FNO on 1D Burgers

Dataset: range=(0,1) | Pattern: gaussian | Params: cl=0.1

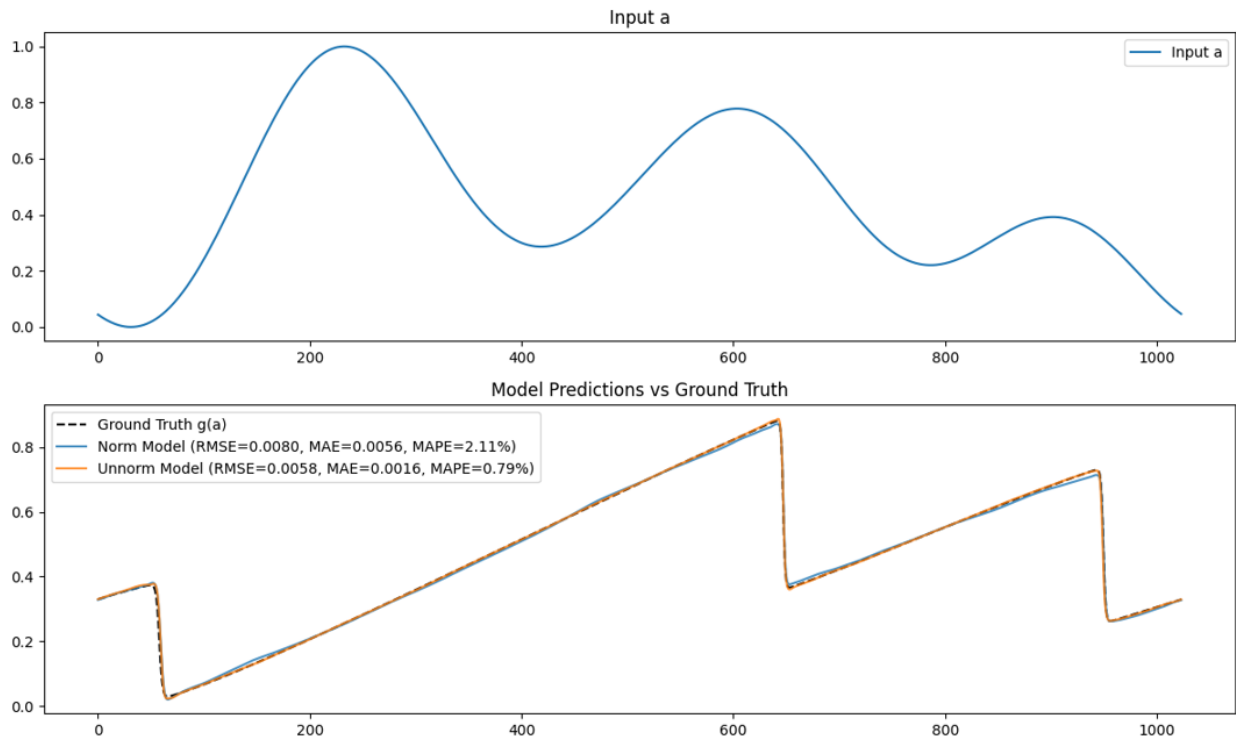


Figure 8: Normalized and Unnormalized FNO 1D Burgers Testing Sample 1 (in-distribution/train and test distribution)

Dataset: range=(-1,0) | Pattern: gaussian | Params: cl=0.1

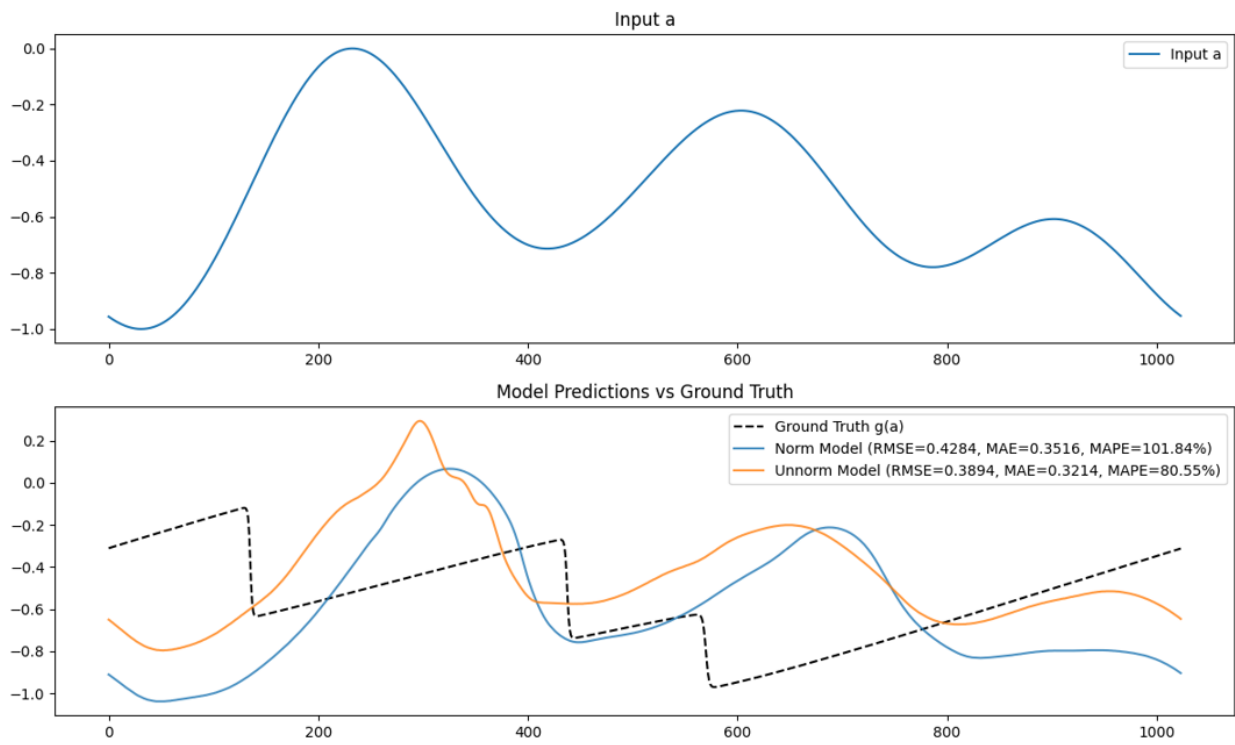


Figure 9: Normalized and Unnormalized FNO 1D Burgers OOD Testing Sample 10

Dataset: range=(0,2) | Pattern: gaussian | Params: cl=0.01

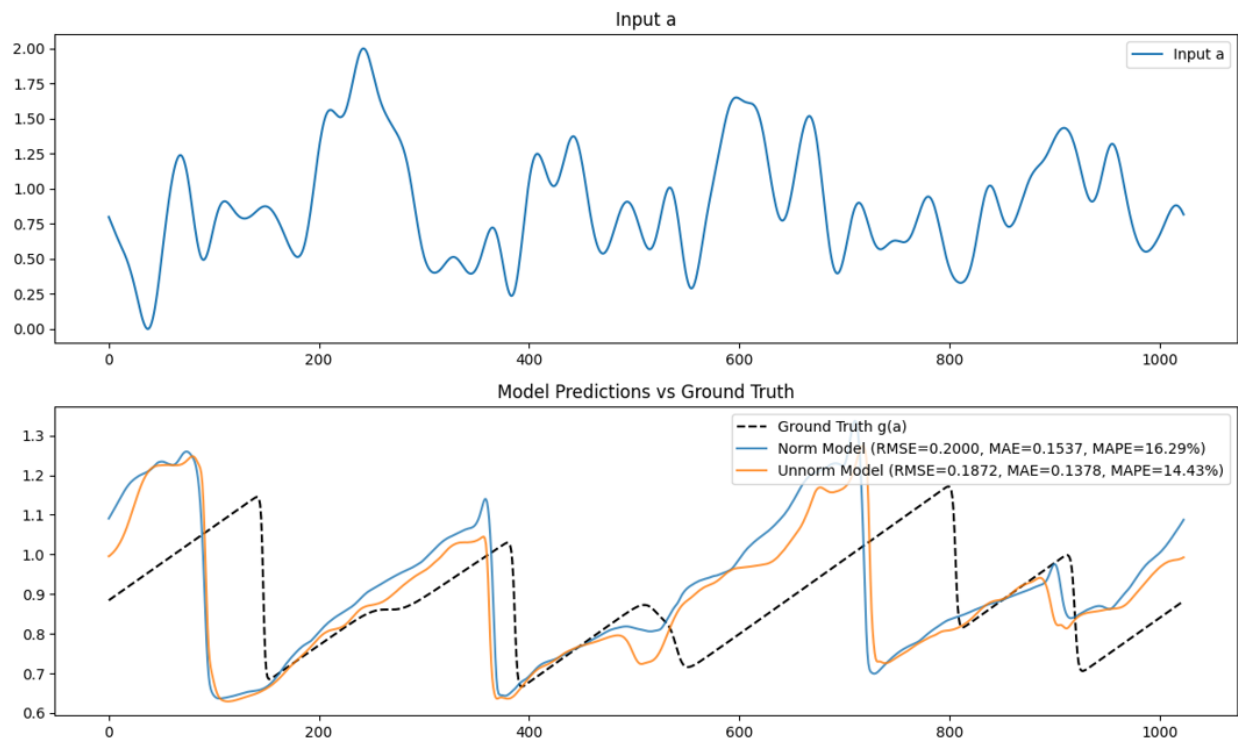


Figure 10: Normalized and Unnormalized FNO 1D Burgers OOD Testing Sample 11

Dataset: range=(-1,0) | Pattern: matern | Params: cl=0.03, nu=2.5

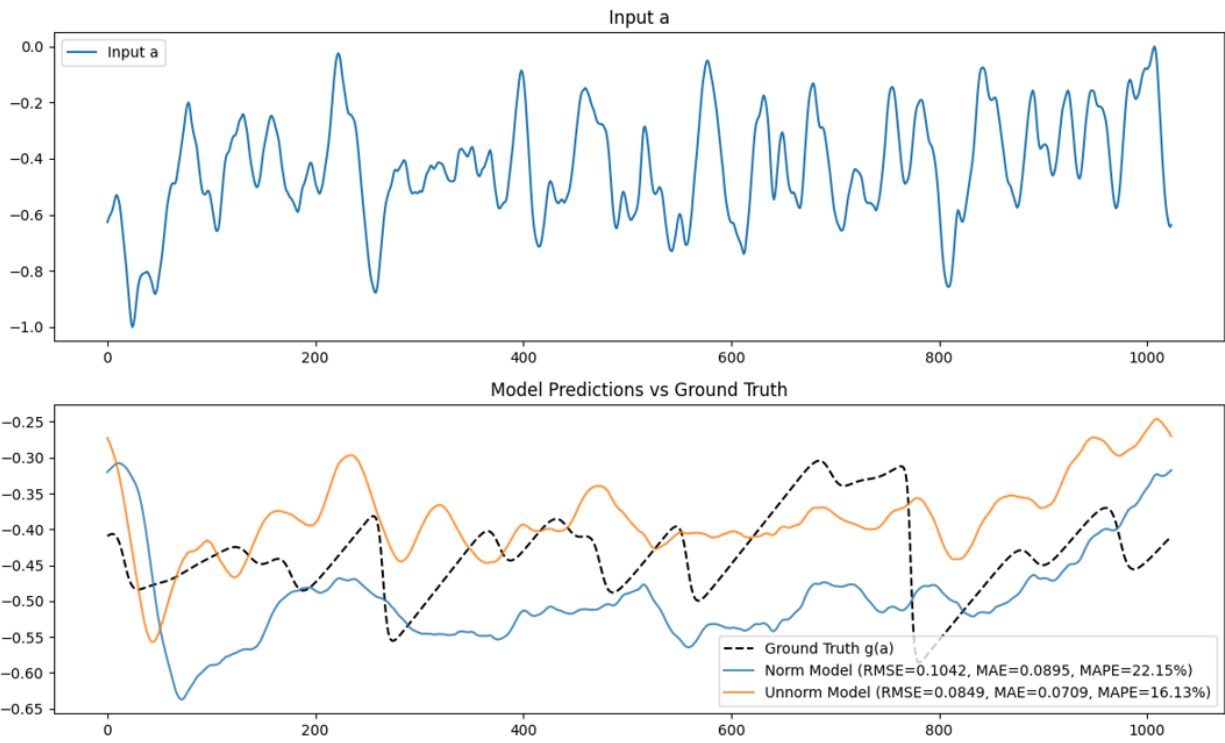


Figure 11: Normalized and Unnormalized FNO 1D Burgers OOD Testing Sample 13

# Recurrent FNO2d on 2D NS

Dataset: dim2d\_nx256\_N1150\_solver=exponax\_nu0.000\_t20.0\_train\_all\_frames | Index: 0 | RMSE=0.1414 MAE=0.1092 MAPE=29.93%  
solver=exponax | nx=256 | N=1150 | nu=0.000 | t=20.0

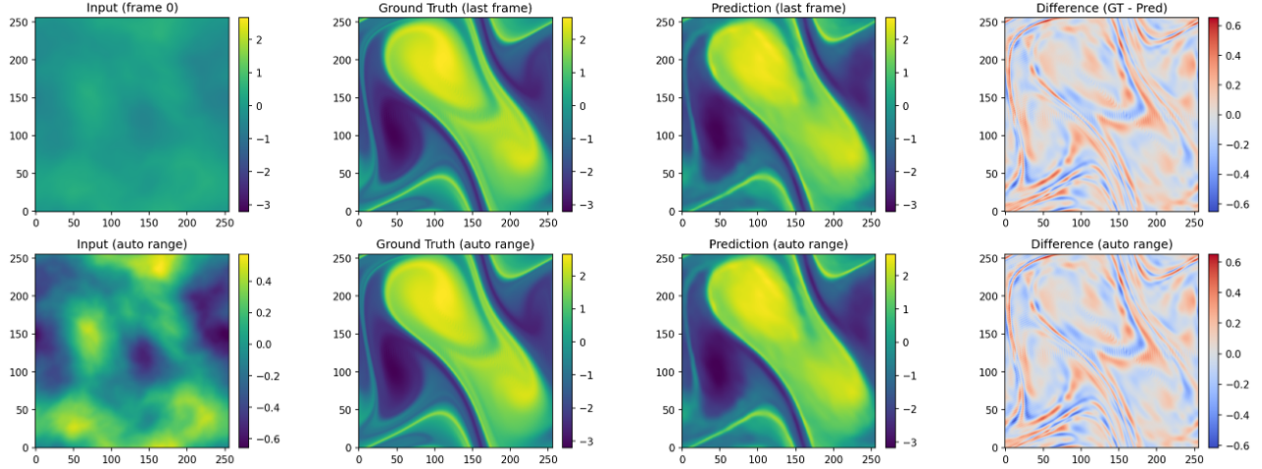


Figure 12: Unnormalized FNO 2D NS Testing Sample (in-distribution/train)

Dataset: dim2d\_nx256\_N50\_solver=exponax\_nu0.000\_t20.0\_test\_all\_frames | Index: 0 | RMSE=0.2101 MAE=0.1417 MAPE=48.69%  
solver=exponax | nx=256 | N=50 | nu=0.000 | t=20.0

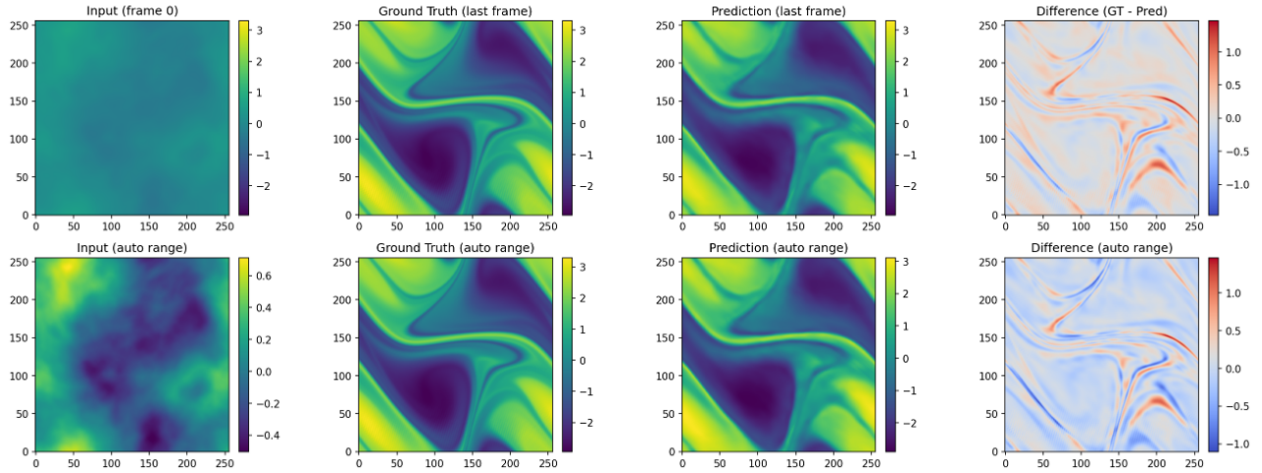


Figure 13: Unnormalized FNO 2D NS Testing Sample (in-distribution/test)

Dataset: dim2d\_nx256\_N10\_solver=exponax\_nu0.000\_t20.0\_test\_ntimepoints21\_GRF\_periodic\_length\_scale40\_period0.050\_vmax1\_vmin-1\_batch0\_all\_frames | Index: 0 | RMSE=0.0679 MAE=0.0514 MAPE=7.95%  
 type=GRF\_periodic | solver=exponax | nx=256 | N=10 | nu=0.000 | t=20.0 | ntimepoints=21 | length\_scale=40 | period=0.050 | vmax=1 | vmin=-1

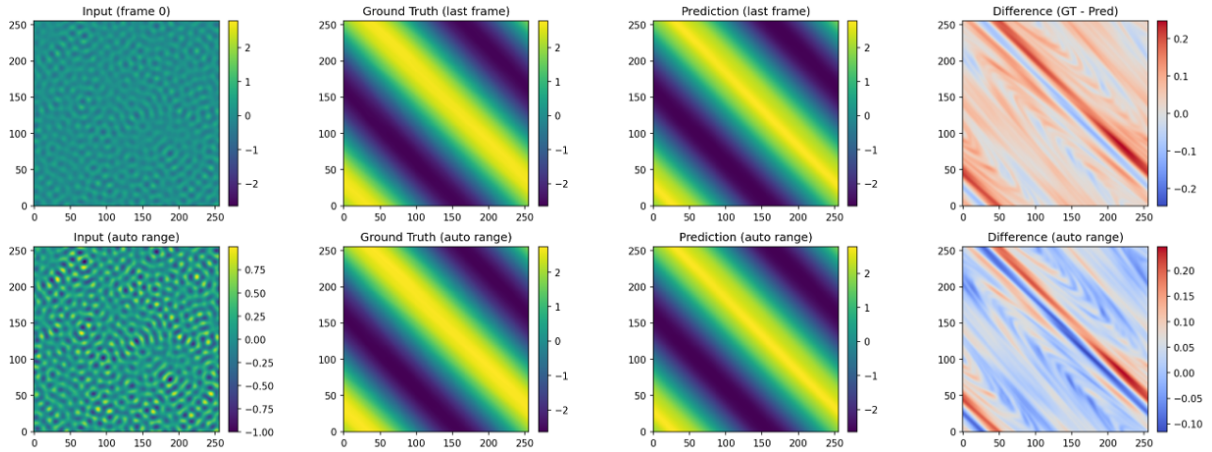


Figure 14: Unnormalized FNO 2D NS OOD Testing Sample 1

Dataset: dim2d\_nx256\_N10\_solver=exponax\_nu0.000\_t20.0\_test\_ntimepoints21\_GRF\_periodic\_length\_scale40\_period0.100\_vmax1.5\_vmin-1\_batch0\_all\_frames | Index: 0 | RMSE=1.3266 MAE=1.2365 MAPE=529.99%  
 type=GRF\_periodic | solver=exponax | nx=256 | N=10 | nu=0.000 | t=20.0 | ntimepoints=21 | length\_scale=40 | period=0.100 | vmax=1.5 | vmin=-1

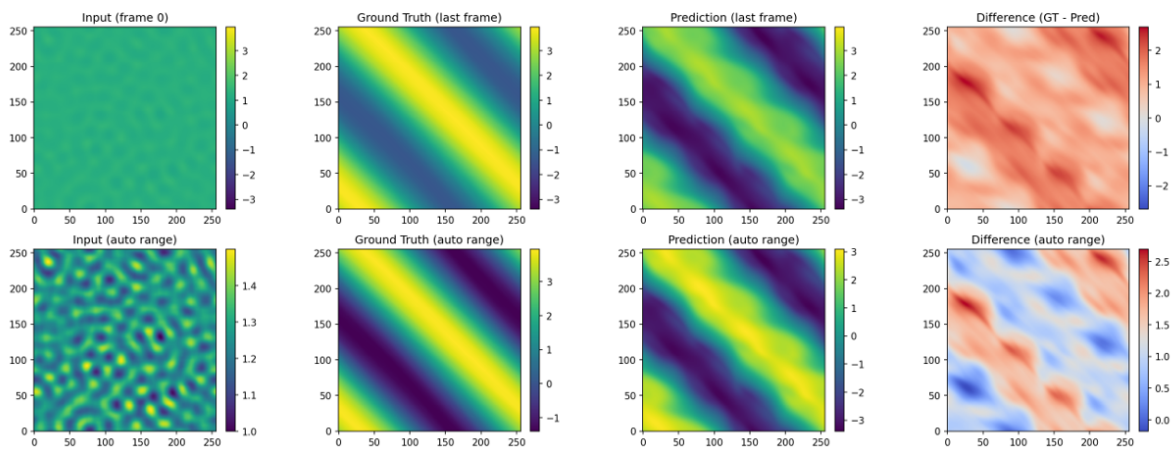


Figure 15: Unnormalized FNO 2D NS OOD Testing Sample 7

Dataset: dim2d\_nx256\_N10\_solver=exponax\_nu0.000\_t20.0\_test\_ntimepoints21\_NegLogGRF\_rq\_length\_scale0.200\_variance1.700\_alpha1.500\_exp\_factor2.500\_vmax1\_vmin-1\_batch0\_all\_frames | Index: 0 | RMSE=1.0781 MAE=0.8808 MAPE=686.61%  
 type=NegLogGRF\_rq | solver=exponax | nx=256 | N=10 | nu=0.000 | t=20.0 | ntimepoints=21 | length\_scale=0.200 | variance=1.700 | alpha=1.500 | exp\_factor=2.500 | vmax=1 | vmin=-1

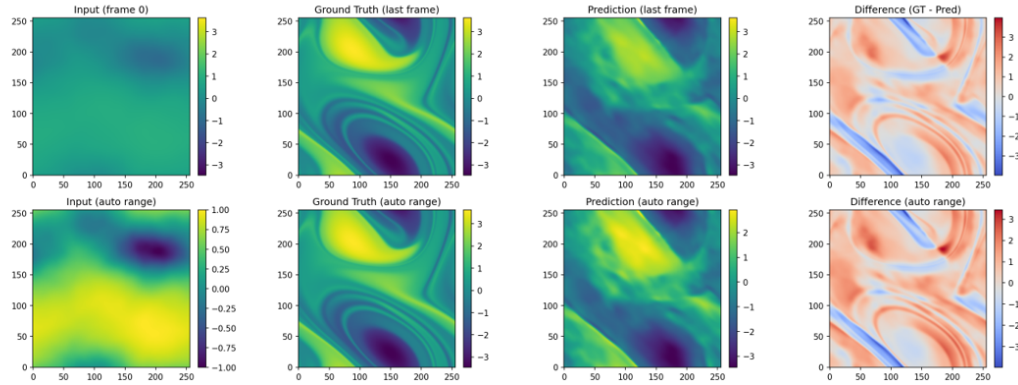


Figure 16: Unnormalized FNO 2D NS OOD Testing Sample 9

## Appendix: Attack Results

### D.2 FNO Burgers Results

Combined Loss Curves across approxN — file: gradient\_test\_exponax\_nu0.0005\_nsamples1 | under: nu=0.0005\_PGD\_results  
 norm: 2 | index: 0 | steps: 100 | epsilon: 10.0 | alpha: 0.05  
 approxN: 20,200,2000,20000

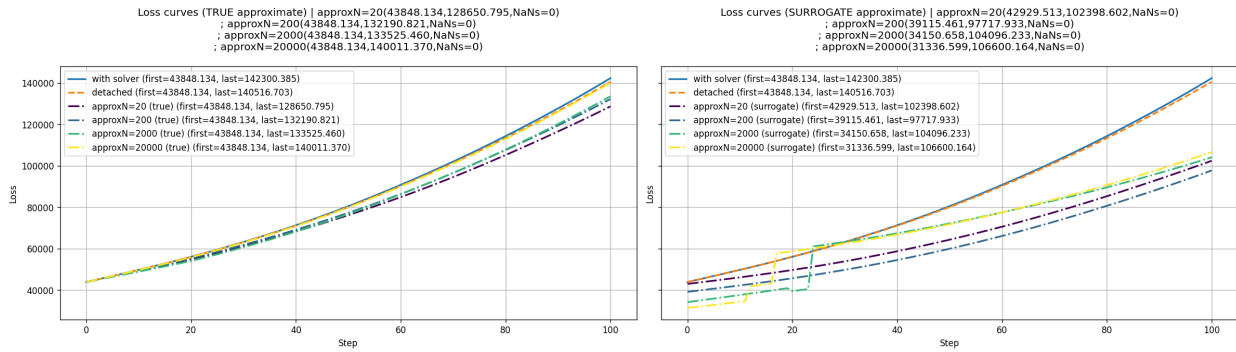


Figure 17: 1D Burgers  $\nu=0.0005$   $\text{norm}=2$   $\text{index}=0$   $\text{steps}=100$   $\text{epsilon}=10.0$   $\text{alpha}=0.05$   $\text{approxNs}(\text{dict size})=20,200,2000,20000$

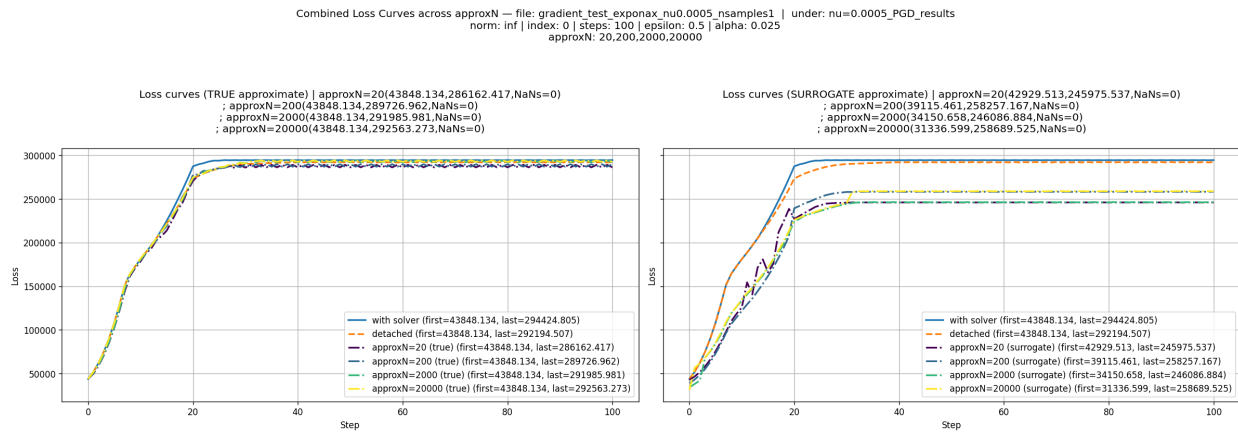


Figure 18: 1D Burgers  $\nu=0.0005$  norm=inf index=0 steps=100 epsilon=0.5 alpha=0.025 approxNs(dict size)=20,200,2000,20000

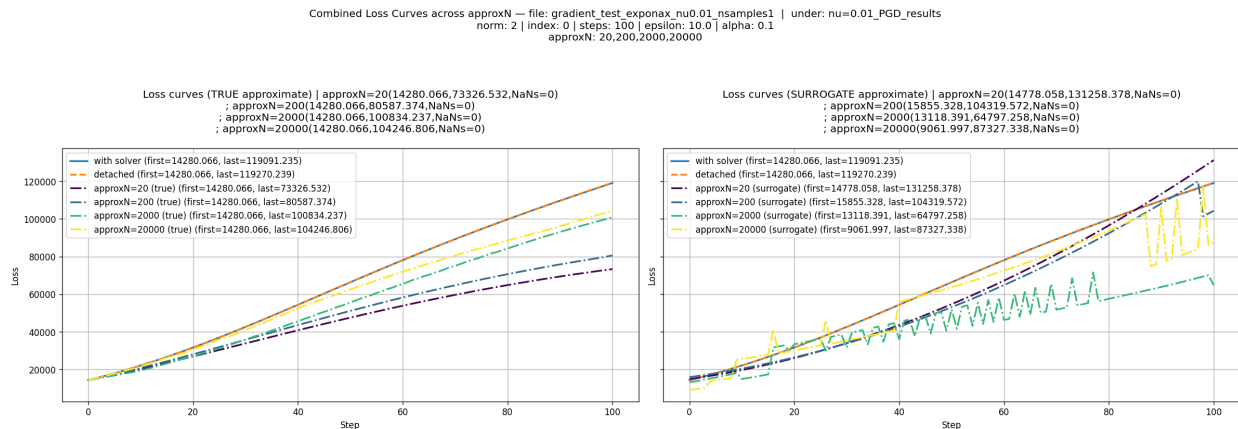


Figure 19: 1D Burgers  $\nu=0.01$  norm=2 index=0 steps=100 epsilon=10.0 alpha=0.1 approxNs(dict size)=20,200,2000,20000

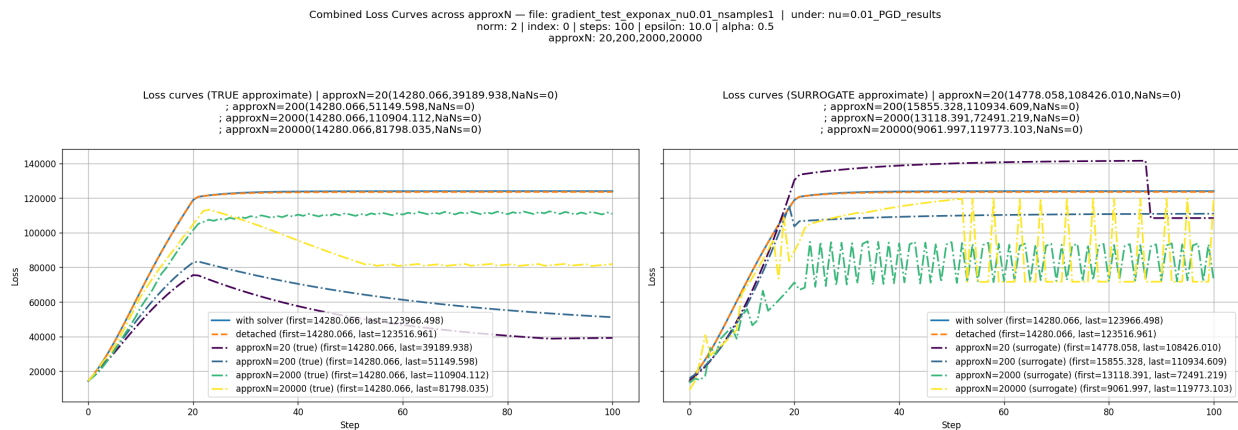


Figure 20: 1D Burgers  $\nu=0.01$  norm=2 index=0 steps=100 epsilon=10.0 alpha=0.5 approxNs(dict size)=20,200,2000,20000

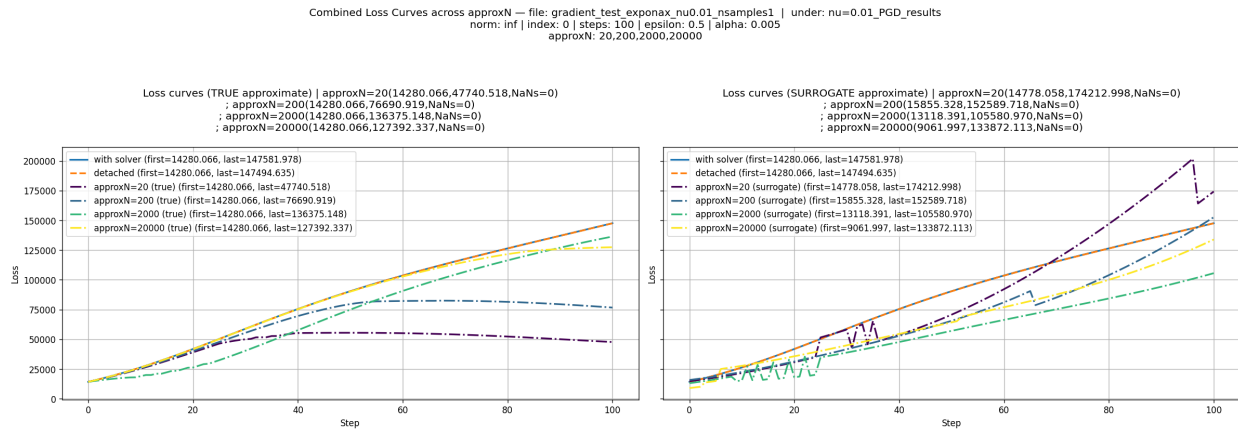


Figure 21: 1D Burgers  $\nu=0.01$  norm=inf index=0 steps=100 epsilon=0.5 alpha=0.005 approxNs(dict size)=20,200,2000,20000

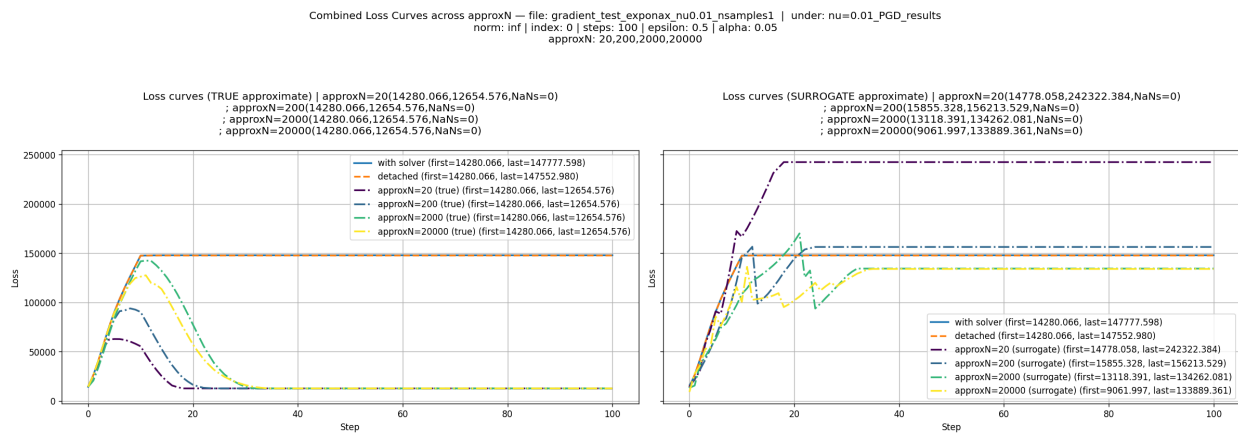


Figure 22: 1D Burgers  $\nu=0.01$  norm=inf index=0 steps=100 epsilon=0.5 alpha=0.05 approxNs(dict size)=20,200,2000,20000

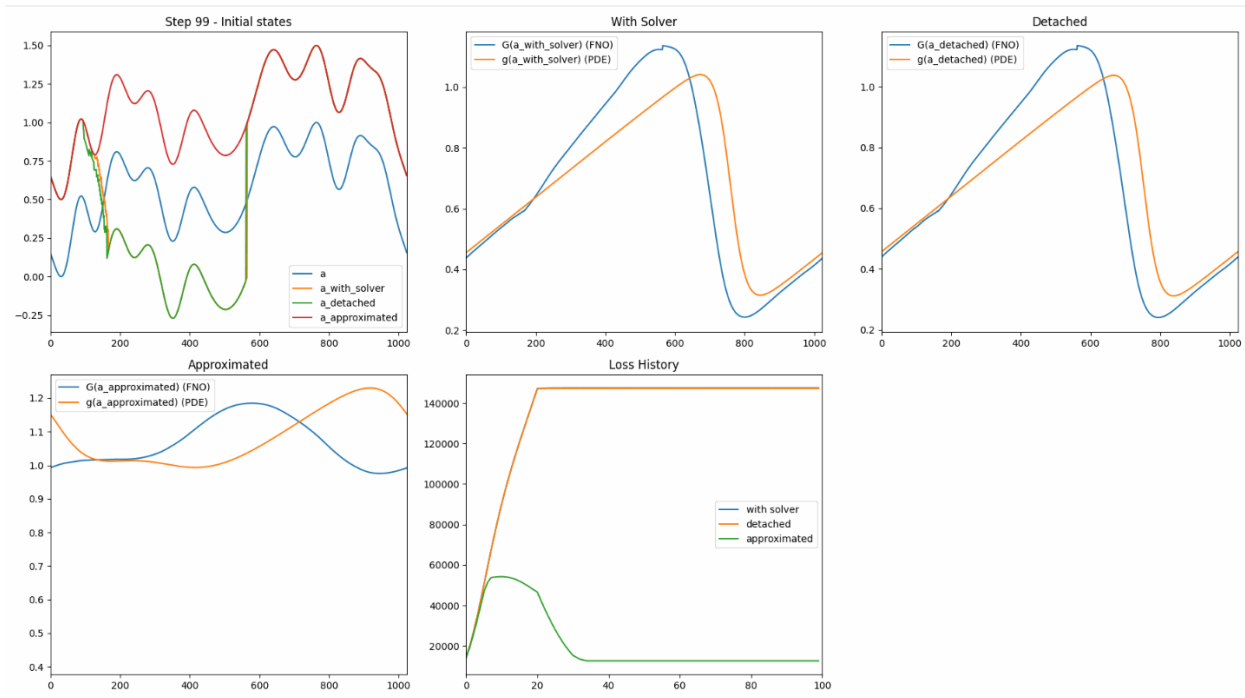


Figure 23: 1D Burgers  $\nu=0.01$   $\text{norm}=\text{inf}$   $\text{index}=0$   $\text{steps}=100$   $\text{epsilon}=0.5$   $\text{alpha}=0.0025$

### D.3 DeepONet Burgers Results

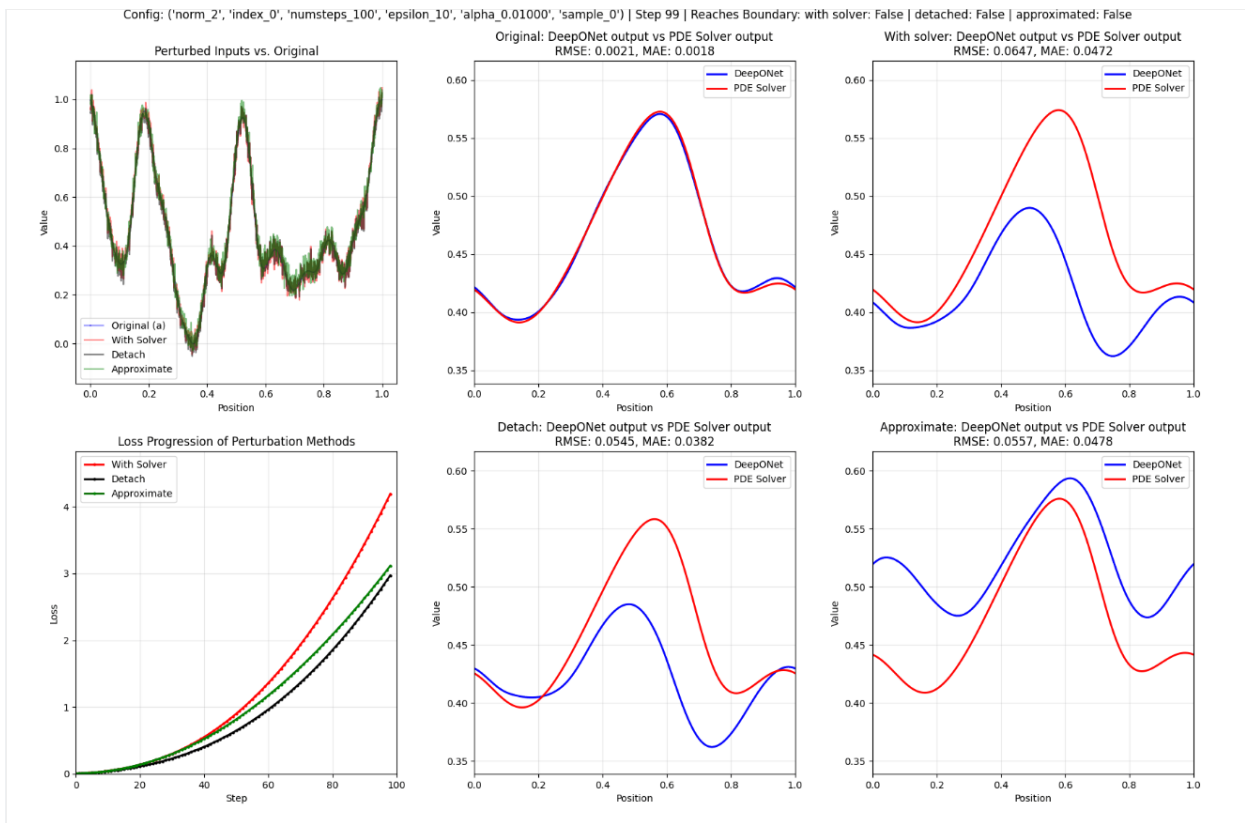


Figure 24: 1D Burgers  $\nu=0.01$   $\text{norm}=2$   $\text{index}=0$   $\text{steps}=100$   $\text{epsilon}=10$   $\text{alpha}=0.01$

Config: ('norm\_inf', 'index\_0', 'numsteps\_100', 'epsilon\_0.5', 'alpha\_0.02500', 'sample\_0') | Step 99 | Reaches Boundary: with solver: 0.9443359375 | detached: 0.7861328125 | approximated: 0.2802734375

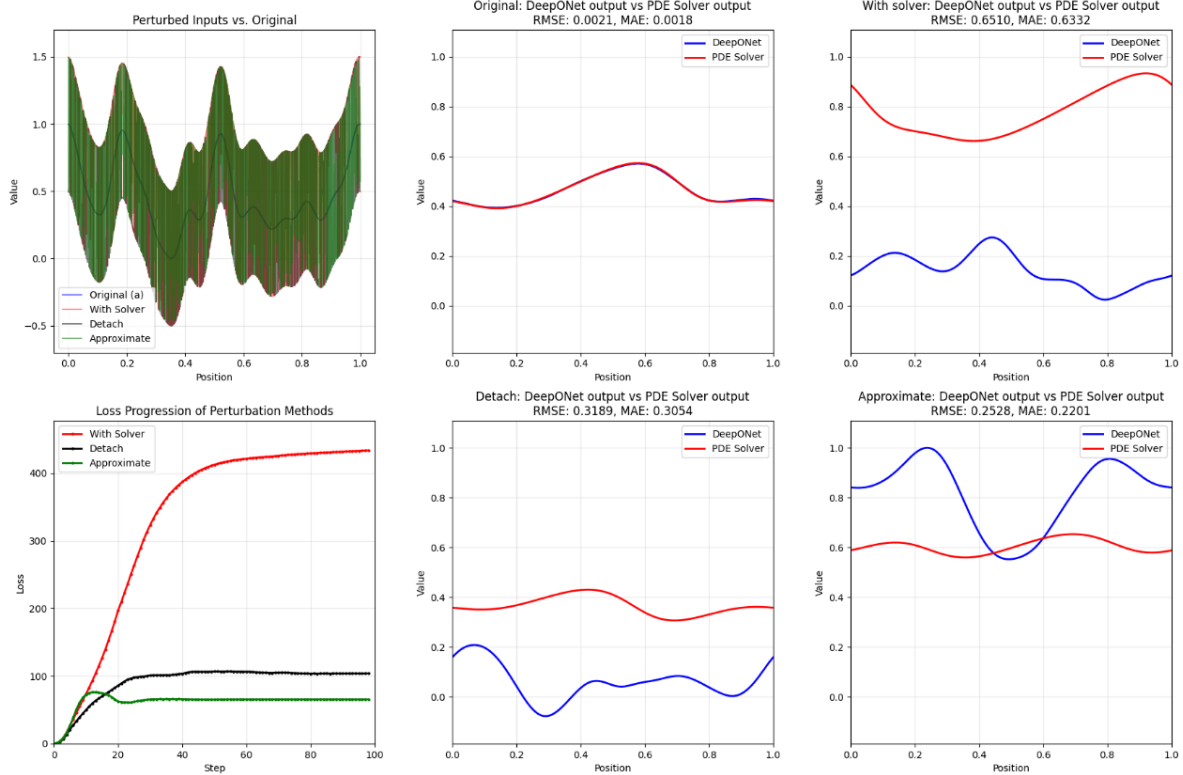


Figure 25: 1D Burgers  $\nu=0.01$   $\text{norm}=\text{inf}$   $\text{index}=0$   $\text{steps}=100$   $\text{epsilon}=0.5$   $\text{alpha}=0.025$

## D.4 FNO PGD Attack on 1D Burgers with Soft-DTW Loss

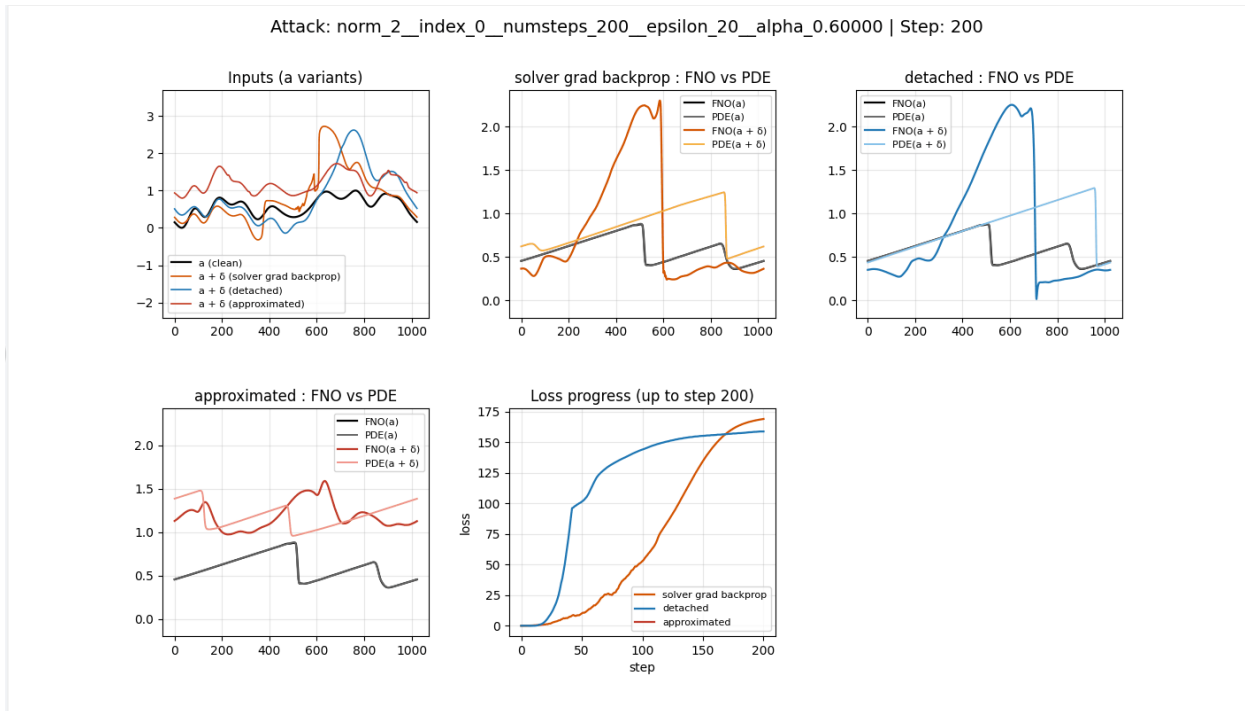


Figure 26: 1D Burgers  $\nu=0.01$  norm=2 index=0 steps=200 epsilon=20 alpha=0.6 Soft-DTW as loss  $\gamma=0.01$

## D.5 FNO Variants' Navier-Stokes Prediction Results

This shows the test rmse and mae of different variants of FNO on 2D NS test case. There are also T test on every pair of these variants to show that their prediction performances are significantly different. I chose the best variant here as the model in the attacking.

	Model	model_type	architecture	padding	modes1	modes2	modes3	width	epochs	Tin	Tout	Avg RMSE	Avg MAE
10	FNO	2d	recurrent		64	64		60	500	10	10	0.311532	0.213168
3	FNO	2d	recurrent		16	16		60	500	10	10	0.315702	0.216745
8	FNO	2d	recurrent		48	48		60	500	10	10	0.325217	0.223623
5	FNO	2d	recurrent		32	32		40	500	10	10	0.335240	0.234046
11	FNO	2d	recurrent		64	64		40	500	10	10	0.337644	0.235757
6	FNO	2d	recurrent		32	32		60	500	10	10	0.340296	0.230033
12	FNO	2d	recurrent		96	96		40	500	10	10	0.341112	0.237695
7	FNO	2d	recurrent		48	48		40	500	10	10	0.343496	0.239848
13	FNO	2d	recurrent		128	128		40	500	10	10	0.352749	0.244336
2	FNO	2d	recurrent		12	12		20	500	10	10	0.405792	0.287911
16	FNO	3d		no	64	64	6	60	500	10	10	0.505344	0.347536
17	FNO	3d		yes	32	32	8	40	500	10	10	0.527340	0.365085
14	FNO	3d		no	32	32	6	40	500	10	10	0.532029	0.371948
9	FNO	2d	recurrent		64	64		60	500	1	19	0.548878	0.376137
4	FNO	2d	recurrent		32	32		40	500	1	19	0.549336	0.387712
18	FNO	3d		yes	32	32	12	40	500	1	19	0.764626	0.544359
15	FNO	3d		no	32	32	8	40	500	1	19	0.807495	0.580186
1	FNO	2d	initial_to_final		64	64		60	500			0.825590	0.591958
0	FNO	2d	initial_to_final		32	32		40	500			0.868306	0.623773

Figure 27: Test RMSE and MAE for FNO of different variants and parameters

RMSE Comparison p-values  
(One-sided t-test: row model < column model)

FNO2d_recurrent_modes64_width60_epochs500_Tin10_T10 -	0.181	4.300 $\times 10^{-1}$	1.079 $\times 10^{-1}$	1.047 $\times 10^{-1}$	7.168 $\times 10^{-1}$	1.809 $\times 10^{-1}$	8.777 $\times 10^{-1}$	1.122 $\times 10^{-1}$	1.505 $\times 10^{-1}$	1.319 $\times 10^{-1}$	8.199 $\times 10^{-1}$	1.045 $\times 10^{-1}$	1.138 $\times 10^{-1}$	6.327 $\times 10^{-1}$	0.336 $\times 10^{-1}$	2.943 $\times 10^{-1}$	4.540 $\times 10^{-1}$	2.889 $\times 10^{-1}$			
FNO2d_recurrent_modes16_width60_epochs500_Tin10_T10	0.817	1.627 $\times 10^{-1}$	4.565 $\times 10^{-1}$	2.011 $\times 10^{-1}$	1.746 $\times 10^{-1}$	1.713 $\times 10^{-1}$	5.030 $\times 10^{-1}$	5.807 $\times 10^{-1}$	1.214 $\times 10^{-1}$	1.699 $\times 10^{-1}$	6.796 $\times 10^{-1}$	1.041 $\times 10^{-1}$	1.528 $\times 10^{-1}$	9.380 $\times 10^{-1}$	6.498 $\times 10^{-1}$	1.653 $\times 10^{-1}$	4.966 $\times 10^{-1}$	4.168 $\times 10^{-1}$			
FNO2d_recurrent_modes48_width60_epochs500_Tin10_T10	0.997	0.964	4.919 $\times 10^{-1}$	2.104 $\times 10^{-1}$	7.299 $\times 10^{-1}$	2.126 $\times 10^{-1}$	1.822 $\times 10^{-1}$	3.309 $\times 10^{-1}$	5.219 $\times 10^{-1}$	1.329 $\times 10^{-1}$	2.255 $\times 10^{-1}$	5.212 $\times 10^{-1}$	1.518 $\times 10^{-1}$	2.491 $\times 10^{-1}$	1.180 $\times 10^{-1}$	6.605 $\times 10^{-1}$	2.457 $\times 10^{-1}$	7.939 $\times 10^{-1}$			
FNO2d_recurrent_modes32_width40_epochs500_Tin10_T10	1.000	1.000	0.951	0.333	0.161	0.111	0.064	1.174 $\times 10^{-1}$	2.495 $\times 10^{-1}$	4.261 $\times 10^{-1}$	4.202 $\times 10^{-1}$	1.899 $\times 10^{-1}$	1.853 $\times 10^{-1}$	4.448 $\times 10^{-1}$	1.626 $\times 10^{-1}$	1.308 $\times 10^{-1}$	3.385 $\times 10^{-1}$	4.767 $\times 10^{-1}$			
FNO2d_recurrent_modes64_width40_epochs500_Tin10_T10	1.000	1.000	0.979	0.667	0.328	0.265	0.170	7.219 $\times 10^{-1}$	6.897 $\times 10^{-1}$	8.088 $\times 10^{-1}$	2.356 $\times 10^{-1}$	4.070 $\times 10^{-1}$	1.246 $\times 10^{-1}$	2.588 $\times 10^{-1}$	6.537 $\times 10^{-1}$	9.073 $\times 10^{-1}$	5.081 $\times 10^{-1}$	1.522 $\times 10^{-1}$			
FNO2d_recurrent_modes32_width60_epochs500_Tin10_T10	1.000	1.000	0.993	0.839	0.672	0.448	0.271	9.863 $\times 10^{-1}$	3.894 $\times 10^{-1}$	1.289 $\times 10^{-1}$	1.048 $\times 10^{-1}$	2.094 $\times 10^{-1}$	1.482 $\times 10^{-1}$	9.364 $\times 10^{-1}$	2.560 $\times 10^{-1}$	9.624 $\times 10^{-1}$	8.906 $\times 10^{-1}$	1.199 $\times 10^{-1}$			
FNO2d_recurrent_modes96_width40_epochs500_Tin10_T10	1.000	1.000	0.998	0.889	0.735	0.552	0.335	1.561 $\times 10^{-1}$	7.114 $\times 10^{-1}$	3.551 $\times 10^{-1}$	1.377 $\times 10^{-1}$	3.597 $\times 10^{-1}$	1.482 $\times 10^{-1}$	5.406 $\times 10^{-1}$	9.004 $\times 10^{-1}$	5.630 $\times 10^{-1}$	1.320 $\times 10^{-1}$	1.072 $\times 10^{-1}$			
FNO2d_recurrent_modes48_width40_epochs500_Tin10_T10	1.000	1.000	0.998	0.936	0.830	0.729	0.665	7.619 $\times 10^{-1}$	1.463 $\times 10^{-1}$	1.530 $\times 10^{-1}$	1.742 $\times 10^{-1}$	3.085 $\times 10^{-1}$	4.065 $\times 10^{-1}$	4.743 $\times 10^{-1}$	4.772 $\times 10^{-1}$	1.141 $\times 10^{-1}$	3.975 $\times 10^{-1}$	3.715 $\times 10^{-1}$			
FNO2d_recurrent_modes128_width40_epochs500_Tin10_T10	1.000	1.000	1.000	1.000	0.993	0.990	0.984	0.974	1.241 $\times 10^{-1}$	1.091 $\times 10^{-1}$	8.766 $\times 10^{-1}$	2.775 $\times 10^{-1}$	1.407 $\times 10^{-1}$	5.676 $\times 10^{-1}$	3.234 $\times 10^{-1}$	6.684 $\times 10^{-1}$	1.581 $\times 10^{-1}$	7.927 $\times 10^{-1}$			
FNO2d_recurrent_modes12_width20_epochs500_Tin10_T10	1.000	1.000	1.000	1.000	1.000	1.000	1.000	1.000	5.888 $\times 10^{-1}$	7.849 $\times 10^{-1}$	2.308 $\times 10^{-1}$	2.598 $\times 10^{-1}$	1.239 $\times 10^{-1}$	3.601 $\times 10^{-1}$	4.251 $\times 10^{-1}$	2.376 $\times 10^{-1}$	5.302 $\times 10^{-1}$	1.072 $\times 10^{-1}$			
FNO3d_no_padding_modes1264_modes36_width60_epochs500_Tin10_T10_no_padding	1.000	1.000	1.000	1.000	1.000	1.000	1.000	1.000	1.000	1.000	1.000	1.000	1.000	1.158 $\times 10^{-1}$	2.729 $\times 10^{-1}$	9.352 $\times 10^{-1}$	1.446 $\times 10^{-1}$	4.548 $\times 10^{-1}$	3.219 $\times 10^{-1}$	6.499 $\times 10^{-1}$	6.802 $\times 10^{-1}$
FNO3d_padding_modes1232_modes38_width40_epochs500_Tin10_T10_padding	1.000	1.000	1.000	1.000	1.000	1.000	1.000	1.000	1.000	0.999	0.764	0.090	0.125	9.099 $\times 10^{-1}$	7.797 $\times 10^{-1}$	2.539 $\times 10^{-1}$	4.528 $\times 10^{-1}$	1.072 $\times 10^{-1}$	1.072 $\times 10^{-1}$	1.072 $\times 10^{-1}$	1.072 $\times 10^{-1}$
FNO3d_no_padding_modes1232_modes36_width40_epochs500_Tin10_T10_no_padding	1.000	1.000	1.000	1.000	1.000	1.000	1.000	1.000	1.000	1.000	0.736	0.190	0.210	3.183 $\times 10^{-1}$	4.808 $\times 10^{-1}$	1.247 $\times 10^{-1}$	1.240 $\times 10^{-1}$	1.072 $\times 10^{-1}$	1.072 $\times 10^{-1}$	1.072 $\times 10^{-1}$	1.072 $\times 10^{-1}$
FNO2d_recurrent_modes64_width60_epochs500_Tin1_T19	1.000	1.000	1.000	1.000	1.000	1.000	1.000	1.000	1.000	0.991	0.910	0.810	0.490	2.881 $\times 10^{-1}$	3.312 $\times 10^{-1}$	1.317 $\times 10^{-1}$	1.346 $\times 10^{-1}$	1.072 $\times 10^{-1}$	1.072 $\times 10^{-1}$	1.072 $\times 10^{-1}$	1.072 $\times 10^{-1}$
FNO2d_recurrent_modes32_width40_epochs500_Tin1_T19	1.000	1.000	1.000	1.000	1.000	1.000	1.000	1.000	1.000	0.986	0.875	0.790	0.510	4.284 $\times 10^{-1}$	2.451 $\times 10^{-1}$	6.510 $\times 10^{-1}$	7.409 $\times 10^{-1}$	1.072 $\times 10^{-1}$	1.072 $\times 10^{-1}$	1.072 $\times 10^{-1}$	1.072 $\times 10^{-1}$
FNO3d_padding_modes1232_modes312_width40_epochs500_Tin1_T19_padding	1.000	1.000	1.000	1.000	1.000	1.000	1.000	1.000	1.000	1.000	1.000	1.000	1.000	6.068 $\times 10^{-1}$	2.940 $\times 10^{-1}$	2.590 $\times 10^{-1}$	1.072 $\times 10^{-1}$				
FNO3d_no_padding_modes1232_modes38_width40_epochs500_Tin1_T19_no_padding	1.000	1.000	1.000	1.000	1.000	1.000	1.000	1.000	1.000	1.000	1.000	1.000	1.000	0.999	0.118	2.766 $\times 10^{-1}$	1.072 $\times 10^{-1}$				
FNO2d_initial_to_final_modes64_width60_epochs500	1.000	1.000	1.000	1.000	1.000	1.000	1.000	1.000	1.000	1.000	1.000	1.000	1.000	1.000	1.000	0.842	1.848 $\times 10^{-1}$	1.072 $\times 10^{-1}$	1.072 $\times 10^{-1}$	1.072 $\times 10^{-1}$	1.072 $\times 10^{-1}$
FNO2d_initial_to_final_modes32_width40_epochs500	1.000	1.000	1.000	1.000	1.000	1.000	1.000	1.000	1.000	1.000	1.000	1.000	1.000	1.000	1.000	1.000	1.000	1.000	1.000	1.000	1.000

p < 0.05 (significant)

p ≥ 0.05 (not significant)

Figure 28: Test RMSE T test for FNO of different variants and parameters

## D.6 Other Architectures of FNO 2D Navier-Stokes Attack

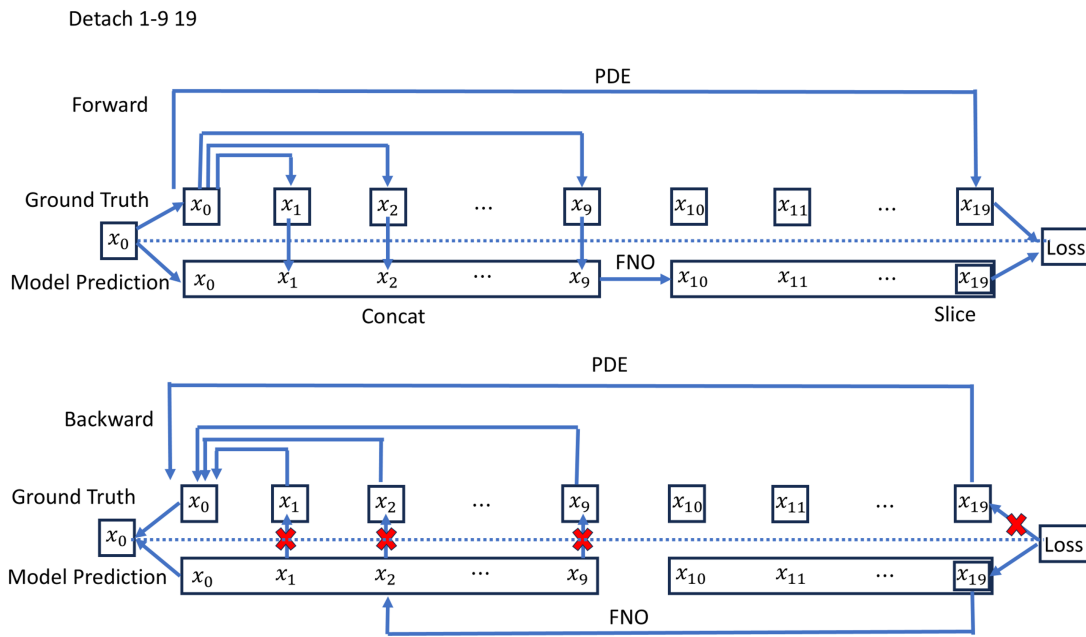


Figure 29: 2D NS PGD attack illustration (detached)

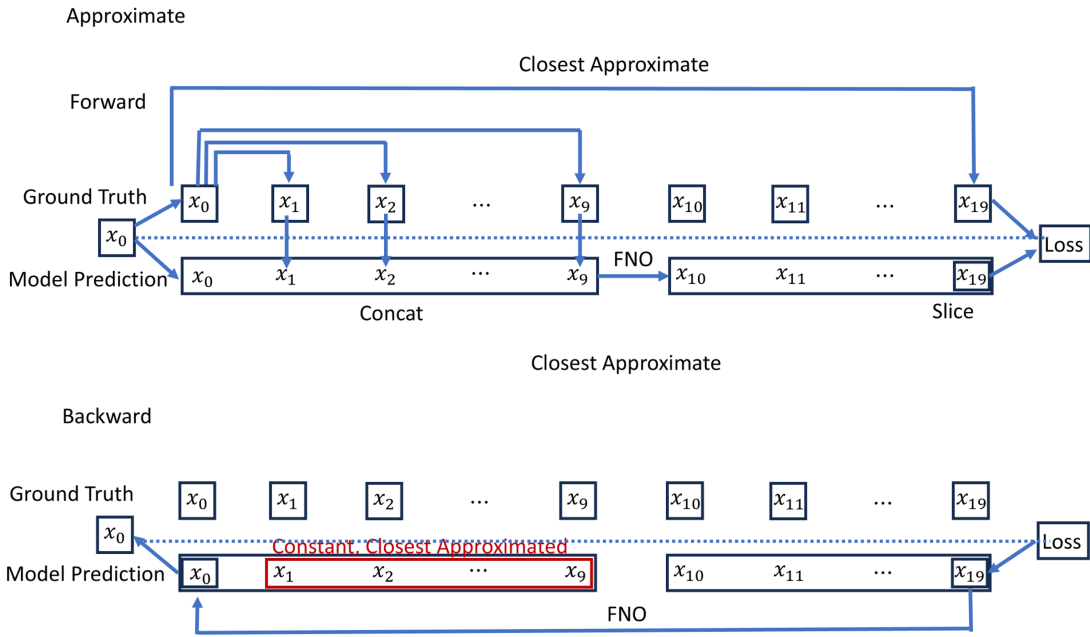


Figure 30: 2D NS PGD attack illustration (approximated)

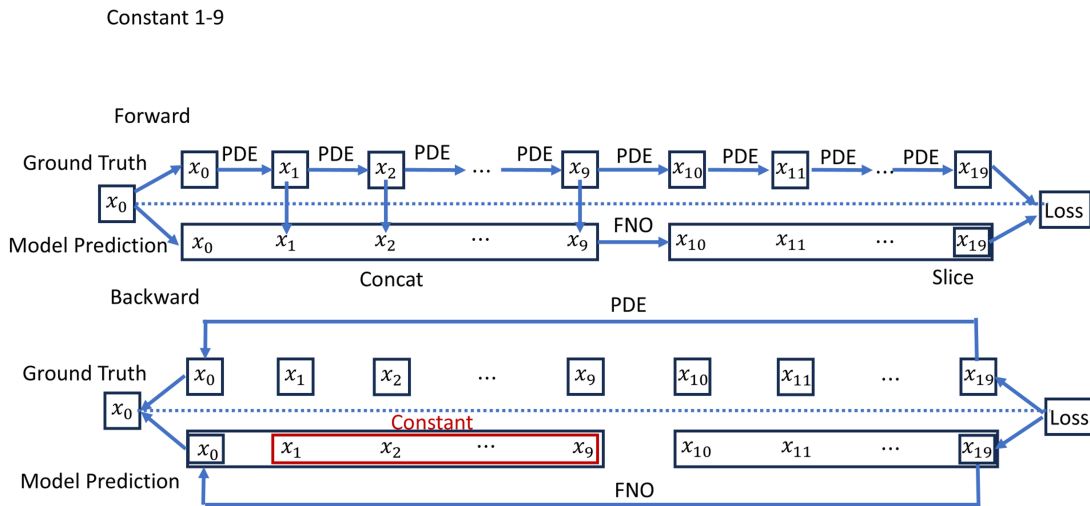


Figure 31: 2D NS PGD attack illustration (constant)

## D.7 FNO 2D Navier-Stokes Results

The results here show that with solver gradient back prop method gives the largest final loss and fastest loss growth. The approximated method's loss here is surrogate loss (computed using the closest surrogate ground truth in the pre-calculated dictionary). I did some ablation study by detaching some frames in the back prop and using approximated values or keeping some values constant. We can see with solver methods gives the largest difference in the heatmap, and the most prominent perturbed initial condition. One interesting observation is that excluding many frames' gradient back propagation causes the loss to oscillate in a periodic manner, unable to keep at a large final loss.

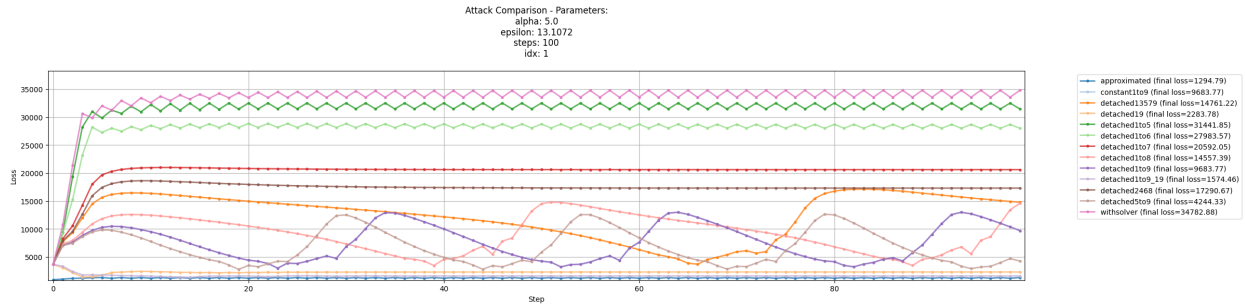


Figure 32: 2D NS PGD attack loss progression alpha=5.0 epsilon=13.1072 steps=100

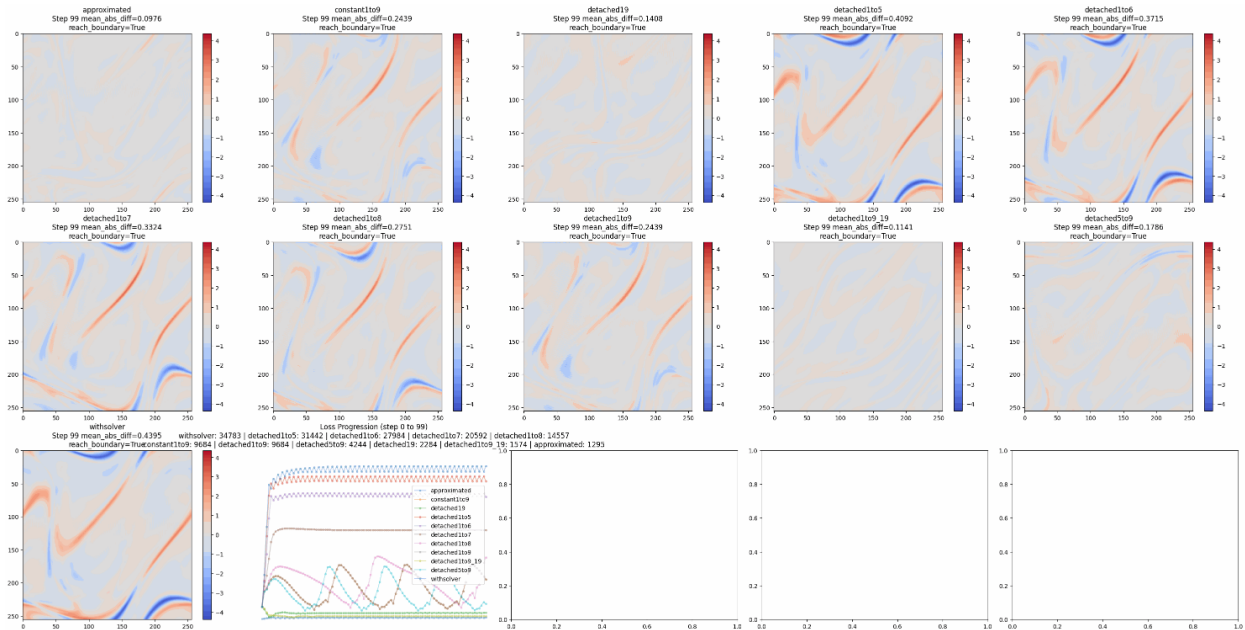


Figure 33: 2D NS PGD attack FNO and PDE solver output final difference alpha=5.0 epsilon=13.1072 steps=100

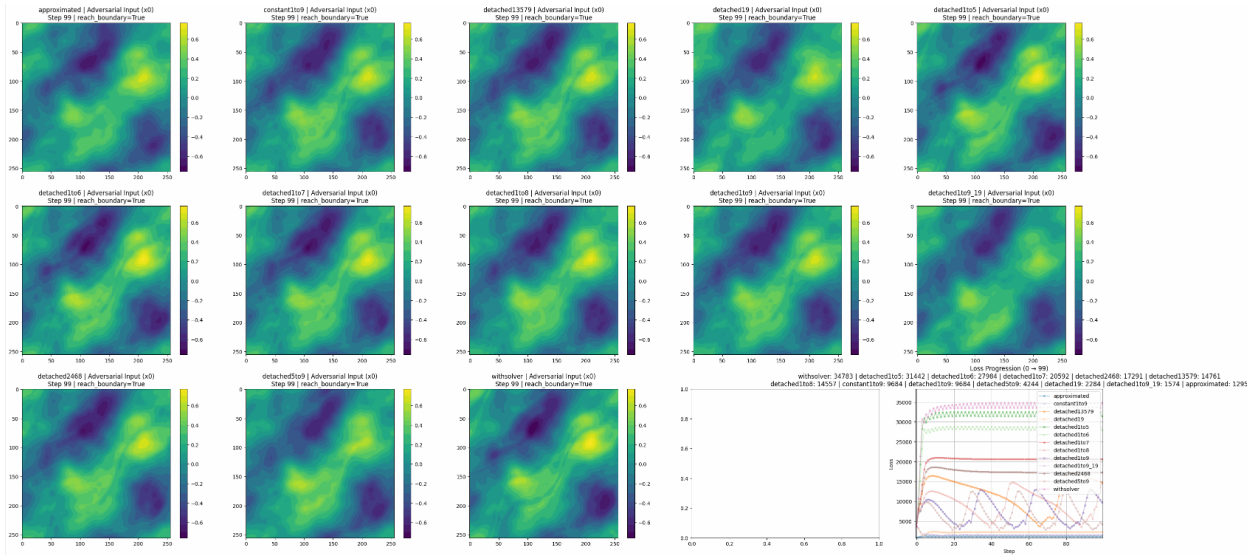


Figure 34: 2D NS PGD attack final perturbed initial condition  $\alpha=5.0$   $\epsilon=13.1072$  steps=100

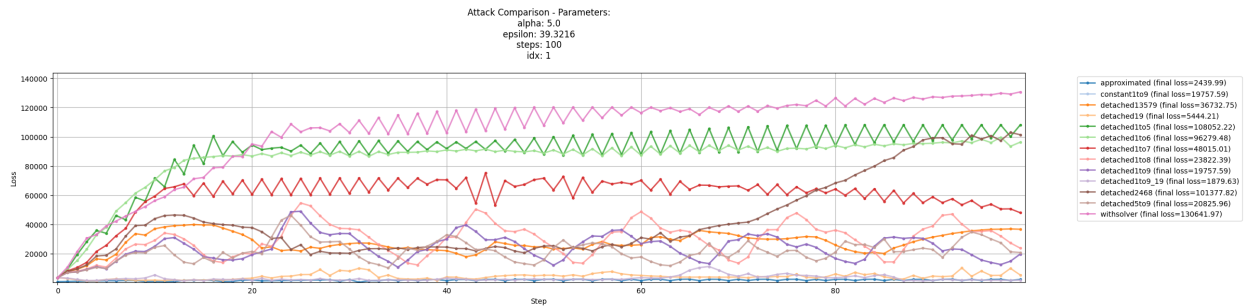


Figure 35: 2D NS PGD attack loss progression  $\alpha=5.0$   $\epsilon=39.3216$  steps=100

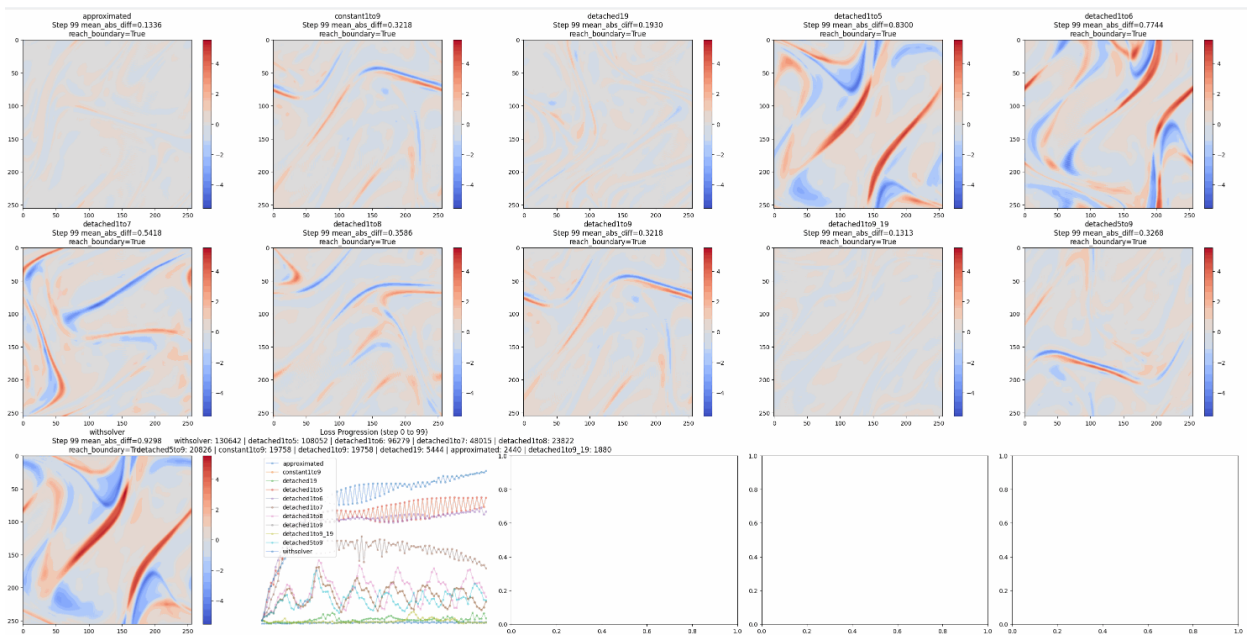


Figure 36: 2D NS PGD attack FNO and PDE solver output final difference  $\alpha=5.0$   $\epsilon=39.3216$  steps=100

In [39], it requires that all velocity, vorticity and external forcing are of periodic boundary condition. The empirical finding shows that our generated perturbed initial conditions in this PGD attack manner involving both PDE solver and FNO are indeed of periodic boundary condition. By computing the gradient and hessian of the final perturbed initial condition and back propped gradient at every step, it is obvious there is no discernible boundary when patching four of the repeated function in a periodic manner. I suspect this is because our whole setting is periodic: data is generated in a periodic boundary NS setting, FNO parametrizes the neural network in Fourier domain, and the PDE solver exponax uses pseudo-spectral method by also utilizing Fourier transform. The back propagated gradient of the initial condition against final loss through the combination of PDE solver and FNO is of periodic boundary condition.

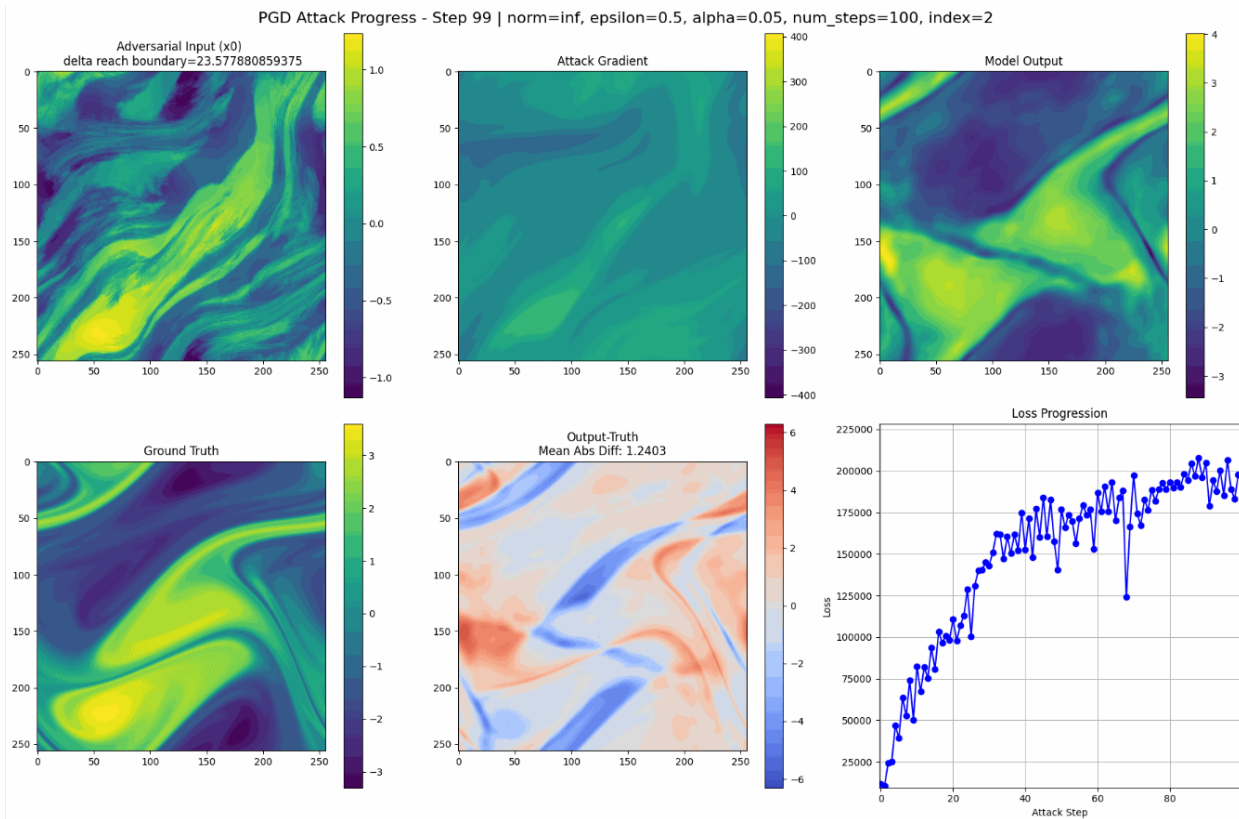


Figure 37: 2D NS PGD attack results norm=inf alpha=0.05 epsilon=0.5 steps=100 index=2

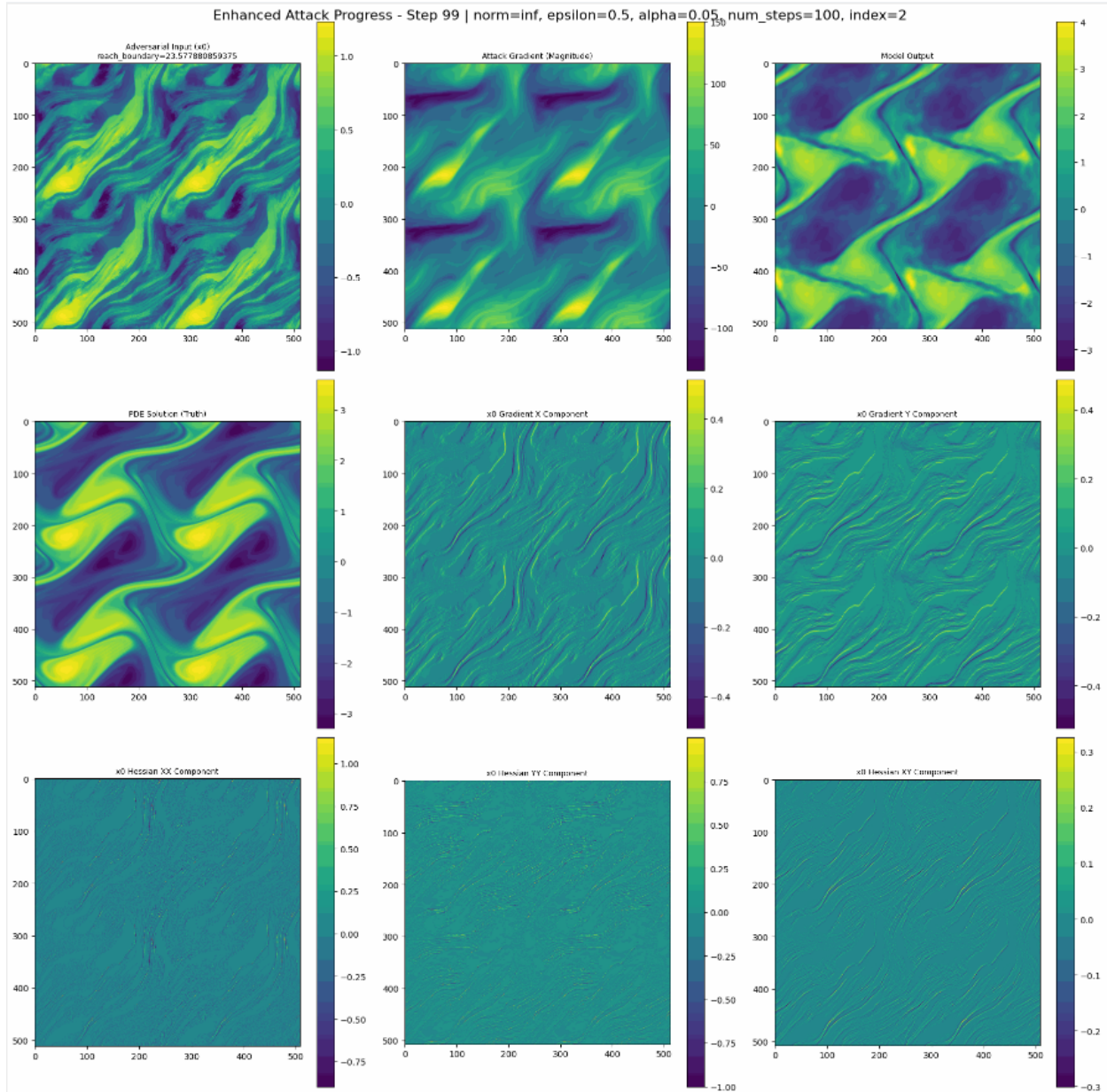


Figure 38: 2D NS PGD attack results norm=inf alpha=0.05 epsilon=0.5 steps=100 index=2 final step perturbed initial condition's gradient and hessian

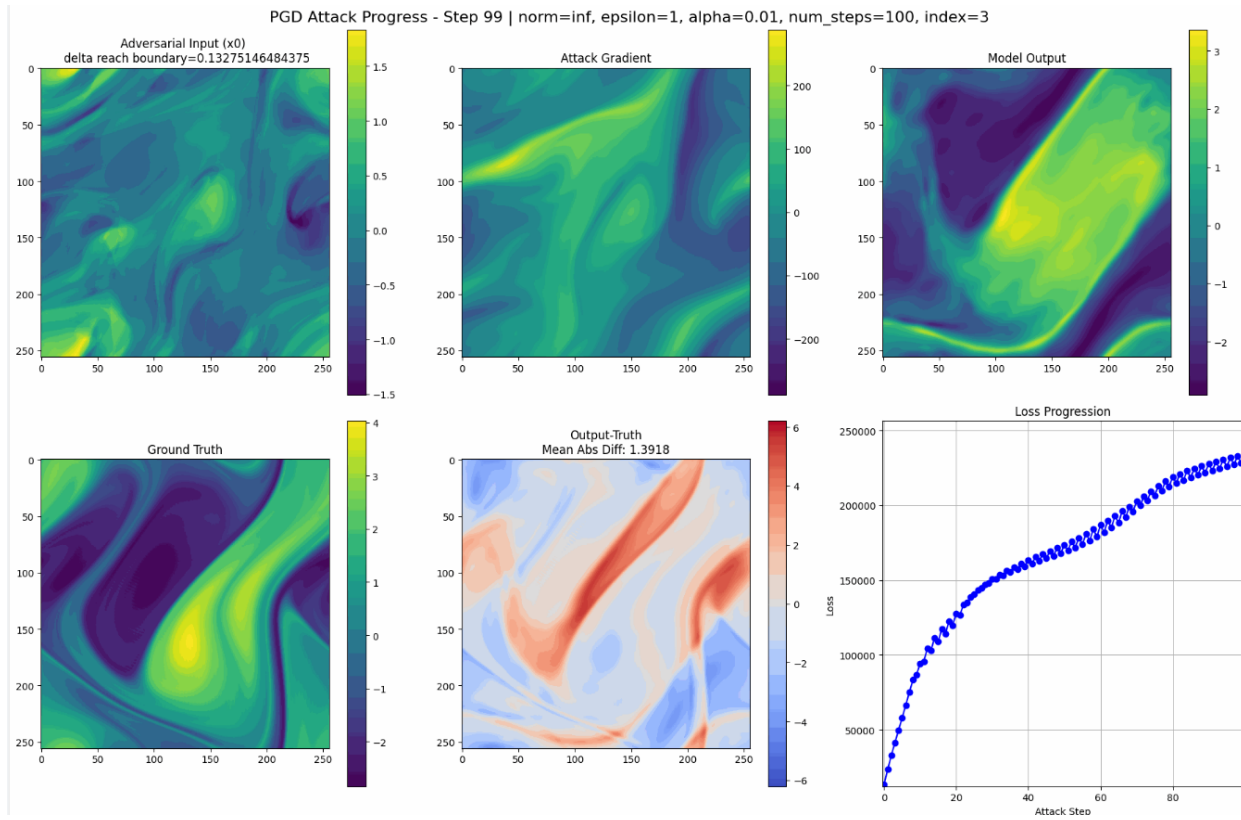


Figure 39: 2D NS PGD attack results norm=inf alpha=0.01 epsilon=1 steps=100 index=3

The ablation study on alpha (step size in PGD attack) indicates that alpha may control the period of the oscillation found above.

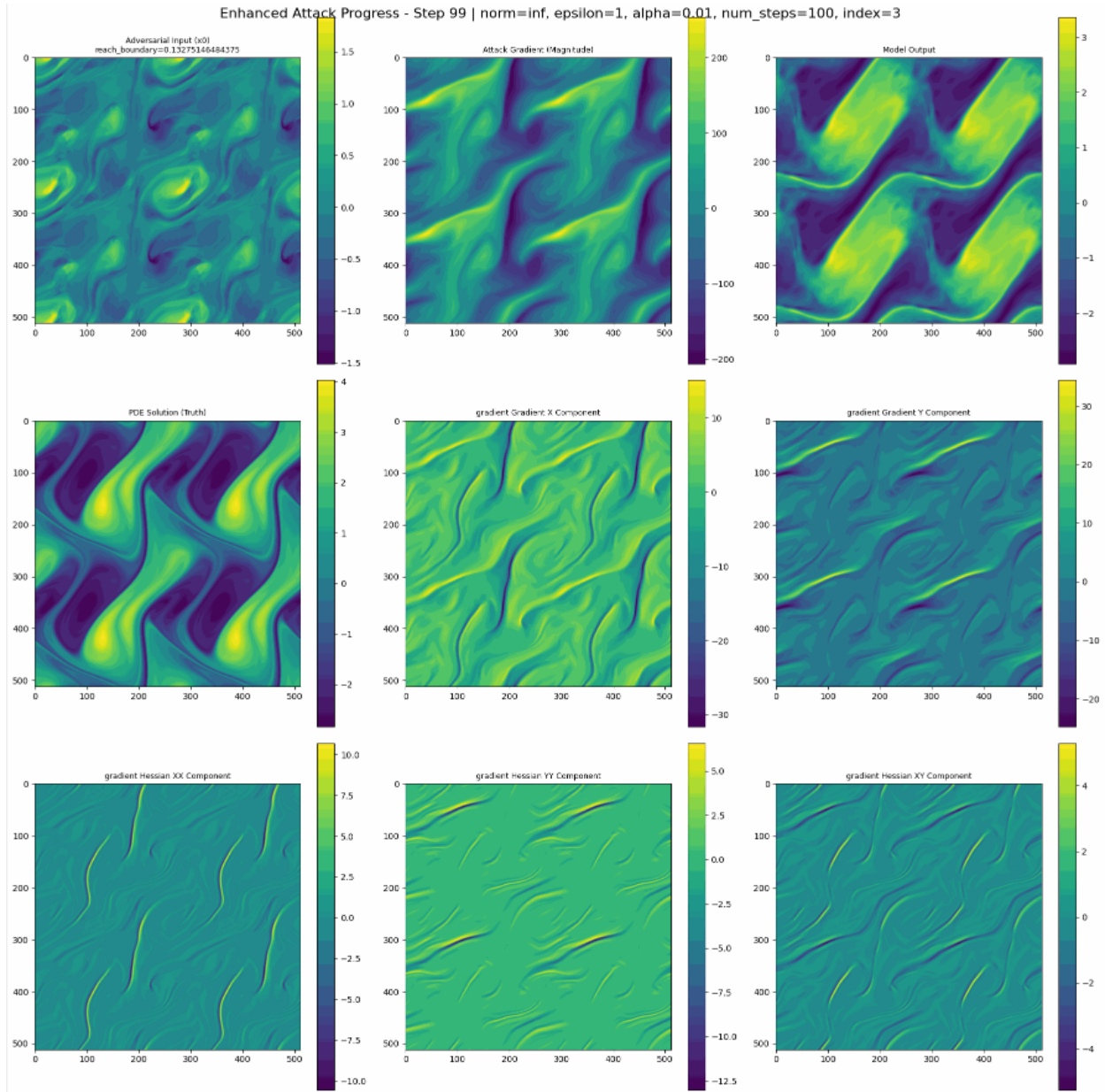


Figure 40: 2D NS PGD attack results norm=inf alpha=0.01 epsilon=1 steps=100 index=3 final step gradient's gradient and hessian

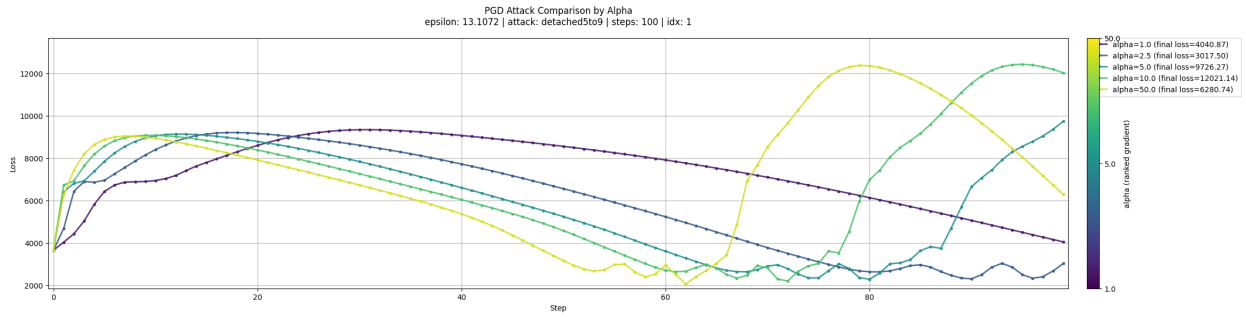


Figure 41: 2D NS PGD attack (detach5to9) alpha ablation study results norm=2 epsilon=13.1072 steps=100 index=1 loss progression

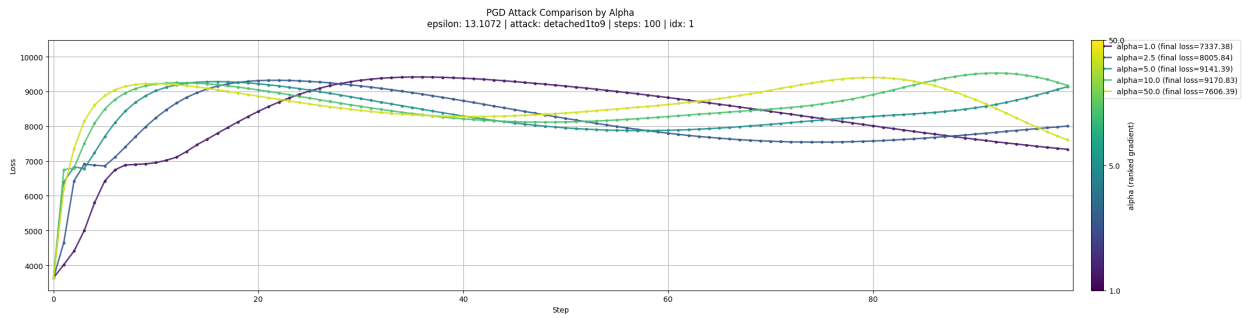


Figure 42: 2D NS PGD attack (detach1to9) alpha ablation study results norm=2 epsilon=13.1072 steps=100 index=1 loss progression

These results show the loss progression of using adam to update perturbed initial condition based on back propped gradient and not using adam (vanilla PGD method). Results suggest adam has the effect of smoothing out the oscillation in loss progression but could lead to lower final loss.

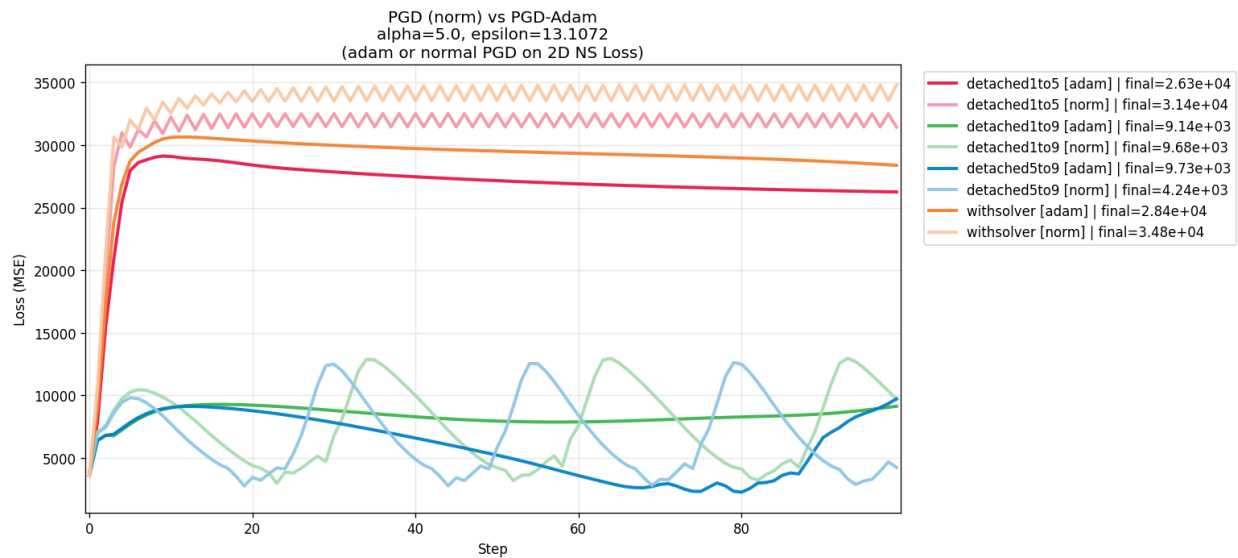


Figure 43: 2D NS PGD attack alpha=5 epsilon=13.1072 steps=100 loss progression

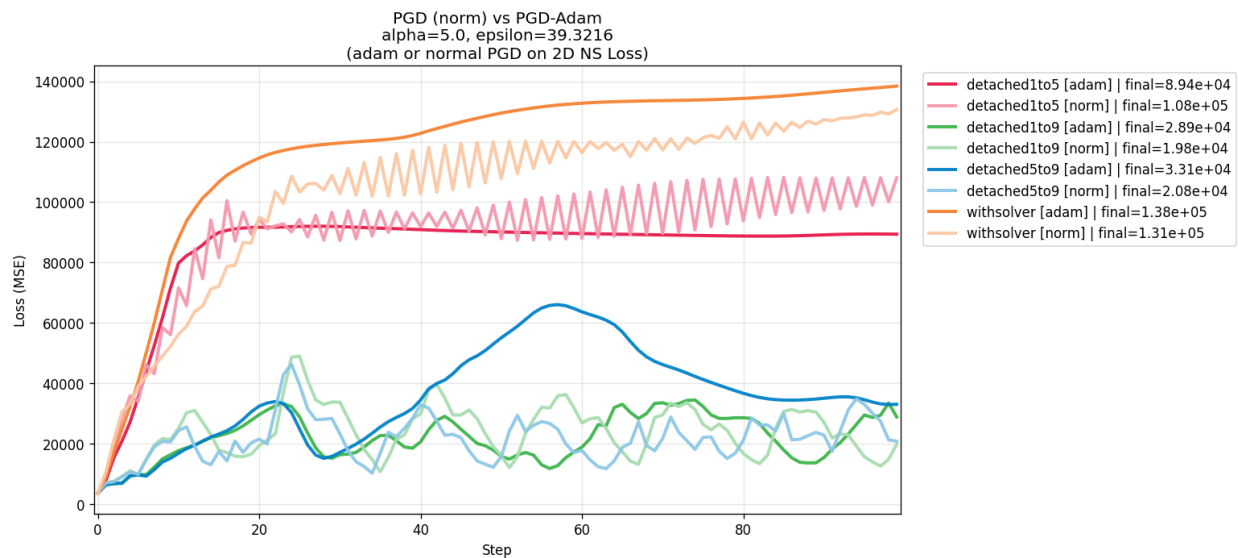


Figure 44: 2D NS PGD attack alpha=5 epsilon=39.3216 steps=100 loss progression

## D.8 FNO 2D NS Case Perturbation Examples and Average

The 1-4 rows of the next two plots represent the perturbed initial condition, final condition of the perturbed initial condition, generated perturbation on the initial condition, and the final condition difference between the perturbed and unperturbed initial conditions. We can see the perturbation shows a roughly 45 degree diagonal patterns.

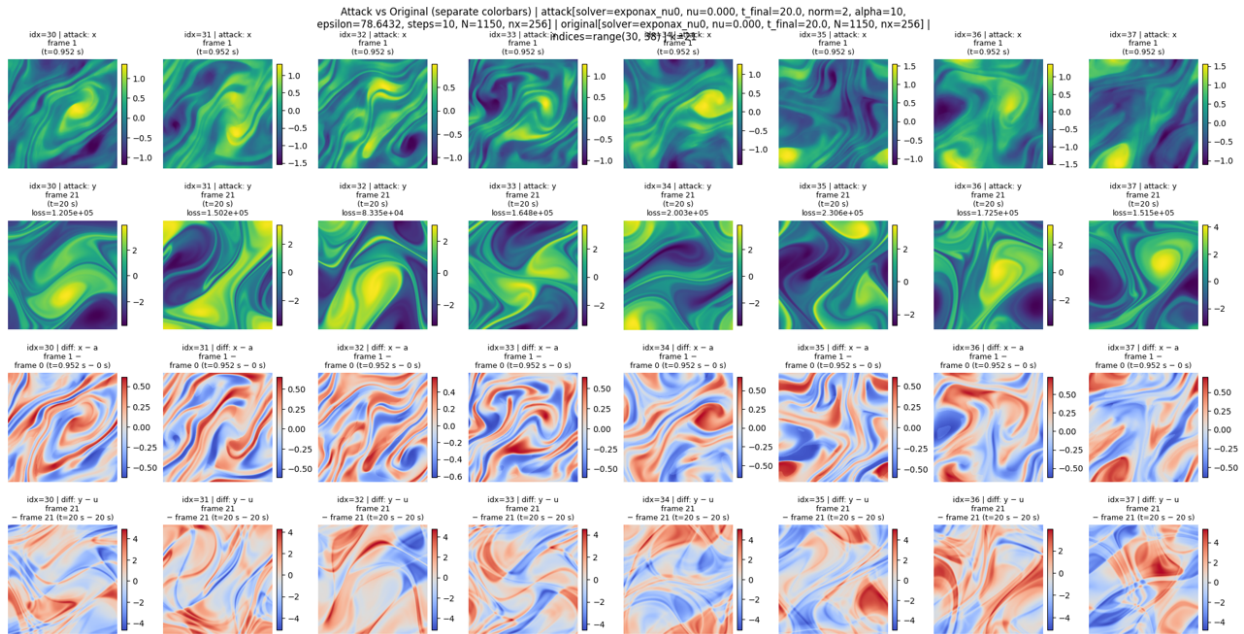


Figure 45: 2D NS PGD attack examples alpha=10 epsilon=78.6432 steps=10 loss progression

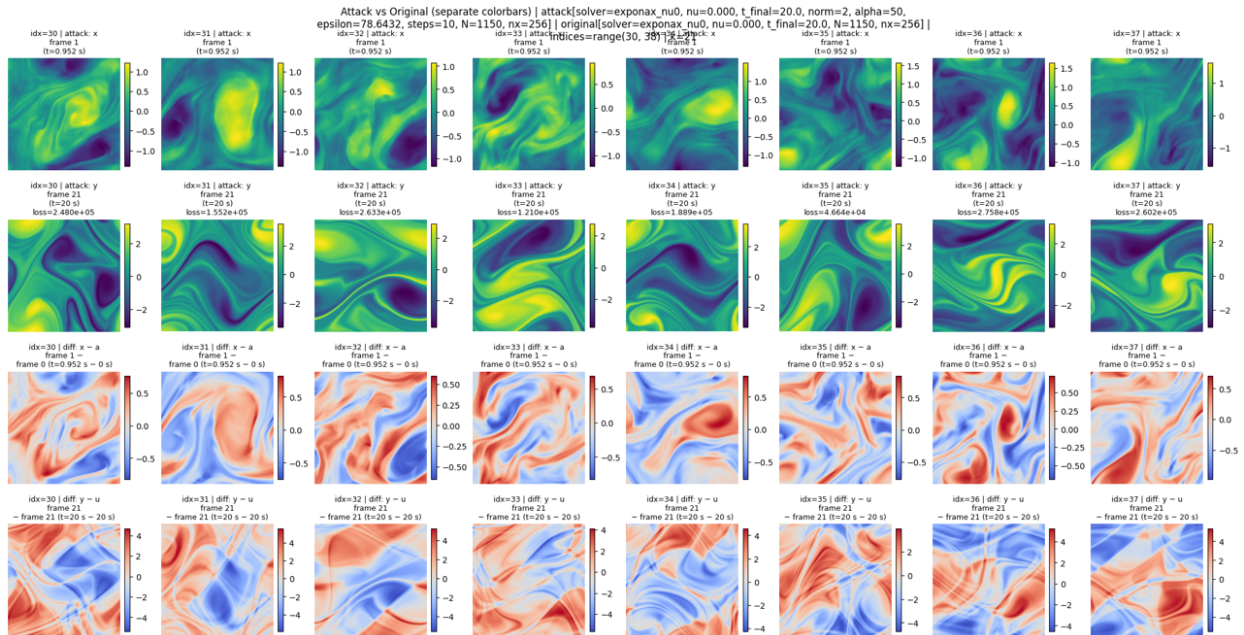


Figure 46: 2D NS PGD attack examples alpha=50 epsilon=78.6432 steps=10 loss progression

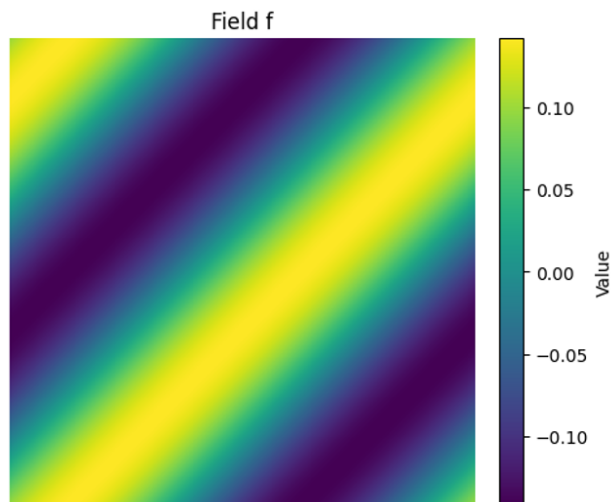


Figure 47: 2D NS dataset external forcing pattern (diagonal)  
This actually means the curl of force here.

Mean over first N=500 records | Attack y(k) vs Difference y(k)-u(k) | attack[solver=exponax\_nu0, nu=0.000, t\_final=20.0, norm=2, alpha=10, epsilon=39.3216, steps=10, N=500, nx=256] | original[solver=exponax\_nu0, nu=0.000, t\_final=20.0, N=1150, nx=256]

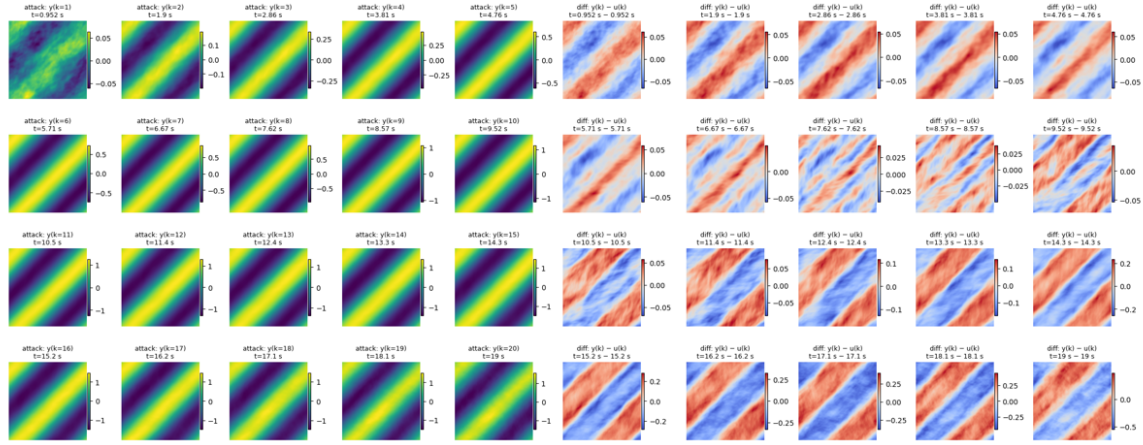


Figure 48: 2D NS dataset and perturbed result evolution difference

Left part of the plot shows the averaged evolution of perturbed initial condition, while right part of the plot shows the averaged difference of the original and perturbed initial condition.

The first image of the right part shows the averaged perturbation generated by our method. It undoubtedly reflects the external forcing on the system.

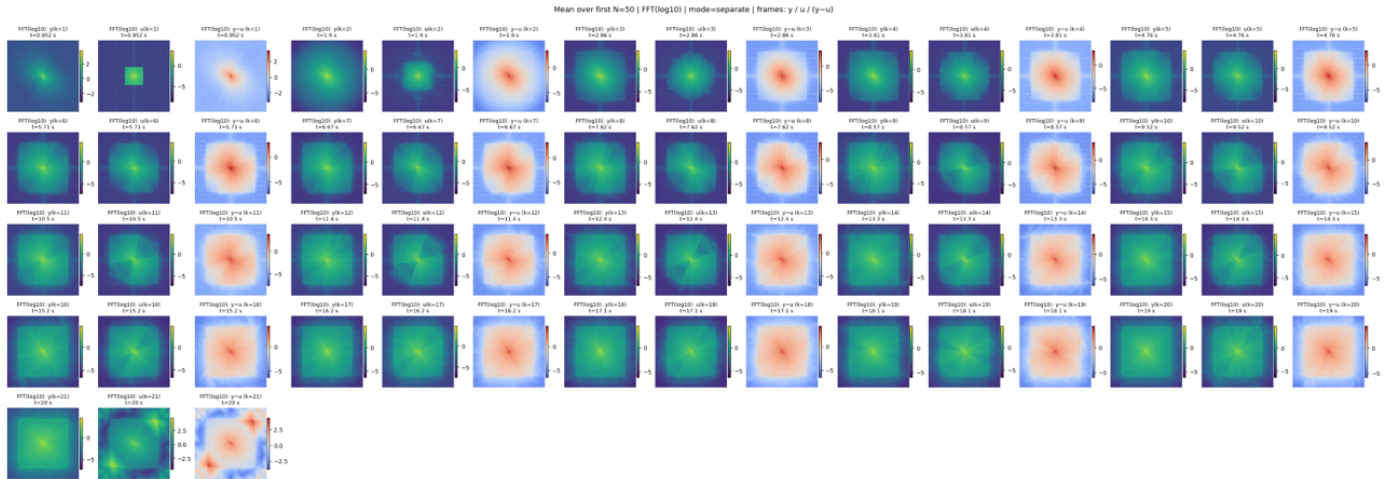


Figure 49: 2D NS dataset and perturbed result evolution difference (upsampled  $256 \times 256$  datasets solved by PDE solver)

$y$  means perturbed initial conditions' evolution,  $u$  means original initial conditions' evolution,  $y-u$  means the difference between perturbed and original evolution

The original initial condition only has frequencies between -32 and 32 on x and y axes, because I interpolate the original  $64 \times 64$  signal to  $256 \times 256$  by zero padding in Fourier domain. Lower resolution will incur numerical errors using the solver. The later frames of both original and perturbed datasets has frequencies between -85 and 85 on x and y axes, because the pseudo-spectral solver follows Orszag's 2/3 rule to do de-aliasing

## D.9 Spectral and Enstrophy Analysis of the 2D NS Dataset

The initial condition which is a GRF, roughly follows a power law spectral distribution. The system's enstrophy increases in time as vorticity is exerted to the system temporarily. When averaging the dataset's vorticity values across all records, we can see the forcing pattern emerges. Because the FFT of the forcing pattern is actually 2 symmetric frequency at (-1,1) and (1,-1), we see that the log absolute the FFT result of vorticity actually evolves and spreads diagonally.

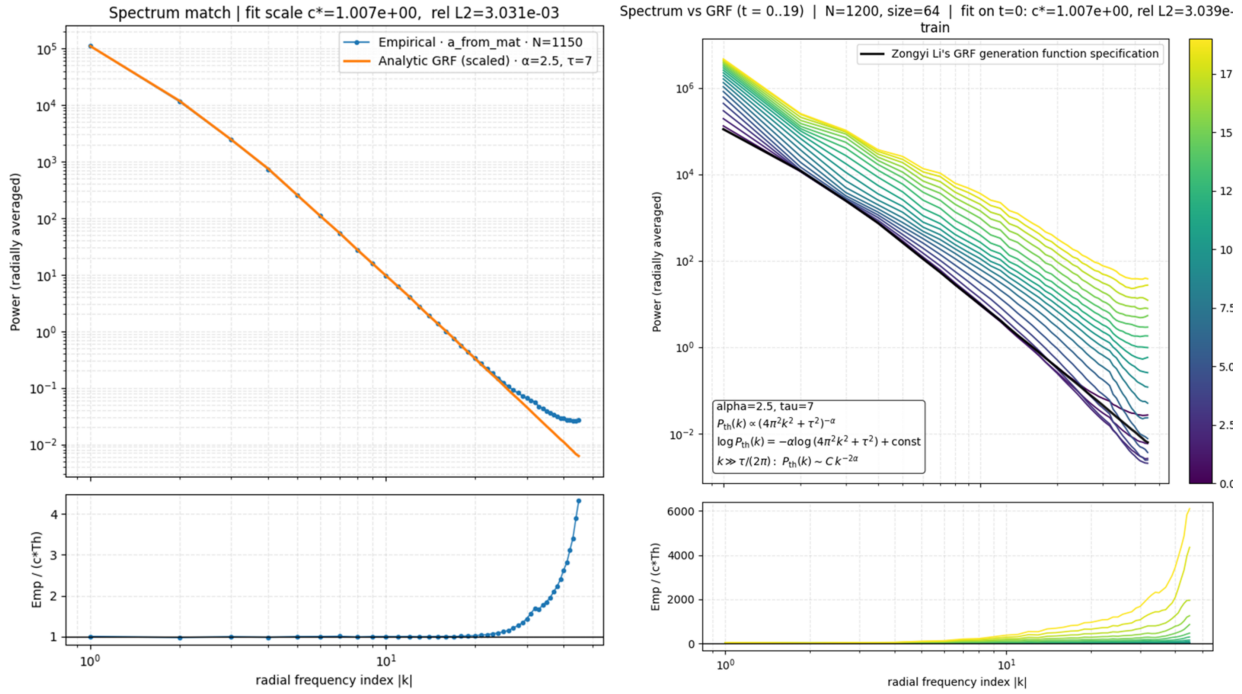


Figure 50: 2D NS dataset initial condition spectrum and temporal evolution of vorticity spectrum

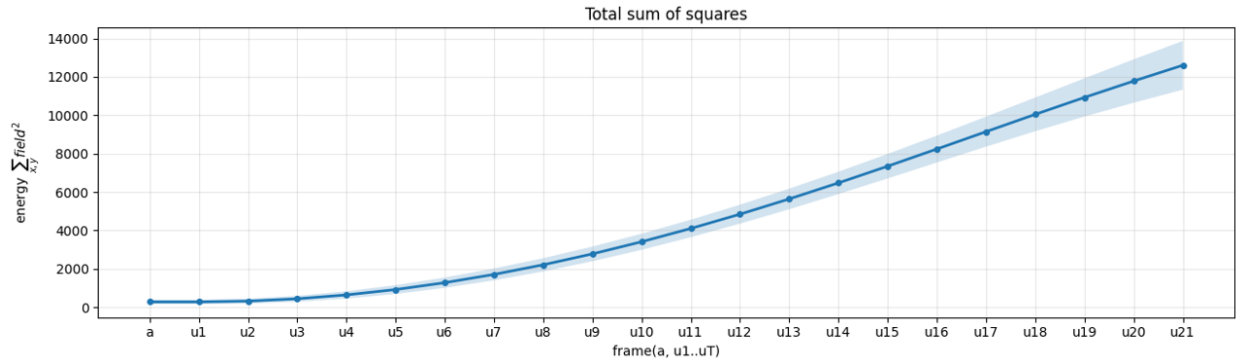


Figure 51: 2D NS dataset temporal evolution of enstrophy

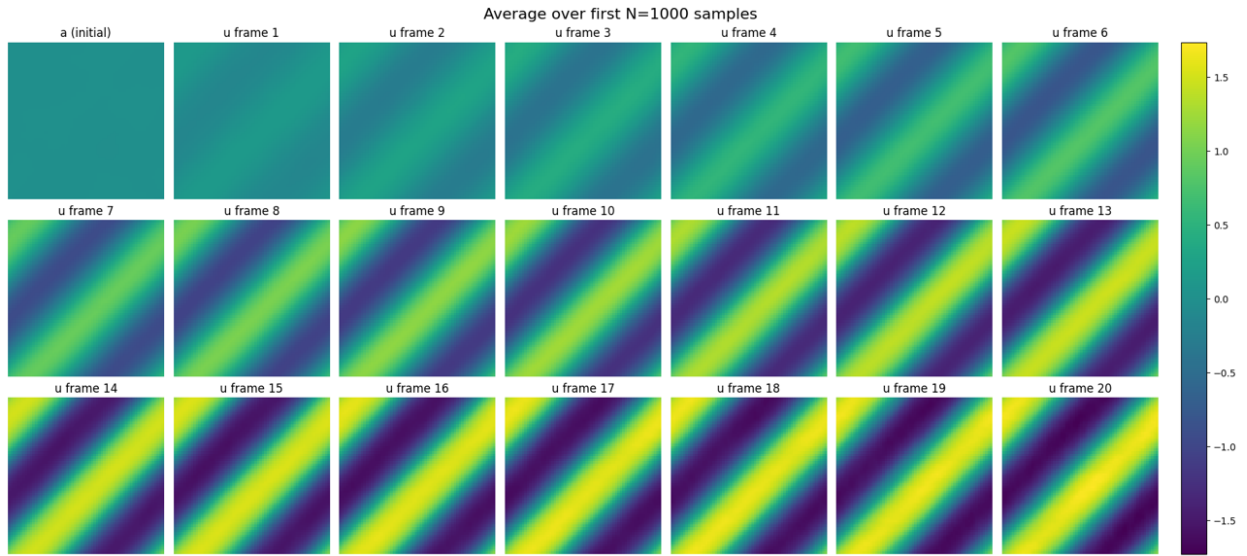


Figure 52: 2D NS dataset temporal evolution of average vorticity (original  $64 \times 64$  dataset in [39])

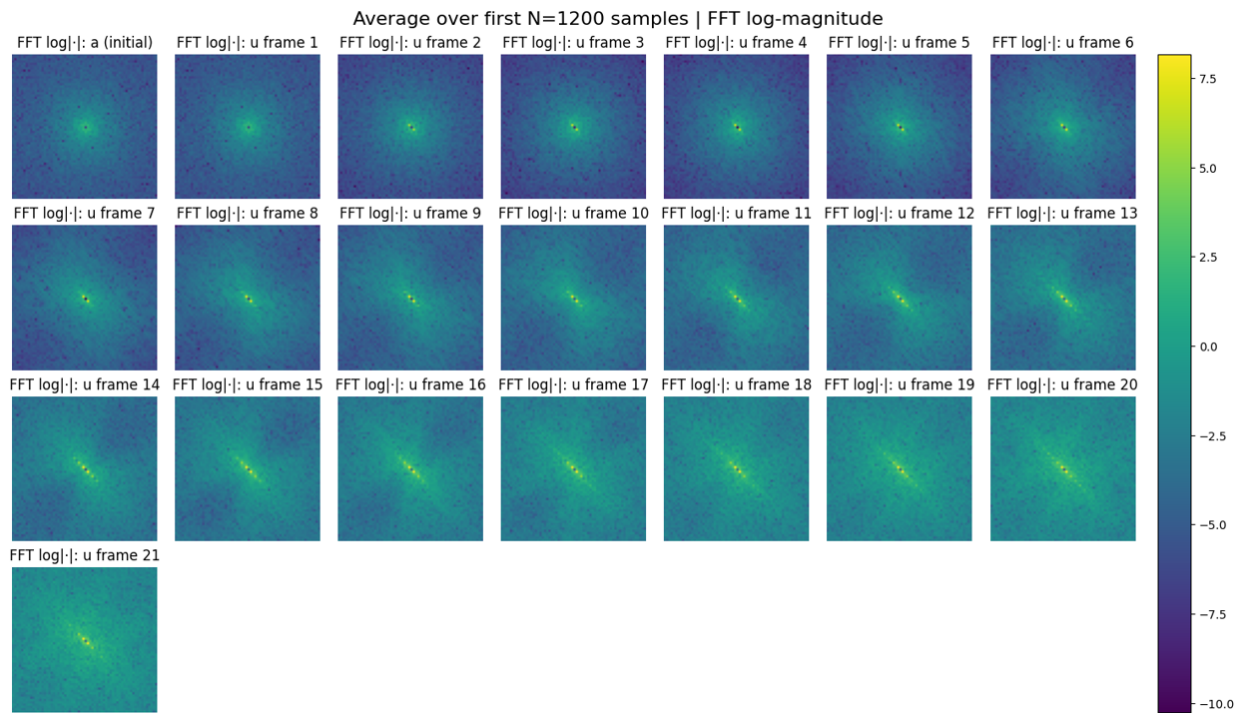


Figure 53: 2D NS dataset temporal evolution of average log absolute Fourier coefficients of vorticity (original  $64 \times 64$  dataset in [39])

## D.10 Different External Forcings

To further validate the relationship between our generated perturbation and NS dataset external forcing, I generated more NS dataset of different external forcing pattern and attacked them using this method. The results validate that this method correctly attacks the dataset and the model, because the perturbation is reflective of the external forcing of the dataset. When there is no external forcing on the system, the perturbation on initial conditions is a random field with no discernible patterns.

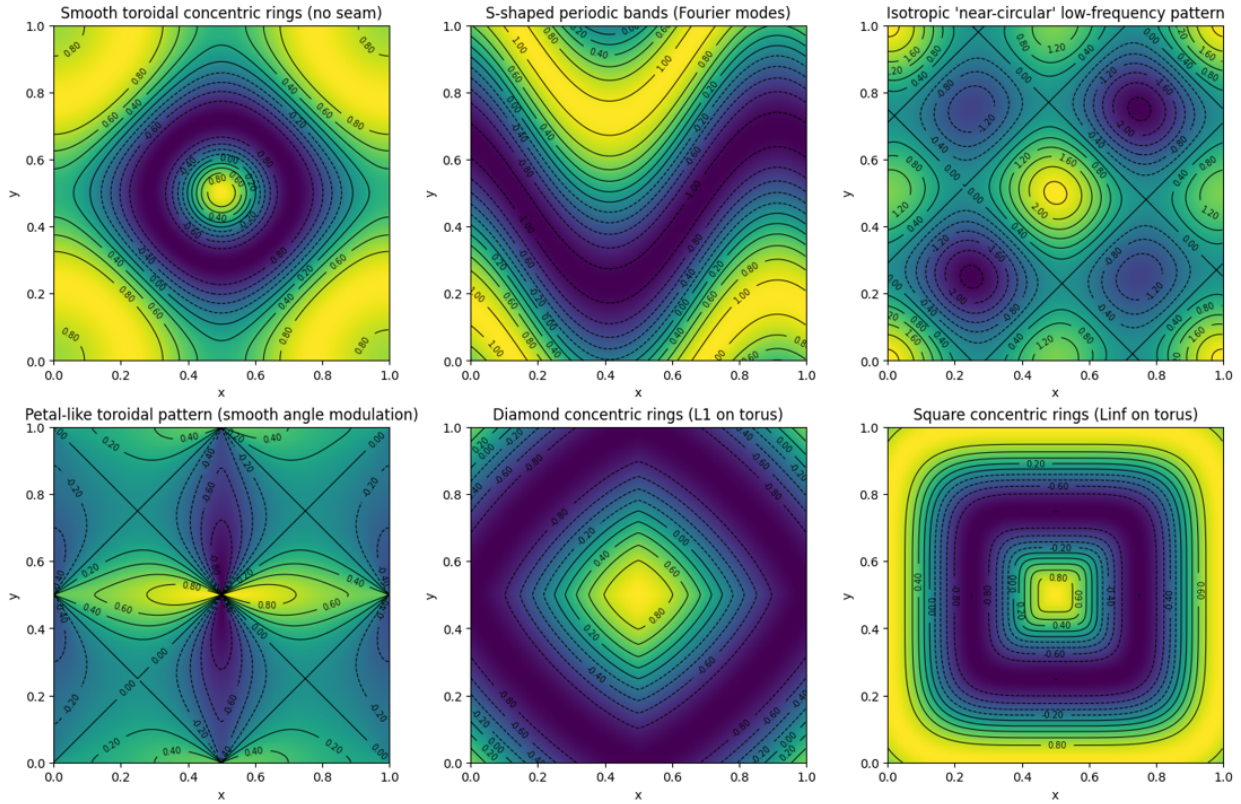


Figure 54: All forcing patterns tested in the 2D NS datasets

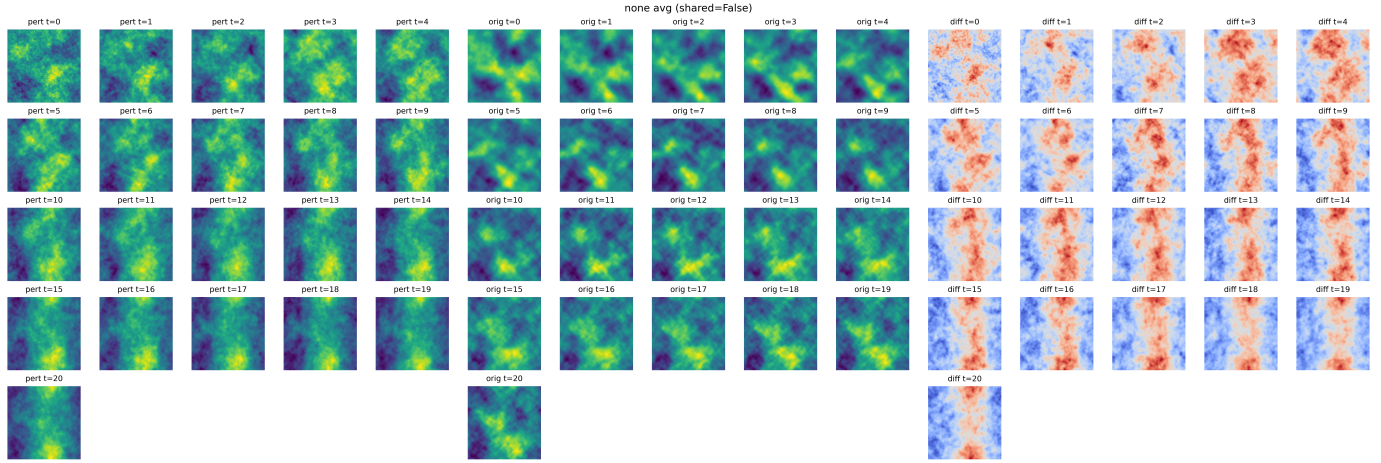


Figure 55: Evolution of original and perturbed datasets and the difference of perturbed and original datasets under no external forcing

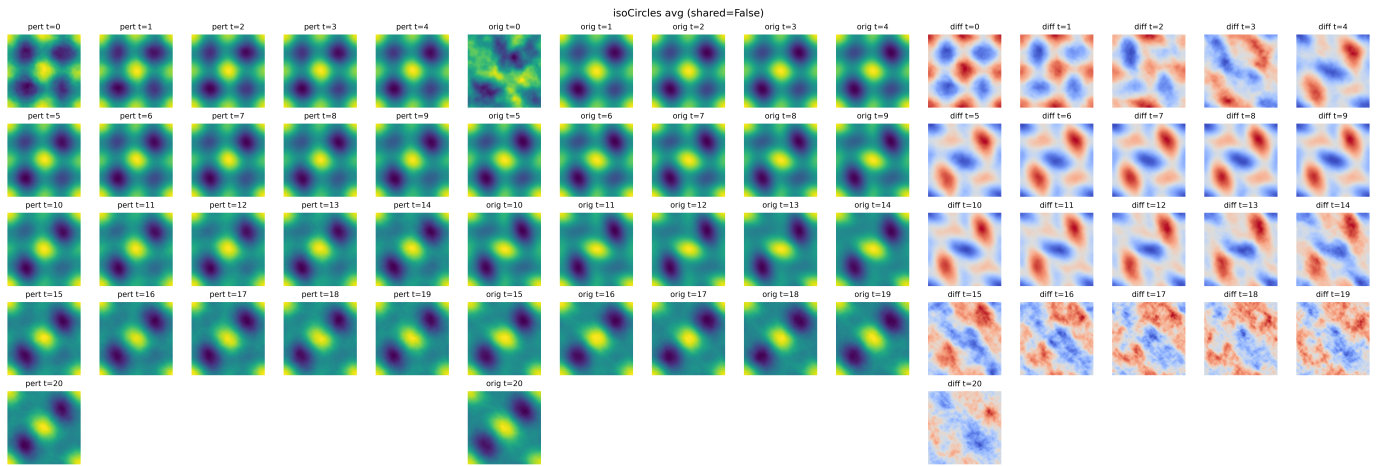


Figure 56: Evolution of original and perturbed datasets and the difference of perturbed and original datasets under isoCircles external forcing pattern

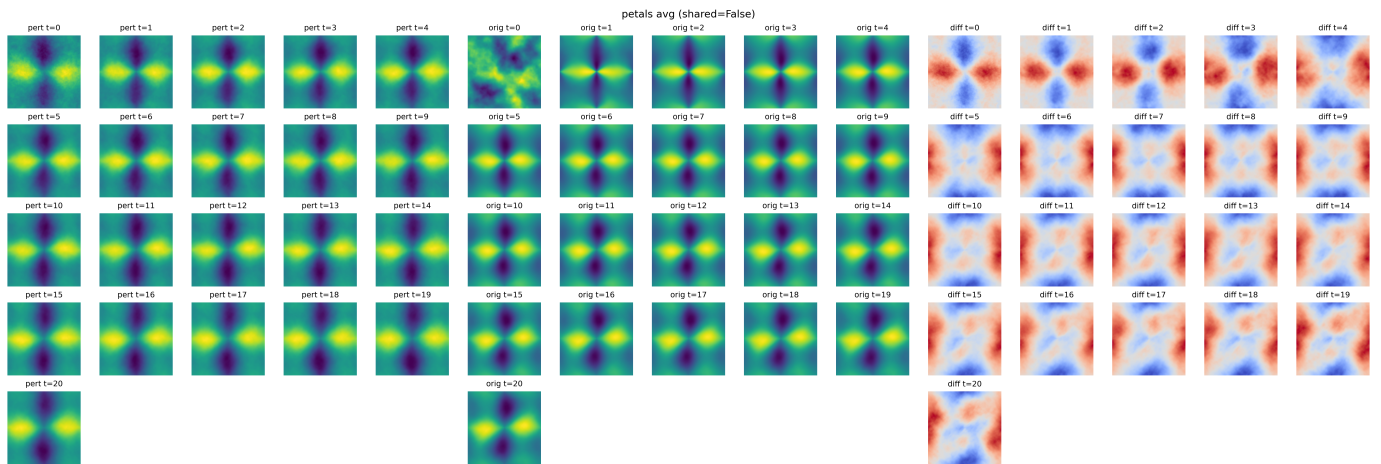


Figure 57: Evolution of original and perturbed datasets and the difference of perturbed and original datasets under petals external forcing pattern

## D.11 FNO Kernel Visualization

One interesting finding is that the complex number matrix kernel learned in training shows the Orzsag's  $2/3$  rule's pattern. I calculated the singular value of every complex matrix on every frequency point in Fourier domain. The entropy of singular value of every matrix shows that there is a pattern at around  $2/3$  of the frequency maximum. Because the complex tensor are symmetric on the frequency domain, only the 2 quarters of the tensors are shown.

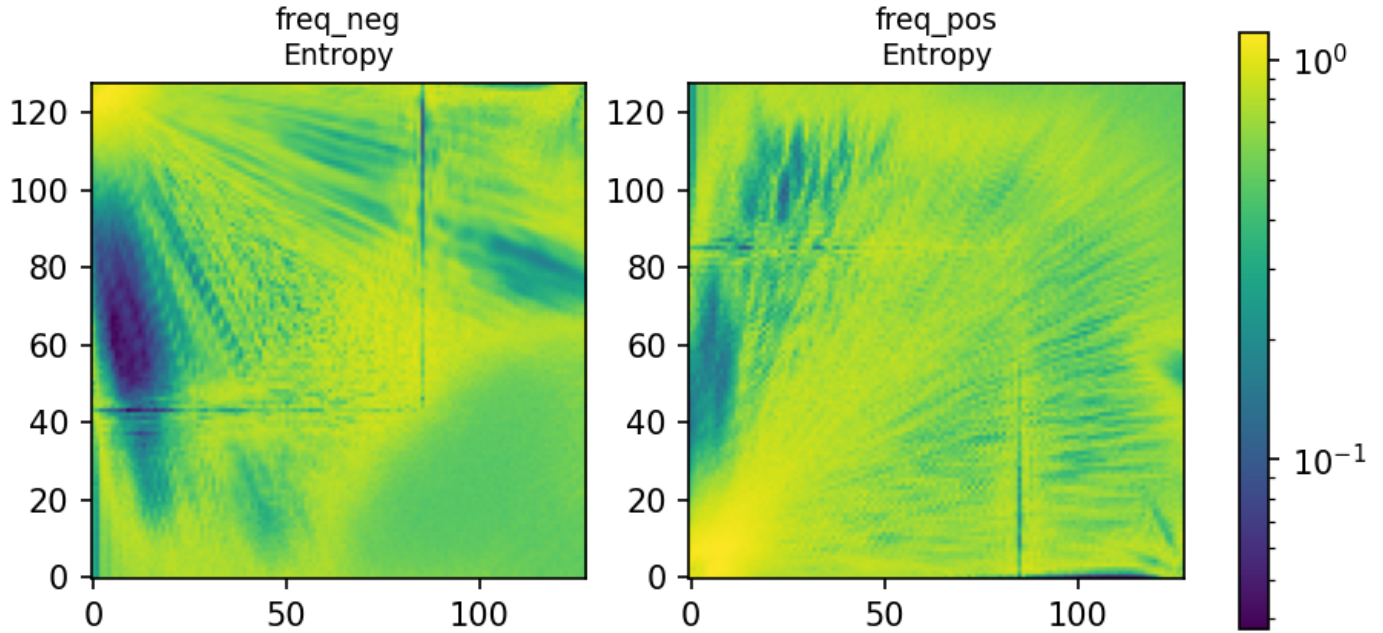


Figure 58: Entropy of singular value of the complex matrices on every frequency point

## D.12 Model Explainability

I trained an FNO model of 4 Fourier layers using the NS dataset, and then only kept the first  $k$  Fourier layers when doing inference to see what the output looks like. The results shows that FNO is indeed one surrogate modeling method. Its intermediate representation shares no resemblance to the temporal evolution of the NS system solved using pseudo-spectral solver. This may partially explain why FNO does not generalize well into all kinds of initial condition and is not a universal solver.

modes128\_width40\_epochs500\_Tin10\_T10\_variants\_keep0to4\_pred11 sample 1

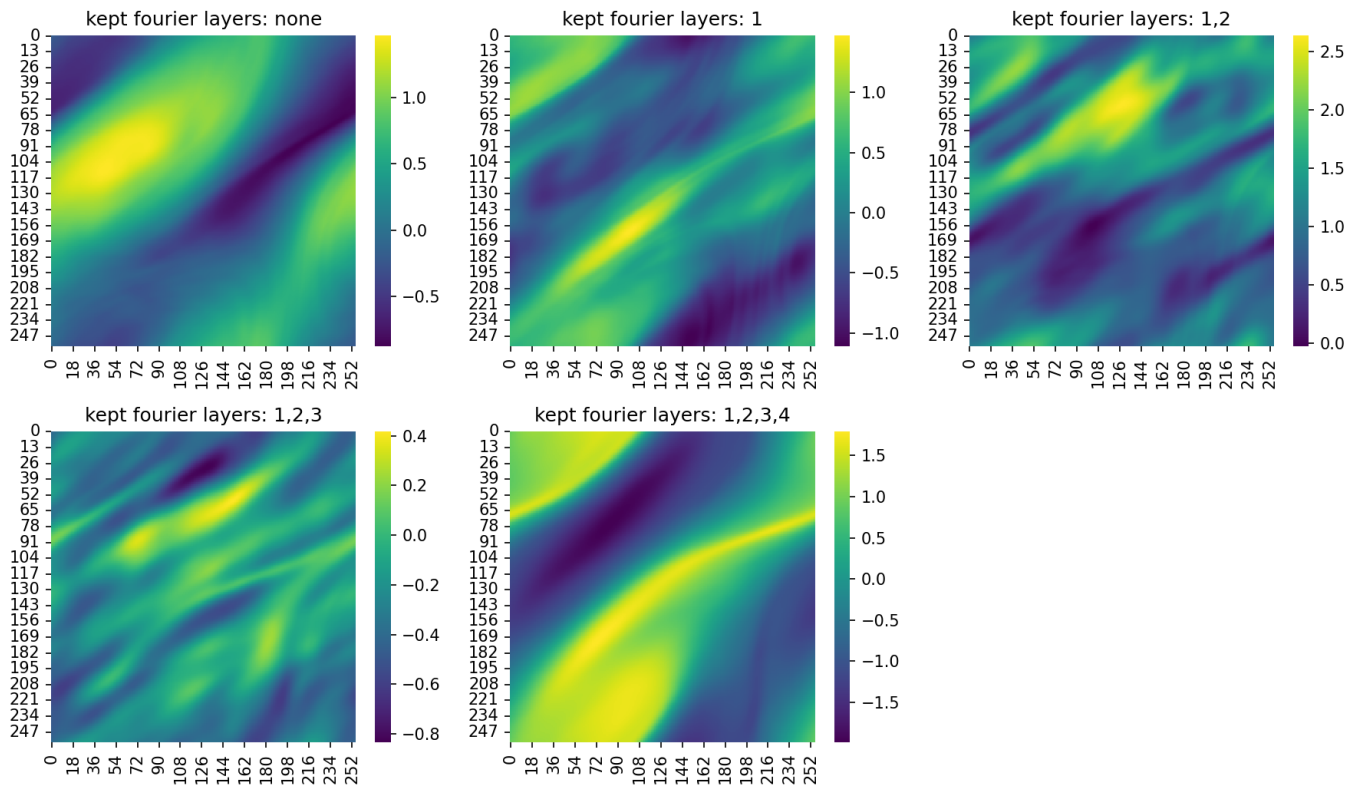


Figure 59: Outputs of trained FNO when truncated in terms of number of Fourier layers